

INFORMATION TO USERS

This manuscript has been reproduced from the microfilm master. UMI films the text directly from the original or copy submitted. Thus, some thesis and dissertation copies are in typewriter face, while others may be from any type of computer printer.

The quality of this reproduction is dependent upon the quality of the copy submitted. Broken or indistinct print, colored or poor quality illustrations and photographs, print bleedthrough, substandard margins, and improper alignment can adversely affect reproduction.

In the unlikely event that the author did not send UMI a complete manuscript and there are missing pages, these will be noted. Also, if unauthorized copyright material had to be removed, a note will indicate the deletion.

Oversize materials (e.g., maps, drawings, charts) are reproduced by sectioning the original, beginning at the upper left-hand corner and continuing from left to right in equal sections with small overlaps.

Photographs included in the original manuscript have been reproduced xerographically in this copy. Higher quality 6" x 9" black and white photographic prints are available for any photographs or illustrations appearing in this copy for an additional charge. Contact UMI directly to order.

ProQuest Information and Learning
300 North Zeeb Road, Ann Arbor, MI 48106-1346 USA
800-521-0600

UMI[®]

University of Alberta

**A Computational Model of Vortex Breakdown in Density
Stratified Flows**

by

Kevin Reid



A thesis submitted to the Faculty of Graduate Studies and Research in
partial fulfillment of the requirements for the degree of Master of Science.

Department of Mechanical Engineering

**Edmonton, Alberta
Spring 2000**



**National Library
of Canada**

**Acquisitions and
Bibliographic Services**

**395 Wellington Street
Ottawa ON K1A 0N4
Canada**

**Bibliothèque nationale
du Canada**

**Acquisitions et
services bibliographiques**

**395, rue Wellington
Ottawa ON K1A 0N4
Canada**

Your file Votre référence

Our file Notre référence

The author has granted a non-exclusive licence allowing the National Library of Canada to reproduce, loan, distribute or sell copies of this thesis in microform, paper or electronic formats.

The author retains ownership of the copyright in this thesis. Neither the thesis nor substantial extracts from it may be printed or otherwise reproduced without the author's permission.

L'auteur a accordé une licence non exclusive permettant à la Bibliothèque nationale du Canada de reproduire, prêter, distribuer ou vendre des copies de cette thèse sous la forme de microfiche/film, de reproduction sur papier ou sur format électronique.

L'auteur conserve la propriété du droit d'auteur qui protège cette thèse. Ni la thèse ni des extraits substantiels de celle-ci ne doivent être imprimés ou autrement reproduits sans son autorisation.

0-612-60173-0

Canada

University of Alberta

Library Release Form

Name of Author: Kevin Reid

Title of Thesis: A Computational Model of Vortex Breakdown in Density Stratified Flows

Degree: Master of Science

Year this Degree Granted: 2000

Permission is hereby granted to the University of Alberta to reproduce single copies of this thesis and to lend or sell such copies for private, scholarly, or scientific research purposes only.

The author reserves all other publication and other rights in association with the copyright in the thesis, and except as hereinbefore provided, neither the thesis nor any substantial portion thereof may be printed or otherwise reproduced in any material form whatever without the author's prior written permission.



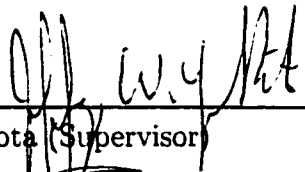
Kevin Reid
177 Ross Haven Drive,
Ft. McMurray, AB
Canada, T9H 3P1

April 17/2000

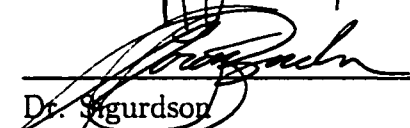
University of Alberta

Faculty of Graduate Studies and Research

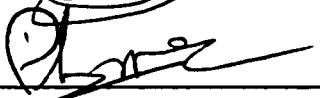
The undersigned certify that they have read, and recommend to the Faculty of Graduate Studies and Research for acceptance, a thesis entitled A Computational Model of Vortex Breakdown in Density Stratified Flows submitted by Kevin Reid in partial fulfillment of the requirements for the degree of Master of Science.



Dr. Yokota (Supervisor)



Dr. Sigurdson



Dr. Mees

Date APRIL 14 / 2000

ABSTRACT

A numerical scheme for the incompressible, inviscid, axisymmetric modelling of the onset of vortex breakdown in a density stratified flow has been developed. Immiscible stratifications are considered and a potential/complex lamellar velocity decomposition is employed.

The code's fidelity was verified against experimental and numerical homogeneous flow solutions of previous investigators. The behavior of homogeneous flow vortex breakdown solutions were found to be in qualitative agreement with past experimental and numerical work. In a diverging pipe, the critical value of the helix angle was found to be 29° .

The azimuthal vorticity created by local density and pressure gradients was found to influence the onset of vortex breakdown. Density stratifications of 10% were considered. In the breakdown region, positive radial density gradients created negative azimuthal vorticity and promoted breakdown solutions. Negative radial density gradients created positive azimuthal vorticity in the breakdown region, thus hindering breakdown solutions. These results are in agreement with predictions made by the vorticity dynamics theory of vortex breakdown.

An expert is a man who has made all the mistakes, which can be made, in a very narrow field.

—Niels Bohr

A computer lets you make more mistakes faster than any invention in human history – with the possible exception of handguns and tequila

—Mitch Ratliffe

Dedicated to my Mom and Dad for all of their support and encouragement.

ACKNOWLEDGEMENTS

I would like to extend my sincerest thanks to my supervisor, Jeffrey W. Yokota. The code used in this thesis is based on his work, and without his support and experience my work would not have been possible. I have learned enumerable lessons from Jeff, not only in the technical sphere but also from his approach to solving problems and meticulous attention to detail.

During my tenure in the CFDAM lab the mood was always laid back but supportive. This was due to the company of, at various times, Seifu Bekele, Adam Medd, Chris Reaume and Lance Portas. Lance deserves special mention for being not only the LTG (Local TeX Guru), but also the LMG (Local Matlab Guru). Chris's frequent off color jokes and forays into religion will always be remembered.

I owe my parents a debt of gratitude for always supporting what I have done, not only in Graduate School, but all throughout my life.

Finally, I would like to thank the Natural Sciences and Engineering Research Council of Canada for supporting this work under a PGS A Scholarship.

CONTENTS

1	Introduction	1
2	Literature Review	3
2.1	Experimental Review	3
2.2	Theoretical Review	14
2.2.1	Wave Theory	15
2.2.2	Quasi-Cylindrical Theory	16
2.2.3	Instability Theory	18
2.3	Computational Review	19
2.4	Vorticity Dynamics in Vortex Breakdown	23
3	Mathematical Model	27
3.1	General Form of Governing Equations	27
3.2	Modification of Equations	29
3.2.1	Incompressible Flow	29
3.2.2	Inviscid Flow	29
3.2.3	Axisymmetric Flow	31
3.3	Clebsch Decomposition	34
3.4	Numerical Form of Convection Equations	38
3.5	Generalized Transformation	40
3.6	Dimensional Analysis	43
4	Numerical Techniques	45
4.1	Solution Sequence	45
4.2	Elliptic Equations	46
4.2.1	Approximate LU Factorization	46
4.2.2	Calculation of the Residual	49
4.2.3	Stability Analysis Of LU Scheme	50
4.2.4	Multigrid Convergence Acceleration	53

4.3	Hyperbolic Equations	55
4.3.1	UNO2 Convection Scheme	57
4.3.2	Source Terms	58
4.4	Boundary and Initial Conditions	58
4.4.1	Solid Wall and Symmetry Boundary Conditions	58
4.4.2	Inflow Boundary Conditions	59
4.4.3	Outflow Boundary Condition	64
4.4.4	Initial Conditions	64
5	Results	67
5.1	Flow Through a Straight Pipe	67
5.1.1	Non-Swirling Flow	70
5.1.2	Swirling Flow	70
5.2	Flow Through a Divergent Pipe	79
5.2.1	Non-Swirling Flow	82
5.2.2	Pre-Breakdown Swirling Flow	89
5.2.3	Incipient Breakdown Swirling Flow	101
5.2.4	Response of Breakdown Zone to Increased Swirl	117
5.3	Vortex Breakdown in Density Stratified Fluids	132
5.3.1	Summary of the Vorticity Dynamics of Vortex Break- down	133
5.3.2	Effect of Negative Density Gradient on Vortex Break- down	140
5.3.3	Effect of Positive Density Gradient on Vortex Breakdown	158
5.3.4	Effect of Density Stratification on Above Critical Swirl Vortex Breakdown	165
6	Conclusions	209
	Bibliography	214

LIST OF FIGURES

2.1	Continuous Flow Vortex Breakdown Test Facility	4
2.2	Spiral Vortex Breakdown. Reprinted with permission from Faler and Leibovich [1977]. Physics of Fluids 9 p. 1391 . . .	6
2.3	Double Helix Vortex Breakdown. Reprinted with permission from Faler and Leibovich [1977]. Physics of Fluids 9 p. 1394	6
2.4	Axisymmetric Vortex Breakdown. Reprinted with permission from Faler and Leibovich [1977]. Physics of Fluids 9 p. 1389	7
2.5	Type 6 Vortex Breakdown. Reprinted with permission from Faler and Leibovich [1977]. Physics of Fluids 9 p. 1393 . . .	9
2.6	Type 4 Vortex Breakdown. Reprinted with permission from Faler and Leibovich [1977]. Physics of Fluids 9 p. 1394 . . .	10
2.7	Type 3 Vortex Breakdown. Reprinted with permission from Faler and Leibovich [1977]. Physics of Fluids 9 p. 1395 . . .	10
2.8	Type 1 Vortex Breakdown. Reprinted with permission from Faler and Leibovich [1977]. Physics of Fluids 9 p. 1391 . . .	11
2.9	Two Tailed Type 0 Vortex Breakdown. Reprinted with permission from Faler and Leibovich [1977]. Physics of Fluids 9 p. 1390	12
3.1	Cylindrical Co-ordinate System	28
3.2	Schematic of Co-ordinate Transformation	40
4.1	Growth Factor of LU Scheme	52
4.2	Five Level Multigrid Scheme	55
4.3(a)	Inflow Distribution of Reduced Circulation ($V_{\theta 1} = 0.5$) . . .	62
4.3(b)	Inflow Distribution of Azimuthal Velocity ($V_{\theta 1} = 0.5$) . . .	63
4.4	Initial Condition on Beta Potential ($V_{\theta 1} = 0.5$)	66

5.1	Straight Pipe Numerical Domain	69
5.2(a)	Initial Condition of Z Material Lines ($V_{\theta 1} = 0.0$)	73
5.2(b)	Z Material Lines After 3200 timesteps ($V_{\theta 1} = 0.0$)	74
5.3(a)	Inflow Helix Angle β ($V_{\theta 1} = 0.6$)	75
5.3(b)	Z Material Lines After 3200 timesteps ($V_{\theta 1} = 0.6$)	76
5.3(c)	B Potential After 3200 timesteps ($V_{\theta 1} = 0.6$)	77
5.3(d)	Temporal Variation of Inflow Helix Angle (β) ($V_{\theta 1} = 0.6$)	78
5.4	Diverging Pipe Numerical Domain	81
5.5(a)	Initial Condition of Axial Velocity ($V_{\theta 1} = 0.0$)	84
5.5(b)	Axial Velocity After 3200 timesteps ($V_{\theta 1} = 0.0$)	85
5.5(c)	F Potential 3200 timesteps ($V_{\theta 1} = 0.0$)	86
5.5(d)	Initial Condition on Z Material Lines ($V_{\theta 1} = 0.0$)	87
5.5(e)	Z Material Lines after 3200 timesteps ($V_{\theta 1} = 0.0$)	88
5.6(a)	Initial Condition of Axial Velocity ($V_{\theta 1} = 0.4$)	92
5.6(b)	Inflow Helix Angle β ($V_{\theta 1} = 0.4$)	93
5.6(c)	Axial Velocity After 3200 timesteps ($V_{\theta 1} = 0.4$)	94
5.6(d)	Z Material Lines after 3200 timesteps ($V_{\theta 1} = 0.4$)	95
5.6(e)	B Potential After 3200 timesteps ($V_{\theta 1} = 0.4$)	96
5.6(f)	F Potential After 3200 timesteps ($V_{\theta 1} = 0.4$)	97
5.6(g)	Detailed F Potential After 3200 timesteps ($V_{\theta 1} = 0.4$)	98
5.6(h)	Convergence of Minimum Axial Velocity ($V_{\theta 1} = 0.4$)	99
5.6(i)	Temporal Variation of Inflow Helix Angle β ($V_{\theta 1} = 0.4$)	100
5.7(a)	Axial Velocity After 3200 timesteps ($V_{\theta 1} = 0.45$)	105
5.7(b)	Inflow Helix Angle β ($V_{\theta 1} = 0.45$)	106
5.7(c)	Z Material Co-ordinate After 3200 timesteps ($V_{\theta 1} = 0.45$)	107
5.7(d)	B Potential After 3200 timesteps ($V_{\theta 1} = 0.45$)	108
5.7(e)	Convergence of Minimum Axial Velocity ($V_{\theta 1} = 0.45$)	109
5.7(f)	Temporal Variation of Inflow Helix Angle β ($V_{\theta 1} = 0.45$)	110
5.8(a)	Inflow Helix Angle β ($V_{\theta 1} = 0.5$)	111
5.8(b)	Axial Velocity After 5400 timesteps ($V_{\theta 1} = 0.5$)	112
5.8(c)	Variation of Axial Velocity With Time ($V_{\theta 1} = 0.5$)	113
5.8(d)	Z Material Co-ordinate After 5400 timesteps ($V_{\theta 1} = 0.5$)	114
5.8(e)	B Potential After 5400 timesteps ($V_{\theta 1} = 0.5$)	115
5.8(f)	Temporal Variation of Inflow B ($V_{\theta 1} = 0.5$)	116
5.9(a)	Inflow Helix Angle β Potential ($V_{\theta 1} = 0.55$)	120
5.9(b)	Axial Velocity After 3200 timesteps ($V_{\theta 1} = 0.55$)	121
5.9(c)	Z Material Co-ordinate After 3200 timesteps ($V_{\theta 1} = 0.55$)	122
5.9(d)	B Potential After 3200 timesteps ($V_{\theta 1} = 0.55$)	123

5.10(a)	Axial Velocity After 3200 timesteps ($V_{\theta 1} = 0.60$)	124
5.10(b)	Inflow Helix Angle β ($V_{\theta 1} = 0.60$)	125
5.10(c)	Temporal Variation of Inflow Helix Angle β ($V_{\theta 1} = 0.60$)	126
5.10(d)	Z Material Co-ordinate After 3200 timesteps ($V_{\theta 1} = 0.60$)	127
5.10(e)	Axial Variation of Axial Velocity at Breakdown ($V_{\theta 1} = 0.60$)	128
5.10(f)	B Potential After 3200 timesteps ($V_{\theta 1} = 0.60$)	129
5.10(g)	F Potential After 3200 timesteps ($V_{\theta 1} = 0.60$)	130
5.10(h)	Detailed F Potential After 3200 timesteps ($V_{\theta 1} = 0.60$)	131
5.11	Azimuthal Vorticity Created by Different Density/Pressure Gradients	135
5.12	Azimuthal Vorticity Created by Different Density/ F Potential Gradients	136
5.13(a)	Initial Axial Vorticity (Homogeneous Flow $V_{\theta 1} = 0.50$)	137
5.13(b)	Axial Vorticity at Breakdown (5400 timesteps) (Homogeneous Flow $V_{\theta 1} = 0.50$)	138
5.13(c)	Azimuthal Vorticity at Breakdown (5400 timesteps) (Homogeneous Flow $V_{\theta 1} = 0.50$)	139
5.14(a)	Axial Velocity Field After 5400 timesteps (Negative Stratification $r_s = 0.77$ $V_{\theta 1} = 0.50$)	142
5.14(b)	Z Material Field After 5400 timesteps (Negative Stratification $r_s = 0.77$ $V_{\theta 1} = 0.50$)	143
5.14(c)	Axial Vorticity After 5400 timesteps (Negative Stratification $r_s = 0.77$ $V_{\theta 1} = 0.50$)	144
5.14(d)	Azimuthal Vorticity After 5400 timesteps (Negative Stratification $r_s = 0.77$ $V_{\theta 1} = 0.50$)	145
5.14(e)	Density Interface After 5400 timesteps (Negative Stratification $r_s = 0.77$ $V_{\theta 1} = 0.50$)	146
5.14(f)	F Potential After 5400 timesteps (Negative Stratification $r_s = 0.77$ $V_{\theta 1} = 0.50$)	147
5.15(a)	Axial Velocity After 5400 timesteps (Negative Stratification $r_s = 0.25$ $V_{\theta 1} = 0.50$)	149
5.15(b)	Z Material Field After 5400 timesteps (Negative Stratification $r_s = 0.25$ $V_{\theta 1} = 0.50$)	150
5.15(c)	Axial Vorticity After 5400 timesteps (Negative Stratification $r_s = 0.25$ $V_{\theta 1} = 0.50$)	151
5.15(d)	Azimuthal Vorticity After 5400 timesteps (Negative Stratification $r_s = 0.25$ $V_{\theta 1} = 0.50$)	152

5.15(e)	Density Interface After 5400 timesteps (Negative Stratification $r_s = 0.25$ $V_{\theta 1} = 0.50$)	153
5.15(f)	F Potential After 5400 timesteps (Negative Stratification $r_s = 0.25$ $V_{\theta 1} = 0.50$)	154
5.15(g)	Detailed F Potential After 5400 timesteps (Negative Stratification $r_s = 0.25$ $V_{\theta 1} = 0.50$)	155
5.16	Variation of Minimum Axial Velocity Along Pipe Centerline For Various Stratification Locations (Negative Stratification $V_{\theta 1} = 0.50$)	157
5.17	Variation of Minimum Axial Velocity Along Pipe Centerline For Various Stratification Locations (Positive Stratification $V_{\theta 1} = 0.50$)	159
5.18(a)	Azimuthal Vorticity After 3200 timesteps (Homogeneous $V_{\theta 1} = 0.50$)	160
5.18(b)	Azimuthal Vorticity After 3200 timesteps (Positive Stratification $r_s = 0.77$ $V_{\theta 1} = 0.50$)	161
5.18(c)	Azimuthal Vorticity After 3200 timesteps (Positive Stratification $r_s = 0.25$ $V_{\theta 1} = 0.50$)	162
5.18(d)	Density Interface After 3200 timesteps (Positive Stratification $r_s = 0.77$ $V_{\theta 1} = 0.50$)	163
5.18(e)	Density Interface After 3200 timesteps (Positive Stratification $r_s = 0.25$ $V_{\theta 1} = 0.50$)	164
5.19(a)	Initial Axial Vorticity (Homogeneous $V_{\theta 1} = 0.60$)	166
5.19(b)	Axial Vorticity After 3200 timesteps (Homogeneous $V_{\theta 1} = 0.60$)	167
5.19(c)	Azimuthal Vorticity After 3200 timesteps (Homogeneous $V_{\theta 1} = 0.60$)	168
5.20	Variation of Minimum Axial Velocity Along Pipe Centerline For Various Stratification Locations (Negative Stratification $V_{\theta 1} = 0.60$)	170
5.21	Variation of Minimum Axial Velocity Along Pipe Centerline For Various Stratification Locations (Positive Stratification $V_{\theta 1} = 0.60$)	171
5.22(a)	Axial Velocity Field After 3200 timesteps (Negative Stratification $r_s = 0.25$ $V_{\theta 1} = 0.60$)	173
5.22(b)	Z Material Field After 3200 timesteps (Negative Stratification $r_s = 0.25$ $V_{\theta 1} = 0.60$)	174

5.22(c)	B Potential After 3200 timesteps (Negative Stratification $r_s = 0.25$ $V_{\theta 1} = 0.60$)	175
5.22(d)	F Potential After 3200 timesteps (Negative Stratification $r_s = 0.25$ $V_{\theta 1} = 0.60$)	176
5.22(e)	Detailed F Potential After 3200 timesteps (Negative Stratification $r_s = 0.25$ $V_{\theta 1} = 0.60$)	177
5.22(f)	Axial Vorticity After 3200 timesteps (Negative Stratification $r_s = 0.25$ $V_{\theta 1} = 0.60$)	178
5.22(g)	Azimuthal Vorticity After 3200 timesteps (Negative Stratification $r_s = 0.25$ $V_{\theta 1} = 0.60$)	179
5.22(h)	Density Interface After 3200 timesteps (Negative Stratification $r_s = 0.25$ $V_{\theta 1} = 0.60$)	180
5.23(a)	Axial Velocity Field After 3200 timesteps (Negative Stratification $r_s = 0.77$ $V_{\theta 1} = 0.60$)	182
5.23(b)	Z Material Field After 3200 timesteps (Negative Stratification $r_s = 0.77$ $V_{\theta 1} = 0.60$)	183
5.23(c)	B Potential After 3200 timesteps (Negative Stratification $r_s = 0.77$ $V_{\theta 1} = 0.60$)	184
5.23(d)	F Potential After 3200 timesteps (Negative Stratification $r_s = 0.77$ $V_{\theta 1} = 0.60$)	185
5.23(e)	Detailed F Potential After 3200 timesteps (Negative Stratification $r_s = 0.77$ $V_{\theta 1} = 0.60$)	186
5.23(f)	Density Interface After 3200 timesteps (Negative Stratification $r_s = 0.77$ $V_{\theta 1} = 0.60$)	187
5.23(g)	Axial Vorticity After 3200 timesteps (Negative Stratification $r_s = 0.77$ $V_{\theta 1} = 0.60$)	188
5.23(h)	Azimuthal Vorticity After 3200 timesteps (Negative Stratification $r_s = 0.77$ $V_{\theta 1} = 0.60$)	189
5.24(a)	Axial Velocity Field After 3200 timesteps (Positive Stratification $r_s = 0.25$ $V_{\theta 1} = 0.60$)	191
5.24(b)	Z Material Field After 3200 timesteps (Positive Stratification $r_s = 0.25$ $V_{\theta 1} = 0.60$)	192
5.24(c)	B Potential After 3200 timesteps (Positive Stratification $r_s = 0.25$ $V_{\theta 1} = 0.60$)	193
5.24(d)	F Potential After 3200 timesteps (Positive Stratification $r_s = 0.25$ $V_{\theta 1} = 0.60$)	194
5.24(e)	Detailed F Potential After 3200 timesteps (Positive Stratification $r_s = 0.25$ $V_{\theta 1} = 0.60$)	195

5.24(f)	Axial Vorticity After 3200 timesteps (Positive Stratification $r_s = 0.25$ $V_{\theta 1} = 0.60$)	196
5.24(g)	Azimuthal Vorticity After 3200 timesteps (Positive Strati- fication $r_s = 0.25$ $V_{\theta 1} = 0.60$)	197
5.24(h)	Density Interface After 3200 timesteps (Positive Stratifica- tion $r_s = 0.25$ $V_{\theta 1} = 0.60$)	198
5.25(a)	Axial Velocity Field After 3200 timesteps (Positive Strati- fication $r_s = 0.77$ $V_{\theta 1} = 0.60$)	200
5.25(b)	Z Material Field After 3200 timesteps (Positive Stratifica- tion $r_s = 0.77$ $V_{\theta 1} = 0.60$)	201
5.25(c)	B Potential After 3200 timesteps (Positive Stratification $r_s = 0.77$ $V_{\theta 1} = 0.60$)	202
5.25(d)	F Potential After 3200 timesteps (Positive Stratification $r_s = 0.77$ $V_{\theta 1} = 0.60$)	203
5.25(e)	Detailed F Potential After 3200 timesteps (Positive Strati- fication $r_s = 0.77$ $V_{\theta 1} = 0.60$)	204
5.25(f)	Density Interface After 3200 timesteps (Positive Stratifica- tion $r_s = 0.77$ $V_{\theta 1} = 0.60$)	205
5.25(g)	Axial Vorticity After 3200 timesteps (Positive Stratification $r_s = 0.77$ $V_{\theta 1} = 0.60$)	206
5.25(h)	Azimuthal Vorticity After 3200 timesteps (Positive Strati- fication $r_s = 0.77$ $V_{\theta 1} = 0.60$)	207

NOMENCLATURE

LATIN SYMBOLS

A	Complex Lamellar Potential
B	Helix Angle
C	Complex Lamellar Potential
D	Complex Lamellar Potential
E	Complex Lamellar Potential
F	Complex Lamellar Potential
F_b	Body Force
g	Gravitational Constant
G	Complex Lamellar Potential
G^k	Growth Factor
H	Complex Lamellar Potential
I	Multigrid Interpolation Parameter
J	Jacobian of Grid Transformation Matrix
k	Constant for Hall's Pressure Equation
K	Model Variable for Leapfrog Method

M	Model Variable for Leapfrog Method
N	Model Convected Variable
P	Pressure
R	Pipe Radius
R_s	Surface Force
Re	Reynolds Number
S	Model Source Term
$S_{i,j}^z$	Slope for UNO2 Interpolation
$S_{i,j}^r$	Slope for UNO2 Interpolation
t	Time
T	Multigrid Transfer Operator
U_r	Transformed Radial Velocity
U_z	Transformed Axial Velocity
v_r	Radial Velocity
v_z	Axial Velocity
v_θ	Azimuthal Velocity
V_{z1}	Experimental Constant
V_{z2}	Experimental Constant
$V_{\theta1}$	Experimental Constant
W	Control Surface
(z, r)	Eulerian Co-ordinates
Z	'z' Material Co-ordinate

GREEK SYMBOLS

α	Fourier Number
α_1	Experimental Constant
β	Inflow Helix Angle
β_w	Mesh Wavenumber
β_o	Vorticity Ratio
Γ	Circulation
ζ	Angular Velocity
θ	Azimuthal Co-ordinate
λ_o	Velocity Ratio
Λ	Correlation Term
μ	Implicit Parameter
(ξ, η)	Transformed Co-ordinates
ρ	Density
Σ	Correlation Term
τ	Shear Stress
ϕ	Lamellar Potential
Φ	Correlation Term
ψ	Streamfunction
ω	Relaxation Factor
ω_r	Radial Vorticity
ω_z	Axial Vorticity
ω_θ	Azimuthal Vorticity
Ω	Control Volume

CHAPTER 1

INTRODUCTION

Vortex breakdown is a phenomenon that occurs in flows which consist of a concentrated vortex core with axial velocity. It can best be defined as an abrupt occurrence of an internal stagnation point on the vortex axis followed by a recirculation zone of limited axial extent [Faler and Leibovich 1977, Leibovich 1978].

This flow disruption was first observed in leading edge vortices formed above wings with highly swept leading edges [Peckham and Atkinson 1957] and studied because of its aerodynamic significance. The onset of vortex breakdown above a wing can lead to flow separation, thus altering the lift, drag and moment coefficients. Aerodynamicists are primarily concerned with the onset of breakdown, the flow structure is of secondary importance. Vortex breakdown also occurs in internal flows and has a potential technological application as a flame stabilizer in swirl combustors. Both the conditions leading to the occurrence of a breakdown and the structure of the breakdown zone are important to this application.

A review of the vortex breakdown literature from the past forty years

has revealed no information on the effects of a density stratification on the onset or structure of breakdown flows. Density stratification is present in combustion chambers where a fuel and an oxidant are mixed, and to control such flows the influence of a density gradient must be understood.

CHAPTER 2

LITERATURE REVIEW

2.1 Experimental Review

While vortex breakdown was first observed above wings with highly swept leading edges [Peckham & Atkinson 1957], the majority of the current research in vortex breakdown focuses mainly on internal flows which are easier to control and simulate. Thus, this review summarizes only the work conducted using internal flow devices.

The most common internal flow test apparatus used to study vortex breakdown is a continuous flow device which was first utilized by Harvey [1962]. An axisymmetric schematic of this experimental setup is shown in Figure 2.1. In this device, an initial axial flow (a) is driven by a constant pressure. This axial flow is redirected radially by the pipe walls (b). When this radial flow is passed over a cascade of swirl vanes (c) it acquires a rotational motion. As the flow approaches the axis, the swirl intensifies until it passes over the vane centerbody (d) and is directed axially (e). The swirling flow in the axial direction can be contained by either a straight pipe, or a

pipe with slightly diverging walls. The adverse pressure gradient created by diverging walls promotes the occurrence of a vortex breakdown [Sarpkaya 1974], and the breakdown structure is typically observed in this section.

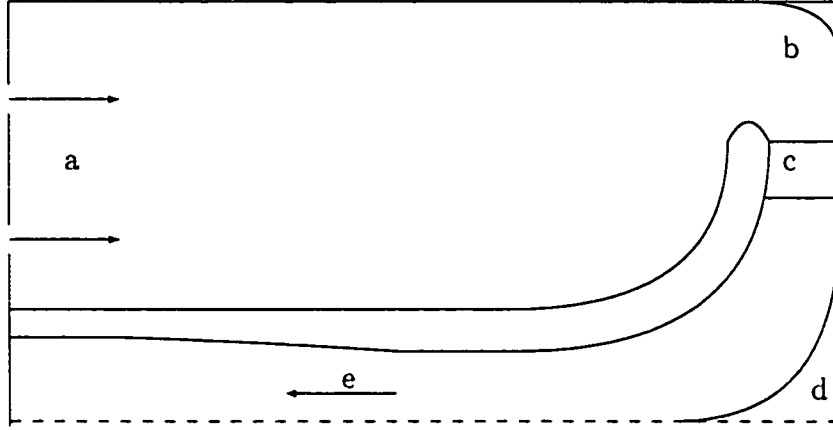


Figure 2.1: Continuous Flow Vortex Breakdown Test Facility

Harvey's goal was to discover if vortex breakdown occurs in internal flows. To this end he used air as the experimental fluid and used the theoretical model proposed by Squire [1960] as a guideline. Squire's model identifies the parameter $\tan\left(\frac{V_{\theta max}}{V_z}\right)$ as an important parameter in breakdown flows. This number is known as the helix angle (B), and Squire postulated that for a breakdown to occur, the maximum value of the helix angle must exceed 50° at one location on the inlet flow, the flow just downstream of the vane centerbody. Using a helix angle which satisfied Squire's criterion for breakdown, Harvey relied on flow visualization to study breakdown flows. Probe measurements are difficult to obtain in vortex breakdown as the phenomenon is sensitive to small flow perturbations. Breakdown zones have been observed

to disappear when a pitot tube is inserted into the flow upstream of the disturbance [Harvey 1962]. By injecting smoke through the vane centerbody along the centerline of the pipe, Harvey showed that it is possible to observe vortex breakdown in an internal flow device.

A significant experimental study of vortex breakdown conducted after Harvey was by Sarpkaya [1971a, 1971b]. Sarpkaya's flow apparatus was similar in design to Harvey's and is also represented by Figure 2.1. Using water as the experimental fluid, Sarpkaya's objective was to study the dependence of vortex breakdown on swirl velocity and Reynolds number. The swirl level was reported using a non-dimensional swirl number, a ratio of the swirl velocity at the tube wall to the average axial velocity.

The main approach taken by Sarpkaya was to vary the swirl number at fixed Reynolds number. When this was done, the first breakdown observed was a spiral type. This spiral breakdown was characterized by a stagnation point on the pipe centerline, followed by a fold in the dye filament which rotated down the pipe soon breaking into turbulence, as shown in Figure 2.2. When the swirl was increased, one of two things occurred depending on the rate of swirl increase.

The first breakdown resulting from an increase in swirl was the double helix form, see Figure 2.3. Originally Sarpkaya identified this as a new form of breakdown, but it is now considered to be a type of instability which does not involve a stagnation point on the axis or a region of flow reversal [Sarpkaya 1971b].

The second breakdown form evolving from the spiral type was an axisymmetric bubble type of breakdown, as shown in Figure 2.4. The central

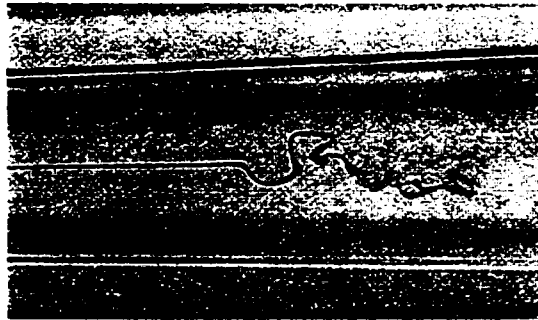


Figure 2.2: Spiral Vortex Breakdown. Reprinted with permission from Faler and Leibovich [1977]. *Physics of Fluids* 9 p. 1391



Figure 2.3: Double Helix Vortex Breakdown. Reprinted with permission from Faler and Leibovich [1977]. *Physics of Fluids* 9 p. 1394

dye filament decelerates along the tube axis, eventually stagnating. The filament then shears over a bubble form in the flow. The bubble is an area of recirculating fluid which is both filled and emptied from the rear.

For all three breakdowns observed by Sarpkaya, the location of the breakdown was moved upstream by increasing either Reynolds number or swirl number, and moved downstream by decreasing these parameters. The Reynolds number affects the breakdown indirectly by changing the radius of the vor-

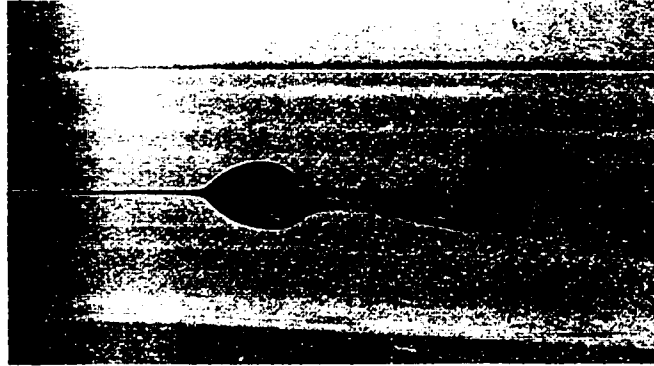


Figure 2.4: Axisymmetric Vortex Breakdown. Reprinted with permission from Faler and Leibovich [1977]. *Physics of Fluids* 9 p. 1389

tical core. A higher Reynolds number leads to a thinner boundary layer forming on the vane centerbody, which leads to a thinner vortical core. For fixed circulation, or swirl vane angle, this leads to an increase in the core vorticity, which is the same affect as increasing the swirl [Leibovich 1978].

Sarpkaya observed transient behavior of a breakdown zone to changes in swirl number. If the swirl number was increased, the breakdown would initially move downstream, before moving upstream and downshooting it's final expected location. The disturbance then moved slowly back to its final mean location. Under steady flow conditions, the breakdown was also observed to be quasi-steady in position, fluctuating axially about a mean location.

Sarpkaya [1974] also studied the effect of an adverse pressure gradient or a divergence of streamsurfaces on the onset of breakdown. It was found that for pipe divergence angles that did not cause boundary layer separation along the tube walls and at a given swirl number and Reynolds number, the application of an adverse pressure gradient moved the breakdown upstream.

It was also shown that in the presence of an adverse pressure gradient, lower swirl and Reynolds numbers were required to precipitate breakdown.

Faler and Leibovich [1977a, 1977b] conducted a thorough experimental investigation of vortex breakdown. Their apparatus was similar in design to that of Sarpkaya, Figure 2.1, and they found three of the same breakdown flows. In Faler and Leibovich's taxonomy, the various breakdown flows are assigned numbers. Type 0 and Type 1 breakdowns are similar to Sarpkaya's axisymmetric breakdown, Type 2 breakdown is Sarpkaya's spiral breakdown and Type 5 is the double helix form. In addition to these, Faler and Leibovich found three more disturbances which can be classified as breakdowns. Following is a description of the evolution of these flows as the swirl number is increased.

At a fixed Reynolds number and with no swirl velocity, Faler and Leibovich observed the central dye filament travelling down the tube with no visible change. As the swirl was increased, small oscillations were reported at the end of the uniform diameter exit section. Further swirl increases caused these oscillations to travel upstream to the exit of the divergent test section. Faler and Leibovich's Type 6 breakdown was observed when the swirl number was increased from this level.

The Type 6 disturbance, Figure 2.5, was observed in the divergent test section and was characterized by the central dye filament moving off of the tube axis. The filament did not acquire the spiraling motion of the base flow until it had moved off the tube axis by approximately half of a tube radius.

Faler and Leibovich's Type 5 breakdown is the double helix form observed by Sarpkaya, Figure 2.3, and it occurred when the swirl level was increased

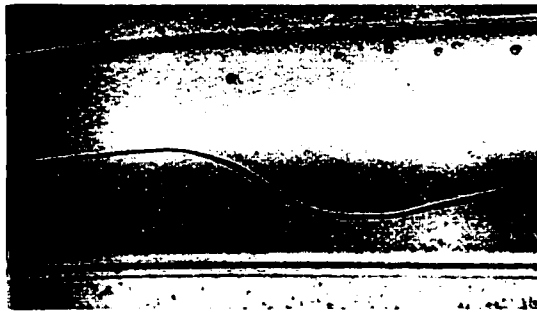


Figure 2.5: Type 6 Vortex Breakdown. Reprinted with permission from Faler and Leibovich [1977]. *Physics of Fluids* 9 p. 1393

from the Type 6 level. A visual comparison of Figure 2.3 and Figure 2.5 indicates that a Type 5 breakdown is structurally similar to a Type 6 breakdown with the central dye filament shearing into two branches. This observation led Faler and Leibovich to conclude that the Type 5 breakdown is the same as a Type 6 breakdown.

The Type 4 breakdown, Figure 2.6, was observed to form when the swirl number was increased from the Type 5 swirl level. This disturbance is similar to the bubble breakdown observed by Sarpkaya, except that it is not rotationally symmetric. The Type 4 bubble was observed to be approximately 3 times as wide as it was thick.

The Type 3 breakdown, Figure 2.7, was observed to contain some characteristics of both Sarpkaya's spiral breakdown form and the Type 4 breakdown. The central dye filament decelerated and folded as observed in spiral breakdown, but some of the dye spread laterally and marked the outline of a Type 4 bubble.

Type 2 breakdown corresponds to Sarpkaya's spiral breakdown, Figure



Figure 2.6: Type 4 Vortex Breakdown. Reprinted with permission from Faler and Leibovich [1977]. *Physics of Fluids* 9 p. 1394



Figure 2.7: Type 3 Vortex Breakdown. Reprinted with permission from Faler and Leibovich [1977]. *Physics of Fluids* 9 p. 1395

2.2. Again this was characterized by deceleration of the flow on the axis and the central dye filament forming an abrupt fold. The filament then spirals out for a few turns with the same sense of rotation as the base flow before turning into turbulence.

Faler and Leibovich found three variations of the axisymmetric bubble breakdown. The first bubble type breakdown observed by Faler and Leibovich was named Type 1, Figure 2.8, and was similar to Sarpkaya's bubble breakdown in its general appearance. However, the front end of this form had slight asymmetries and the emptying region did not return to the tube

axis, but seemed to break up into large scale turbulence.

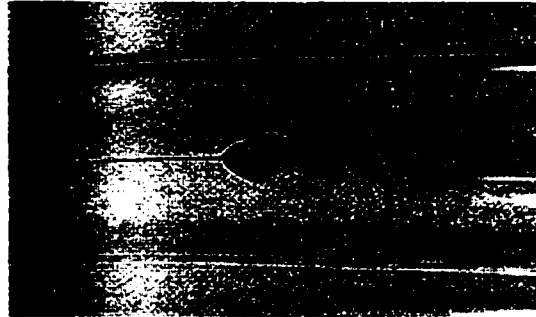


Figure 2.8: Type 1 Vortex Breakdown. Reprinted with permission from Faler and Leibovich [1977]. *Physics of Fluids* 9 p. 1391

The other two forms of axisymmetric breakdown observed by Faler and Leibovich are collectively known as Type 0 breakdown. The more common of these two forms corresponds to Sarpkaya's axisymmetric breakdown, Figure 2.4. This breakdown was characterized by a single emptying region. Filling and emptying took place in accordance with Sarpkaya's observations. The rotating emptying tail was followed by a spiral type breakdown. The less frequently observed Type 0 breakdown consisted of two emptying regions, Figure 2.9. The two emptying regions were diametrically opposed as were the two filling points. The emptying and filling regions were 90° out of phase. The Type 0 and Type 1 breakdowns were observed to spontaneously transform into one another with no change in the swirl number or Reynolds number.

When a dye filament was introduced off axis into a Type 2 breakdown flow, it became disrupted about a tube radius ahead of the main disturbance. If the Reynolds number or the swirl number was increased the main distur-

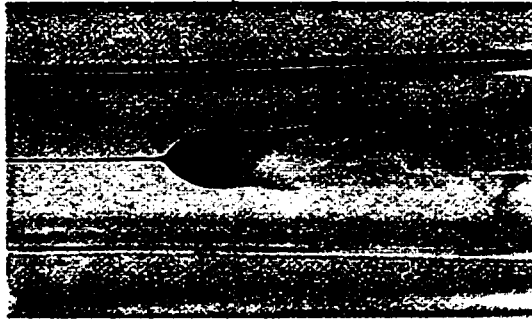


Figure 2.9: Two Tailed Type 0 Vortex Breakdown. Reprinted with permission from Faler and Leibovich [1977]. *Physics of Fluids* 9 p. 1390

bance would move ahead of the off axis disturbance. This is in contrast to the axisymmetric breakdowns (Type 0 and 1) which always occurred before the off axis filament was disturbed and the Type 3 to 6 disturbances which always occurred after the off axis filament was disturbed.

Faler and Leibovich observed the same movements of the breakdown zone to changes in the swirl number and Reynolds number as described by Sarpkaya. A notable difference between the two studies is the order in which some of the disturbances evolved. Faler and Leibovich observed the double helix, Type 5, always forming from Type 6 either spontaneously or with an increase in Reynolds number or swirl, and sometimes spontaneously from a Type 4. Type 4 was always succeeded by Type 3 which led to Type 2 and eventually Types 0 and 1. Sarpkaya reported that the double helix (Type 5) formed as an intermediate step between spiral (Type 2) and axisymmetric breakdowns (Types 0 and 1). In general, no rules can be applied to predict which breakdown forms will appear under specified flow conditions [Escudier 1988]. Indeed, although the aforementioned sequence of breakdown forms

was generally noticed by Sarpkaya and Faler and Leibovich respectively, it was observed that Type 0 and 1 and Type 2 breakdowns could spontaneously change into one another.

Faler and Leibovich's study was the first instance of velocity measurements being taken throughout a breakdown flowfield. These measurements were obtained with the aid of a Laser Doppler Anemometer, and result in the flowfield, just downstream of the vane centerbody, described by equations (2.1) to (2.3):

$$v_r = 0 \quad (2.1)$$

$$v_z = V_{z1} + V_{z2} \exp\left(-\alpha \left(\frac{r}{R}\right)^2\right) \quad (2.2)$$

$$v_\theta = V_{\theta1} \left(\frac{R}{r}\right) \left[1 - \exp\left(-\alpha \left(\frac{r}{R}\right)^2\right)\right] \quad (2.3)$$

where V_{z1} , V_{z2} , $V_{\theta1}$ and α are constants and R the tube radius.

It is accepted that the two basic types of vortex breakdown are the spiral and axisymmetric modes. The question over which mode is more fundamental is still open to debate. The theoretical approach taken towards breakdown depends in large part on the answer to this question. In their experimental investigation of the development of breakdown modes, Bruecker and Althaus [1995] use particle tracking velocimetry to address this problem. Using a significantly lower Reynolds number than Sarpkaya and Faler and Leibovich, Bruecker and Althaus observed a spiral breakdown forming from a bubble breakdown. By examining selected streamlines from both forms, they came to the conclusion that spiral and axisymmetric breakdowns are topologically similar. Furthermore, they observed that the spiral mode forms as a result of growing asymmetries in the initial bubble. From these observations, Bruecker

and Althaus concluded that the axisymmetric bubble breakdown is the more fundamental phenomenon.

A theoretical model of vortex breakdown should match or explain some of the observations reported here. The more notable of these observations are summarized:

- The different forms of breakdown can transform into one another without altering the swirl number or Reynolds number.
- Increasing Reynolds number, swirl number and the adverse pressure gradient causes the disturbance to move upstream.
- The initial movement of the disturbance to a change in Reynolds number or swirl number, is in the opposite direction to that expected.
- Breakdown seems to be initiated and altered by increasing the swirl of the incoming flow.
- The spiral breakdown's (Type 2) role as an intermediate form between Types 3-6 and Types 0 and 1.

2.2 Theoretical Review

Shortly after Peckham and Atkinson first observed vortex breakdown in 1957, several different theoretical explanations were presented. Generally the theories can be called; Wave Models, Instability Models, and Quasi-Cylindrical Models. Initially it was thought that all three of these theories were inherently different, but more recent analysis has shown them to be related [Wang and Rusak 1997]. In this section, the three models will briefly be discussed.

2.2.1 Wave Theory

The central idea in the wave theory of vortex breakdown is the concept of a critical state. A subcritical flow can sustain infinitesimal standing waves, while a supercritical flow cannot. The critical state marks the boundary of these two states, and in this condition a flow can sustain infinitesimal disturbances of indefinite wavelength. A clear mathematical description of these definitions can be found in Benjamin [1962]. The definition relies upon the assumptions of inviscid, steady, axisymmetric flow. Furthermore, the flow is assumed to have a small radial velocity component and little variation in the axial direction, such flows are called quasi-cylindrical.

Squire [1960] introduced the concept of a critical state into vortex breakdown theory. In his paper he considered only the critical state, and searched for conditions on the axial and swirl velocity for which a flow could first sustain standing waves. Squire's theory was that when a flow can sustain a standing wave, disturbances created downstream can travel up the vortex core causing breakdown. For three different swirl distributions, Squire found that the Helix angle should be greater than 50° . It was this data that Harvey used to guide his experimental work.

Benjamin [1962] proposed that vortex breakdown is a transition from a supercritical upstream flow to a subcritical downstream flow akin to a hydraulic jump or a shock wave. Benjamin showed that subcritical flows have greater flow force than supercritical flows. Flow force is defined as the sum of horizontal momentum flux and pressure force per unit length. He postulated that to conserve momentum, a standing wavetrain forms on the subcritical flow. Benjamin believed that this wavetrain is the vortex breakdown. This

idea of wave dissipation would apply only when the difference in flow force is small, for large differences turbulence is a more likely dissipation mechanism. This is a weakness in his theory, as is the fact that his definition of conjugate flows (supercritical/subcritical) applies only to small perturbations. Vortex breakdown is a large amplitude nonlinear phenomenon.

As outlined in the Experimental Review section of this thesis, the location of a vortex breakdown moves upstream in response to an increase in swirl velocity and moves downstream in response to a decrease in swirl velocity. A strength of the wave theory is its ability to explain this movement of the breakdown zone to changes in swirl level [Faler and Leibovich 1977a]. The vortex breakdown location is fixed in space if its upstream propagation speed vanishes with respect to the laboratory frame. From the wave theory, the upstream wave propagation speed is found to increase for increases in swirl and decrease with an increase in axial velocity. When the swirl is increased the upstream wave speed increases causing the breakdown to convect upstream. As the breakdown moves upstream however, it sees a converging pipe which increases the axial velocity. The increase in axial velocity causes the upstream wave speed to decrease. Eventually the breakdown comes to a new equilibrium position upstream of its old one.

2.2.2 Quasi-Cylindrical Theory

The wave theories of vortex breakdown were analogous to the hydraulic jump and shock waves from other branches of fluid mechanics. Likewise, the Quasi-Cylindrical theory is analogous to the parabolizing of the Navier Stokes equations in boundary layer theory. Quasi-cylindrical flow implies

slow axial gradients and approximately cylindrical stream surfaces.

The Quasi-Cylindrical theories propose that vortex breakdown occurs where the quasi-cylindrical equations become singular. At a vortex breakdown, which is characterized by a rapid flow deceleration along the pipe axis of symmetry, the assumptions of slow axial gradients and cylindrical stream surfaces are not valid [Hall 1972]. The physical mechanism for flow deceleration can be shown to depend on the magnitude of the swirl velocity. Specifically, the pressure gradient along the axis is greater than that outside of the vortex core by an amount depending on the square of the circulation [Hall 1972]:

$$\left(\frac{\partial P}{\partial z}\right)_{r=0} = \left(\frac{\partial P}{\partial z}\right)_{r=R} + \rho k \frac{\Gamma^2}{R^3} \quad (2.4)$$

Hall performed numerical calculations based on this theory. He predicted the location of breakdown to within one and a half diameters of the vortex core. Furthermore, a sensitivity study of the quasi-cylindrical equations showed that the location of failure depends, at least qualitatively, on the parameters of swirl number and pressure gradient in the same way as experimental breakdown flows.

It has been shown that when the solution to the quasi-cylindrical equations fail, the flow shows a fall from supercritical to subcritical conditions. In fact, Trigub [1985] has shown that the singular state of the quasi-cylindrical equations is the same as the critical state defined in the wave theory. This is not surprising as the wave theory also invokes a quasi-cylindrical assumption.

2.2.3 Instability Theory

Another theory which was initially proposed to explain vortex breakdown is that of hydrodynamic instability [Ludweig 1962,1965]. Ludweig claimed that vortex breakdown is a direct consequence of instability to spiral type disturbances. He calculated a stability boundary for swirling flow in an annulus and postulated that this should be a necessary condition for stability in high Reynolds number flows. Ludweig said that after the instability has developed, it may induce asymmetry in the vortex core which could lead to stagnation.

The main criticism of this theory lies in the fact that spiral asymmetry is never observed upstream of breakdown. This would indicate that the flow is not becoming unstable prior to breakdown. Furthermore, using the traditional stability analysis of Lessen et. al. [1974], Leibovich [1977a] showed that all of the approach flows used in his experiments were marginally stable to axisymmetric and asymmetric disturbances.

Due to the difficulties involved in any stability analysis, the role of stability in vortex breakdown is not clear. Flows have been observed to break down with no sign of instability, and many unstable swirling flows do not undergo breakdown [Leibovich 1984]. The traditional analysis put forth by Lessen et. al. [1974] dealt with flow in an infinite pipe. Wang and Rusak [1996] have recently conducted a stability analysis for swirling flow in a finite length pipe and have used their results to guide a new theory of vortex breakdown [Wang and Rusak 1997].

Using inviscid, axisymmetric flow in a circular finite length duct as their starting point, Wang and Rusak [1997] showed that the critical swirl level

defined by Benjamin [1962] is a point of exchange of stability for columnar swirling flows. When a flow is supercritical, all disturbances are convected out of the flow domain. When the flow is subcritical, disturbances can travel upstream and interact with the inlet conditions in a nonlinear instability which forms a breakdown. The disturbances Wang and Rusak discuss can travel to the inlet since a uniform duct is considered in their work. Their results can be interpreted in terms of a diverging duct when the effect of this geometry on wave propagation is considered. Experimentally observed breakdowns are supercritical upstream and subcritical downstream of the breakdown zone. In a diverging duct, the flow will be supercritical at the high axial velocity found at the inlet. As the flow decelerates down the diverging duct, the upstream wave propagation speed increases and subcritical conditions will soon develop. It is at this supercritical/subcritical station that breakdown will occur. The theory of Wang and Rusak is an extension of Benjamin's theory. The inclusion of an instability removes the small disturbance drawbacks of Benjamin's theory.

Popper [1969] put forth several criteria that any explanatory theory should satisfy. A theory should not only correspond to known facts, it should evolve from a simple unifying idea, have explanatory power, explain all interesting aspects of a phenomenon and have a high degree of refutability. Based on this criteria, no theory of vortex breakdown is yet complete.

2.3 Computational Review

Many computational studies into vortex breakdown have been conducted. Early simulations were limited by computing resources and were capable of

capturing only first order effects. Other early numerical studies, such as Grabowski and Berger [1976], predicted breakdown occurring near the inlet plane of the computational domain. The accuracy near a boundary of any numerical simulation is limited by the accuracy with which the boundary condition approximates the physical flow. If the boundary condition is not an exact solution of the equations being solved there must exist a region of adjustment in which an exact solution to the equations develops. Flow phenomena observed in this development region may be generated by the boundary condition and not by a physical mechanism. Furthermore, it is possible that any disturbance occurring near a boundary may affect the boundary condition creating a non physical temporal disturbance.

Darmofal [1996], conducted a numerical experiment into the validity of the axisymmetric assumption of vortex breakdown. To make a comparison between experiment and computation, Darmofal choose to use Faler and Leibovich's [1977b] data. This data encompasses breakdown flows at many Reynolds and swirl numbers so that several flow situations can be compared. Faler and Leibovich's test apparatus is shown in Figure 2.1. The use of a straight pipe followed by a diverging test section isolates the vortex breakdown from occurring near the pipe inlet. Using a similar domain in his computational work also allowed Darmofal to isolate the breakdown from the pipe inlet.

Darmofal solved the incompressible axisymmetric Navier Stokes equations in vorticity streamfunction form using a finite volume algorithm with four stage Runge Kutta time stepping. The details of this second order accurate method can be found in Jameson et. al. [1981].

For three different Reynolds number/swirl number combinations, Darmofal predicted the location of the breakdown. Although the calculation was unsteady, and experimental breakdowns are unsteady in position, a steady breakdown location was predicted by the simulation. An examination of Faler and Leibovich's experiments shows that the location of breakdown is very sensitive to inlet conditions. It is likely that the numerical/experimental discrepancy can be attributed to the lack of periodic fluctuations in the inlet boundary condition and not to a failure of the axisymmetric assumption.

Darmofal also looked at a specific Reynolds number/swirl number combination for comparison with Faler and Leibovich's detailed vortex breakdown velocity field. The overall structure of the computational bubble was very similar to the experimental bubble. The calculated velocity values in the upstream half of the bubble were found to be only 10% in error. The downstream portion of the bubble and the wake flow showed relatively larger discrepancies with the experimental values. Darmofal's interpretation of this was that the mechanism leading to axisymmetric breakdown flows is inherently axisymmetric, but the breakdown itself is unstable to nonaxisymmetric disturbances. This would lend credence to the theoretical models which begin with the assumption of axisymmetry.

Beran and Culick [1992] utilized numerical simulations in a different manner than Darmofal. Using a Newton iteration technique in conjunction with arc length continuation, they managed to show that vortex breakdown is related to the existence of nonunique solutions of the Navier Stokes equations.

Like Darmofal, Beran and Culick wrote the equations of motion in vorticity streamfunction form, and a straight pipe to diverging pipe type of flow

domain was utilized to remove the effects of the inlet on the breakdown zone. The inlet swirl level was used as the free parameter onto which continuation was applied, and the minimum axial velocity on the axis of symmetry used as a representation of a particular solution. When the minimum axial velocity was plotted as a function of swirl level, two limit points were found. By also solving the quasi-cylindrical equations, Beran and Culick were able to show that the first limit point corresponds to the point at which the quasi-cylindrical approximation fails. This is also the point at which the flow becomes critical. Reversed flow was not observed until after this point, which is in accordance with Leibovich [1989], who said that a flow must first become subcritical to axisymmetric disturbances before the point at which stagnation is observed.

More recent computations using the unsteady Navier Stokes equations by Beran [1994] and Lopez [1994], have shown that the region between the first and second limit points is unstable. It is a physically unrealizable solution, which will not evolve from any initial flow.

Another observation from Beran and Culick's work was that for large Reynolds numbers, three different forms of flow could be observed. These three flow forms; columnar, solitary wave and wave train correspond to three types of flow found to exist in inviscid problems [Leibovich and Kribus 1990]. The relationship of these viscous flows to their inviscid counterparts has been used to support the inviscid assumption in theoretical vortex breakdown work [Wang and Rusak 1997].

As can be seen from the summary given in this section, the use of CFD techniques has much to add to the study of vortex breakdown. Darmofal's

numerical simulations support the use axisymmetric equations when studying vortex breakdown. Beran and Culick supplied evidence that the underlying mechanism causing vortex breakdown is inviscid.

2.4 Vorticity Dynamics in Vortex Breakdown

The vorticity in internal flow vortex breakdown is generated through boundary layer effects. The boundary layer shed from the vane centerbody forms the vortex core, outside of which the flow is approximately irrotational.

The vorticity in the flow upstream of vortex breakdown is aligned in the axial direction [Spall et. al. 1990]. Brown and Lopez [1990] have examined the evolution of the vorticity as the breakdown zone is approached, and concluded that vortex breakdown flows are always accompanied by the tilting of the axial vorticity into the negative azimuthal direction.

By looking at the equation governing the azimuthal vorticity in axisymmetric flow, Brown and Lopez derived a new criteria for breakdown to occur. The equation governing azimuthal vorticity can be written as:

$$\frac{\omega_\theta}{\omega_{\theta o}} = \frac{r_o}{r} \left(\frac{\lambda_o}{\beta_o} \right) - \frac{r}{r_o} \left(\frac{\lambda_o}{\beta_o} - 1 \right) \quad (2.5)$$

This equation shows that for breakdown to occur (i.e. $-\omega_\theta$) the swirl number of the velocity ($\lambda_o = \frac{v_\theta}{v_z}$) must be greater than the swirl number of the vorticity ($\beta_o = \frac{\omega_\theta}{\omega_z}$) at some initial location on a diverging streamline (i.e. $r > r_o$). Brown and Lopez proposed that the diverging streamlines were initially created by a diffusion of the axial vorticity outwards. Once the radial velocity has been initiated they proposed that an inviscid mechanism

of tilting and stretching of vortex lines governs the evolution of the axial vorticity.

Darmofal [1993] expanded upon this inviscid azimuthal vorticity generation mechanism. The equation governing vorticity can be written as:

$$\frac{D\omega_\theta}{Dt} = \omega_r \frac{\partial v_\theta}{\partial r} + \omega_z \frac{\partial v_\theta}{\partial z} - \frac{v_\theta \omega_r}{r} + \frac{v_r \omega_\theta}{r} \quad (2.6)$$

Using the definition of vorticity this equation can be rewritten as:

$$\frac{D\omega_\theta}{Dt} = \frac{\partial}{\partial z} \left(\frac{\Gamma^2}{r^3} \right) + \frac{v_r \omega_\theta}{r} \quad (2.7)$$

where $\Gamma = rv_\theta$. For steady inviscid flow this can be restated in terms of the streamfunction as follows:

$$\frac{D\omega_\theta}{Dt} = -\frac{v_r}{r^2} \frac{d(\Gamma^2)}{d\Psi} + \frac{v_r \omega_\theta}{r} \quad (2.8)$$

The first term on the right hand side of equation (2.8) contains the three vortex tilting terms on the right hand side of equation (2.6). This means that a non-zero radial velocity or axial gradient of circulation results in the tilting of the axial and radial vorticity components into azimuthal vorticity. For vortex breakdown flows it is noticed that $\frac{d(\Gamma^2)}{d\Psi} \geq 0$, so that a positive radial velocity always causes a reduction in azimuthal vorticity [Darmofal 1993]. Once the azimuthal vorticity has become negative, the vortex stretching term in equation (5.6) creates more negative ω_θ , and a further deceleration of the axial flow along the axis.

When the axial velocity decelerates along the pipe axis, mass conservation requires that a positive radial velocity develops. From equation (2.8) the increased radial velocity will create more negative azimuthal vorticity which

will in turn decelerate the flow on the axis of symmetry. Vortex breakdown has been identified as a rapid structural change, and the the vorticity dynamics description of the breakdown process also describes a rapidly evolving flowfield.

As was discussed in the Experimental Review section (Section 2.1), vortex breakdown depends most significantly on the magnitude of the swirl number and an adverse pressure gradient in the flow. Starting with Hall's pressure equation (2.4) and using Darmofal's azimuthal velocity equation (2.8) we get [Darmofal 1993]:

$$\left(\frac{\partial P}{\partial z}\right)_{r=0} = \left(\frac{\partial P}{\partial z}\right)_{r=R} - \rho \int_r^\infty \frac{D\omega_\theta}{Dt} dr \quad (2.9)$$

From equation (2.9) it can be seen that the production of negative azimuthal vorticity is connected to the creation of an adverse pressure gradient. This is interesting for two reasons. First, the vorticity approach to problems normally does not involve the pressure field, but here we have a connection between vorticity dynamics and the more common momentum approach to problems. More importantly, in equation (2.9) we have a connection between the vorticity dynamics theory of vortex breakdown and the quasi-cylindrical theory of breakdown.

Spall et. al. [1991] performed a three dimensional numerical simulation of vortex breakdown. They observed the vorticity field upstream of the vortex breakdown being aligned mainly in the axial direction. They also saw this vorticity becoming stretched and tilted into both the radial and azimuthal directions as the breakdown zone was approached.

Spall et. al. [1991] also calculated the enstrophy of vortex breakdown flows. Enstrophy is an absolute measure of the amount of vorticity present

in a fluid region. They found that the governing influence over enstrophy was vortex stretching and tilting, viscous effects were secondary. They showed that in some regions of the flow inviscid effects are not as important as the viscous effects. In these isolated regions, viscous effects likely govern the flow. (i.e. flow inside the bubble). These observations are supported by inviscid calculations of breakdown which correctly predict an axial velocity stagnation, but which do not predict a breakdown bubble structure in agreement with experimental results.

CHAPTER 3

MATHEMATICAL MODEL

3.1 General Form of Governing Equations

The governing equations for a constant energy flow are the conservation of mass and momentum. They are shown below in integral form for a volume Ω bounded by a surface W :

$$\frac{\partial}{\partial t} \int_{\Omega} \rho d\Omega + \int_W \rho (\bar{v} \cdot \bar{n}) dW = 0 \quad (3.1)$$

$$\frac{\partial}{\partial t} \int_{\Omega} \bar{v} \rho d\Omega + \int_W \bar{v} \rho (\bar{v} \cdot \bar{n}) dW = \int_{\Omega} \rho \bar{F} d\Omega + \int_W \bar{R} dW \quad (3.2)$$

By applying the Divergence Theorem and Reynolds Transport Theorem to equations (3.1) and (3.2) [Panton 1996] it is possible to write them in differential form.

$$\frac{\partial \rho}{\partial t} + \nabla \cdot (\rho \bar{v}) = 0 \quad (3.3)$$

$$\rho \frac{D\bar{v}}{Dt} = \rho \nabla (gr \sin \theta) - \nabla P + \nabla \cdot \tau \quad (3.4)$$

where:

$$\frac{D}{Dt} = \frac{\partial}{\partial t} + v_r \frac{\partial}{\partial r} + \frac{v_{\theta}}{r} \frac{\partial}{\partial \theta} + v_z \frac{\partial}{\partial z} \quad (3.5)$$

$$\nabla = \frac{\partial}{\partial r} \hat{e}_r + \frac{1}{r} \frac{\partial}{\partial \theta} \hat{e}_\theta + \frac{\partial}{\partial z} \hat{e}_z \quad (3.6)$$

and a cylindrical co-ordinate system is defined in Figure 3.1.

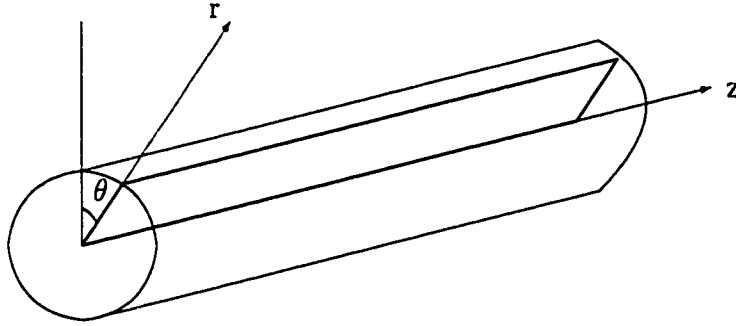


Figure 3.1: Cylindrical Co-ordinate System

This manipulation assumes that the surface stress is composed of a pressure stress and a viscous stress.

$$\bar{R} = \hat{n} (-P + \tau) \quad (3.7)$$

This formulation also assumes that only conservative body forces are present. In this instance, the only body force is gravity. For a cylindrical co-ordinate system, gravity can be written as a potential in the following manner:

$$\bar{F} = \nabla (gr \sin \theta) \quad (3.8)$$

The equations are written in differential form as these equations are simpler to manipulate than the integral form, but still apply to a wide class of problems.

3.2 Modification of Equations

3.2.1 Incompressible Flow

The incompressibility condition can be written as:

$$\nabla \cdot \bar{v} = 0 \quad (3.9)$$

For numerical simulations of incompressible flows it is beneficial to recast equation (3.3) into a new form so that the incompressibility condition can be satisfied explicitly. This is achieved by expanding the dot product and recollecting terms:

$$\frac{D\rho}{Dt} + \rho \nabla \cdot \bar{v} = 0 \quad (3.10)$$

The incompressibility condition (3.9) in conjunction with continuity (3.10) leads to the additional condition:

$$\frac{D\rho}{Dt} = 0 \quad (3.11)$$

3.2.2 Inviscid Flow

One of the major assumptions taken in this work is that vortex breakdown is an inviscid phenomenon. This assumption is supported in work conducted by previous investigators [Benjamin 1962, Leibovich and Kribus 1990, Brown and Lopez 1990, Darmofal 1993, Wang and Rusak 1997].

The success of the inviscid wave theory of vortex breakdown is one reason for neglecting viscosity in this model. This theory, outlined in Section 2.2.1, correctly predicts the unsteady motion of the breakdown zone in response to changes in Reynolds number and swirl number [Faler and Leibovich 1977a].

Spall et. al. [1991] conducted three dimensional, viscous calculations of vortex breakdown in an unbounded flow. They calculated the rate of change of enstrophy in these flows due to both vortex stretching (an inviscid process) and viscosity. They showed that in the flow upstream of a vortex breakdown, the total change in enstrophy (due to viscosity and vortex stretching) is governed by vortex stretching. This indicates that the initiation of vortex breakdown is governed by an inviscid mechanism. Darmofal's [1993] description of the inviscid evolution of vorticity in the flow approaching vortex breakdown, discussed in Section 2.4, agrees with the numerical observations made by Spall et. al. and also supports the use of an inviscid model for studying breakdown flows.

The axisymmetric, viscous calculations conducted by Beran and Culick [1992] were described in Section 2.3. In these calculations, a Newton iteration was performed with arc length continuation applied to the swirl level. The minimum axial velocity along the pipe axis was used as a representation of a flow solution. A bifurcation diagram of the minimum axial velocity plotted against the applied swirl velocity was found to have two limit points. The axial velocity along the pipe centerline was found to stagnate at a swirl velocity between the two limit points. Inviscid simulations conducted by Buntine and Saffman [1995] which also used a Burger vortex distribution for the swirl velocity and a jet profile for the axial velocity resulted in a

bifurcation diagram that closely matched the shape of Beran and Culick's up to the location of the axial velocity stagnation. The similar behavior of the viscous and inviscid calculations in the region approaching the stagnation point indicates that the mechanism creating vortex breakdown is inviscid.

It is believed that viscous effects are important in shaping and governing the flow inside the bubble region of vortex breakdown. In this work we are interested in predicting the occurrence of vortex breakdown in a flow and not the details of the flowfield, it is therefore reasonable to neglect viscosity in (3.4), giving:

$$\rho \frac{D\bar{v}}{Dt} = -\nabla P + \rho \nabla (gr \sin \theta) \quad (3.12)$$

3.2.3 Axisymmetric Flow

As discussed by Leibovich [1984], there are compelling arguments supporting both axisymmetric and asymmetric models of vortex breakdown. The most convincing evidence that breakdown is axisymmetric are the many numerical simulations of the axisymmetric Navier Stokes equations that have been conducted and which contained breakdown solutions [Kopecky and Torrance 1973, Grabowski and Berger 1976, Salas and Kuruvila 1989, Darmofal 1996]. Darmofal's simulations, which are discussed in Section 2.3, were conducted to test the validity of the axisymmetric assumption. By comparing the results of his computations to the experimental results of Faler and Leibovich [1977b], Darmofal concluded that the mechanism leading to vortex breakdown is axisymmetric.

Previous theoretical work in vortex breakdown has invoked the axisymmetric assumption [Benjamin 1962, Hall 1967, Darmofal 1993, Wang and

Rusak 1997]. As discussed in Section 2.2.1, the wave theory of vortex breakdown successfully predicts the movement of breakdown zones to changes in Reynolds number and swirl number [Leibovich 1977a]. The axisymmetric quasi-cylindrical theory of Hall [1967], described in Section 2.2.2, correctly predicts the location of vortex breakdown to within one and a half diameters of the vortex core. The axisymmetric vorticity dynamics approach to vortex breakdown [Darmofal 1993] summarized in Section 2.4, qualitatively describes the tilting and stretching of the vorticity leading to a vortex breakdown that Spall et. al. [1991] observed in their three dimensional numerical calculations.

To obtain axisymmetric equations, previous investigators of vortex breakdown have neglected the azimuthal derivative terms found in the Navier Stokes or Euler equations [Benjamin 1962, Batchelor 1967, Beran and Culick 1992]. Axisymmetric equations can be derived by averaging the governing equations over the azimuth. The resulting equations consist of the axisymmetric equations and a group of correlations which contain three dimensional effects.

To obtain the axisymmetric averaged set of equations, the flowfield is first assumed to be composed of an axisymmetric averaged component, and a three dimensional perturbation. For example, the velocity field can be written as:

$$\bar{v}(r, \theta, z) = \bar{\bar{v}}(r, z) + \bar{v}'(r, \theta, z) \quad (3.13)$$

The averaging procedure involves substituting equation (3.13), along with similar equations for the pressure and density, into equation (3.12). This

equation is then averaged utilizing the definition of an azimuthal average:

$$\bar{T}(r, z) = \frac{1}{2\pi} \int_0^{2\pi} T(r, \theta, z) d\theta \quad (3.14)$$

When this procedure is carried out in a term by term manner the following equations result:

$$\bar{\rho} \left(\frac{\partial \bar{v}_r}{\partial t} + \bar{v}_r \frac{\partial \bar{v}_r}{\partial r} + \bar{v}_z \frac{\partial \bar{v}_r}{\partial z} - \frac{\bar{v}_\theta^2}{r} \right) = -\frac{\partial \bar{P}}{\partial r} - \frac{2\rho g}{\pi} - \sum_{i=1}^5 \Lambda_i \quad (3.15)$$

$$\bar{\rho} \left(\frac{\partial \bar{v}_\theta}{\partial t} + \bar{v}_r \frac{\partial \bar{v}_\theta}{\partial r} + \bar{v}_z \frac{\partial \bar{v}_\theta}{\partial z} + \frac{\bar{v}_\theta \bar{v}_r}{r} \right) = -\sum_{i=1}^5 \Sigma_i \quad (3.16)$$

$$\bar{\rho} \left(\frac{\partial \bar{v}_z}{\partial t} + \bar{v}_r \frac{\partial \bar{v}_z}{\partial r} + \bar{v}_z \frac{\partial \bar{v}_z}{\partial z} \right) = -\frac{\partial \bar{P}}{\partial z} - \sum_{i=1}^5 \Phi_i \quad (3.17)$$

where for example:

$$\Lambda_1 = \overline{\rho' \frac{\partial v_r'}{\partial t}} + \overline{\bar{\rho} v_r' \frac{\partial v_r'}{\partial r}} + \overline{\rho' \bar{v}_r \frac{\partial v_r'}{\partial r}} + \overline{\rho' v_r' \frac{\partial \bar{v}_r}{\partial r}} + \overline{\rho' v_r' \frac{\partial v_r'}{\partial r}} \quad (3.18)$$

$$\Lambda_2 = \frac{\overline{\bar{\rho} v_\theta' \frac{\partial v_r'}{\partial \theta}}}{r} + \frac{\overline{\rho' \bar{v}_\theta \frac{\partial v_r'}{\partial \theta}}}{r} + \frac{\overline{\rho' v_\theta' \frac{\partial v_r'}{\partial \theta}}}{r} + \frac{\overline{\bar{\rho} \bar{v}_\theta \frac{\partial v_r'}{\partial \theta}}}{r} \quad (3.19)$$

$$\Lambda_3 = \overline{\bar{\rho} v_z' \frac{\partial v_r'}{\partial z}} + \overline{\rho' \bar{v}_z \frac{\partial v_r'}{\partial z}} + \overline{\rho' v_z' \frac{\partial \bar{v}_r}{\partial z}} + \overline{\rho' v_z' \frac{\partial v_r'}{\partial z}} \quad (3.20)$$

$$\Lambda_4 = \frac{\overline{\bar{v}_\theta \rho' v_\theta'}}{r} + \frac{\overline{\bar{\rho} v_\theta' v_\theta'}}{r} + \frac{\overline{\rho' \bar{v}_\theta v_\theta'}}{r} + \frac{\overline{\rho' v_\theta' v_\theta'}}{r} \quad (3.21)$$

$$\Lambda_5 = \frac{1}{\pi} \int_0^\pi \rho' g \sin \theta d\theta \quad (3.22)$$

The Λ, Σ, Φ , and gravity terms can be viewed as three dimensional correction terms to the axisymmetric equation, which when included and modelled correctly, give a closer approximation to the three dimensional solution. When the Λ, Σ, Φ and gravity terms are neglected, equations (3.15) to (3.17) reduce to the standard axisymmetric Euler equations.

This work shall deal with the simpler axisymmetric equations:

$$\bar{\rho} \left(\frac{\partial \tilde{v}_r}{\partial t} + \tilde{v}_r \frac{\partial \tilde{v}_r}{\partial r} + \tilde{v}_z \frac{\partial \tilde{v}_r}{\partial z} - \frac{\tilde{v}_\theta^2}{r} \right) = -\frac{\partial \tilde{P}}{\partial r} \quad (3.23)$$

$$\bar{\rho} \left(\frac{\partial \tilde{v}_\theta}{\partial t} + \tilde{v}_r \frac{\partial \tilde{v}_\theta}{\partial r} + \tilde{v}_z \frac{\partial \tilde{v}_\theta}{\partial z} + \frac{\tilde{v}_\theta \tilde{v}_r}{r} \right) = 0 \quad (3.24)$$

$$\bar{\rho} \left(\frac{\partial \tilde{v}_z}{\partial t} + \tilde{v}_r \frac{\partial \tilde{v}_z}{\partial r} + \tilde{v}_z \frac{\partial \tilde{v}_z}{\partial z} \right) = -\frac{\partial \tilde{P}}{\partial z} \quad (3.25)$$

The correlation terms may be added in a future study. Tilde overbars shall be dropped in all future equations where it is understood that all terms are axisymmetric.

3.3 Clebsch Decomposition

The axisymmetric equations can be written in vector form as

$$\rho \frac{D\bar{v}}{Dt} = -\nabla P \quad (3.26)$$

Where ρ , \bar{v} and P are all functions of only r and z . Yokota [1998] has developed a complex lamellar approach to solving two dimensional stratified flow problems in a cartesian co-ordinate system. The method employed here parallels that of Yokota.

The velocity vector field can be decomposed into potential and complex lamellar components such as [Aris 1962]:

$$\bar{v} = \nabla \phi + A \nabla B + C \nabla D + E \nabla F + G \nabla H \quad (3.27)$$

Expanding equation (3.27) yields:

$$v_r = \frac{\partial \phi}{\partial r} + A \frac{\partial B}{\partial r} + C \frac{\partial D}{\partial r} + E \frac{\partial F}{\partial r} + G \frac{\partial H}{\partial r} \quad (3.28)$$

$$v_\theta = \frac{1}{r} \frac{\partial \phi}{\partial \theta} + \frac{A}{r} \frac{\partial B}{\partial \theta} + \frac{C}{r} \frac{\partial D}{\partial \theta} + \frac{E}{r} \frac{\partial F}{\partial \theta} + \frac{G}{r} \frac{\partial H}{\partial \theta} \quad (3.29)$$

$$v_z = \frac{\partial \phi}{\partial z} + A \frac{\partial B}{\partial z} + C \frac{\partial D}{\partial z} + E \frac{\partial F}{\partial z} + G \frac{\partial H}{\partial z} \quad (3.30)$$

For a flowfield to be axisymmetric, it is necessary that equations (3.28) to (3.30) have no azimuthal dependence. To construct a flowfield which includes a swirl velocity, equation (3.29) shows that at least one Monge variable must be a function of θ . To satisfy both of these constraints it is necessary to select:

$$D = \theta \quad (3.31)$$

$$\phi, A, B, C, E, F, G, H = f(r, z) \quad (3.32)$$

$$C(r, z) = rv_\theta \quad (3.33)$$

This results in a velocity field given by:

$$v_r = \frac{\partial \phi}{\partial r} + A \frac{\partial B}{\partial r} + E \frac{\partial F}{\partial r} + G \frac{\partial H}{\partial r} \quad (3.34)$$

$$v_\theta = v_\theta \quad (3.35)$$

$$v_z = \frac{\partial \phi}{\partial z} + A \frac{\partial B}{\partial z} + E \frac{\partial F}{\partial z} + G \frac{\partial H}{\partial z} \quad (3.36)$$

Here the axial and radial velocities are constructed from the axisymmetric Monge variables, shown in equation (3.32). The azimuthal velocity is constructed by dividing the axisymmetric Monge variable rv_θ by r .

Using equation (3.27), the material derivative of the velocity field can be written as:

$$\begin{aligned} \frac{D\vec{v}}{Dt} = & \nabla \left(\frac{D\phi}{Dt} - \frac{\vec{v} \cdot \vec{v}}{2} \right) + \frac{DA}{Dt} \nabla B + A \nabla \left(\frac{DB}{Dt} \right) + \frac{Drv_\theta}{Dt} \nabla \theta + \\ & rv_\theta \nabla \left(\frac{D\theta}{Dt} \right) + \frac{DE}{Dt} \nabla F + E \nabla \left(\frac{DF}{Dt} \right) + \frac{DG}{Dt} \nabla H + G \nabla \left(\frac{DH}{Dt} \right) \end{aligned} \quad (3.37)$$

By substituting this material derivative into the momentum equation (3.26), the following transport condition results:

$$\begin{aligned} \nabla \left(\frac{D\phi}{Dt} - \frac{\bar{v} \cdot \bar{v}}{2} \right) + \frac{DA}{Dt} \nabla B + A \nabla \left(\frac{DB}{Dt} \right) + \frac{Drv_\theta}{Dt} \nabla \theta + rv_\theta \nabla \left(\frac{D\theta}{Dt} \right) \\ + \frac{DE}{Dt} \nabla F + E \nabla \left(\frac{DF}{Dt} \right) + \frac{DG}{Dt} \nabla H + G \nabla \left(\frac{DH}{Dt} \right) = -\frac{\nabla P}{\rho} \end{aligned} \quad (3.38)$$

Yokota [1997] presents five possible solutions to a similar equation, the following can be called a modified Clebsch/Weber transformation:

$$\frac{D\phi}{Dt} = \frac{\bar{v} \cdot \bar{v}}{2} \quad (3.39)$$

$$A = rv_\theta \quad (3.40)$$

$$\frac{DB}{Dt} = -\frac{v_\theta}{r} \quad (3.41)$$

$$E = \frac{1}{\rho} \quad (3.42)$$

$$\frac{DF}{Dt} = -P \quad (3.43)$$

$$\frac{DG}{Dt} = 0 \quad (3.44)$$

$$\frac{DH}{Dt} = 0 \quad (3.45)$$

By considering continuity and the ‘ θ ’ component of the axisymmetric Euler equation it is clear that

$$\frac{D\left(\frac{1}{\rho}\right)}{Dt} = 0 \quad (3.46)$$

$$\frac{D(rv_\theta)}{Dt} = 0 \quad (3.47)$$

Also, to add an inflow shear to the problem it is necessary to select

$$G = v_z^* \quad (3.48)$$

$$H = Z \quad (3.49)$$

$$\phi = V_\infty z + \phi' \quad (3.50)$$

Where Z is a material coordinate in the z direction, v_z^* is an inflow shear, and V_∞ is the base axial flow. The only Monge variable that is not related to a physical parameter is B .

To gain an understanding of the B potential, a dimensional analysis was conducted on equation (3.41):

$$\frac{DB}{Dt} = -\frac{v_\theta}{r} \quad (3.51)$$

$$\frac{[\text{units}]}{[t]} = \frac{[1]}{[t]} \quad (3.52)$$

This simple analysis shows that B is dimensionless, it must represent a ratio or an angle. Squire's [1960] criterion for vortex breakdown stated that the value of the helix angle must exceed 50° upstream of a breakdown. Sarpkaya [1971a, 1971b, 1974] and Faler and Leibovich [1977a, 1977b] used a ratio of azimuthal to axial velocity as a non-dimensional parameter in their experimental investigations of vortex breakdown. The importance of this ratio of azimuthal to axial velocity in both Squire's analytical work, and the experimental studies of Sarpkaya and Faler and Leibovich is the justification for selecting the initial value of B , denoted as β , to be the helix angle.

$$\beta = \text{atan} \left(\frac{v_\theta}{v_z} \right) \quad (3.53)$$

Equation (3.53) is used to select boundary and initial conditions for equation (3.41). The evolution of B occurring after the initialization of the flow-field is not influenced by equation (3.53).

An axisymmetric flow with swirl is described by equations (3.39) to (3.45). To solve this system of equations, in particular equation (3.43), an additional constraint is required to obtain the pressure field. To avoid solving a pressure

equation, it is possible to use the incompressibility condition, equation (3.9), to solve for the Monge variable F .

In summary the equations to be solved are:

$$\bar{v} = \nabla (V_\infty z + \phi') + rv_\theta \nabla \theta + rv_\theta \nabla B + \frac{1}{\rho} \nabla F + v_z^s \nabla Z \quad (3.54)$$

$$\frac{D\phi'}{Dt} = \frac{\bar{v} \cdot \bar{v}}{2} - V_\infty v_z \quad (3.55)$$

$$\beta = \text{atan} \left(\frac{v_\theta}{v_z} \right) \quad (3.56)$$

$$\frac{DB}{Dt} = -\frac{v_\theta}{r} \quad (3.57)$$

$$\frac{D(rv_\theta)}{Dt} = 0 \quad (3.58)$$

$$\frac{D\rho}{Dt} = 0 \quad (3.59)$$

$$\frac{Dv_z^s}{Dt} = 0 \quad (3.60)$$

$$\frac{DZ}{Dt} = 0 \quad (3.61)$$

$$\nabla \cdot \bar{v} = 0 \quad (3.62)$$

This set of equations is solved by tailoring the numerical methods used to the physical properties of the equations. Equations (3.55) - (3.61) are hyperbolic and are solved using an upwind differencing scheme. Equation (3.62) is elliptic and will be solved using an approximate LU factorization with multigrid convergence acceleration [Yokota 1993].

3.4 Numerical Form of Convection Equations

The hyperbolic equations are written in conservative form to ensure that flow information is convected at the correct wavespeeds. The necessary manipula-

tions of these hyperbolic constraints are demonstrated on a model equation:

$$\frac{DT}{Dt} = S \quad (3.63)$$

Using (3.5), (3.63) can be written as:

$$\frac{\partial T}{\partial t} + v_r \frac{\partial T}{\partial r} + v_z \frac{\partial T}{\partial z} = S \quad (3.64)$$

Using the product rule of calculus and bringing the velocities into the derivatives results in:

$$\frac{\partial T}{\partial t} + \frac{\partial (v_r T)}{\partial r} + \frac{\partial (v_z T)}{\partial z} = S + T \left(\frac{\partial v_r}{\partial r} + \frac{\partial v_z}{\partial z} \right) \quad (3.65)$$

This technique, when applied to equations (3.55) to (3.61) results in the following set of equations:

$$\frac{\partial \phi'}{\partial t} + \frac{\partial (v_r \phi')}{\partial r} + \frac{\partial (v_z \phi')}{\partial z} = \frac{\bar{v} \cdot \bar{v}}{2} - V_\infty v_z + \phi' \left(\frac{\partial v_r}{\partial r} + \frac{\partial v_z}{\partial z} \right) \quad (3.66)$$

$$\frac{\partial B}{\partial t} + \frac{\partial (v_r B)}{\partial r} + \frac{\partial (v_z B)}{\partial z} = -\frac{v_\theta}{r} + B \left(\frac{\partial v_r}{\partial r} + \frac{\partial v_z}{\partial z} \right) \quad (3.67)$$

$$\frac{\partial r v_\theta}{\partial t} + \frac{\partial (v_r r v_\theta)}{\partial r} + \frac{\partial (v_z r v_\theta)}{\partial z} = +r v_\theta \left(\frac{\partial v_r}{\partial r} + \frac{\partial v_z}{\partial z} \right) \quad (3.68)$$

$$\frac{\partial v_z^s}{\partial t} + \frac{\partial (v_r v_z^s)}{\partial r} + \frac{\partial (v_z v_z^s)}{\partial z} = +v_z^s \left(\frac{\partial v_r}{\partial r} + \frac{\partial v_z}{\partial z} \right) \quad (3.69)$$

$$\frac{\partial Z}{\partial t} + \frac{\partial (v_r Z)}{\partial r} + \frac{\partial (v_z Z)}{\partial z} = +Z \left(\frac{\partial v_r}{\partial r} + \frac{\partial v_z}{\partial z} \right) \quad (3.70)$$

Solving the equations in this form would only be possible on a rectangular grid. To solve these equations for a wider range of geometries, it is necessary to write them in generalized co-ordinates.

3.5 Generalized Transformation

A two dimensional transformation of axisymmetric co-ordinates to generalized co-ordinates begins with the definition of a generalized system. For the present case this shall be defined as:

$$\xi = \xi(z, r) \quad (3.71)$$

$$\eta = \eta(z, r) \quad (3.72)$$

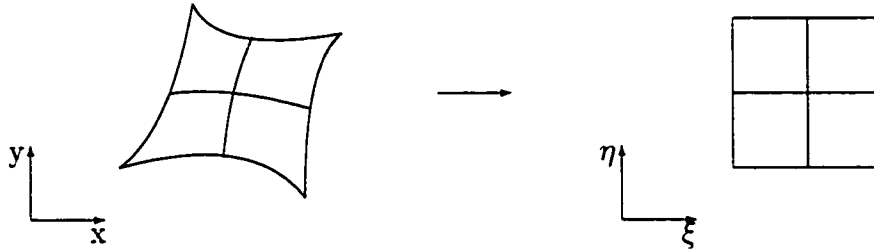


Figure 3.2: Schematic of Co-ordinate Transformation

With this definition and the chain rule of calculus it is possible to write the axisymmetric derivatives as:

$$\frac{\partial}{\partial z} = \frac{\partial \xi}{\partial z} \frac{\partial}{\partial \xi} + \frac{\partial \eta}{\partial z} \frac{\partial}{\partial \eta} \quad (3.73)$$

$$\frac{\partial}{\partial r} = \frac{\partial \xi}{\partial r} \frac{\partial}{\partial \xi} + \frac{\partial \eta}{\partial r} \frac{\partial}{\partial \eta} \quad (3.74)$$

The terms in (3.73) and (3.74) that involve the geometry of the grid are called metrics. To ensure that the transformed equations can be written in conservative form, the transformation needs to be expressed in terms of the inverse of these metrics. The inverse metrics can be derived using the definition of the transformation Jacobian:

$$J = \begin{pmatrix} \frac{\partial z}{\partial \xi} & \frac{\partial z}{\partial \eta} \\ \frac{\partial r}{\partial \xi} & \frac{\partial r}{\partial \eta} \end{pmatrix}$$

along with its inverse:

$$J^{-1} = \begin{pmatrix} \frac{\partial \xi}{\partial z} & \frac{\partial \xi}{\partial r} \\ \frac{\partial \eta}{\partial z} & \frac{\partial \eta}{\partial r} \end{pmatrix}$$

The inverse Jacobian can also be obtained from the Jacobian by utilizing Cramer's Rule from linear algebra to yield:

$$J^{-1} = \frac{1}{\|J\|} \begin{pmatrix} \frac{\partial r}{\partial \eta} & -\frac{\partial z}{\partial \eta} \\ -\frac{\partial r}{\partial \xi} & \frac{\partial z}{\partial \xi} \end{pmatrix}$$

where:

$$\|J\| = \frac{\partial z}{\partial \xi} \frac{\partial r}{\partial \eta} - \frac{\partial z}{\partial \eta} \frac{\partial r}{\partial \xi} \quad (3.75)$$

By matching the terms in these two alternate forms of the inverse Jacobian, the transformation equations (3.73) and (3.74) can be written as:

$$\frac{\partial}{\partial z} = \frac{1}{\|J\|} \left[\frac{\partial r}{\partial \eta} \frac{\partial}{\partial \xi} - \frac{\partial r}{\partial \xi} \frac{\partial}{\partial \eta} \right] \quad (3.76)$$

$$\frac{\partial}{\partial r} = \frac{1}{\|J\|} \left[\frac{\partial z}{\partial \xi} \frac{\partial}{\partial \eta} - \frac{\partial z}{\partial \eta} \frac{\partial}{\partial \xi} \right] \quad (3.77)$$

These transformation equations must be used on the hyperbolic convection equations as well as the elliptic continuity equation. The transformation shall be demonstrated on the model equation (3.65):

$$\frac{\partial T}{\partial t} + \frac{\partial (v_r T)}{\partial r} + \frac{\partial (v_z T)}{\partial z} = S + T \left(\frac{\partial v_r}{\partial r} + \frac{\partial v_z}{\partial z} \right) \quad (3.78)$$

When the spatial derivatives are replaced with the transformation equations (3.76) and (3.77) we obtain:

$$\begin{aligned} \frac{\partial}{\partial t} (T\|J\|) + \frac{\partial}{\partial \eta} (Tv_r z_\xi - Tv_z r_\xi) + \frac{\partial}{\partial \xi} (Tv_z r_\eta - Tv_r z_\eta) = \|J\|S \\ + T \left(\frac{\partial}{\partial \eta} (v_r z_\xi - v_z r_\xi) + \frac{\partial}{\partial \xi} (v_z r_\eta - v_r z_\eta) \right) \end{aligned} \quad (3.79)$$

where advantage has been taken of the Geometric Conservation Laws:

$$\frac{\partial^2 z}{\partial \xi \partial \eta} = \frac{\partial^2 z}{\partial \eta \partial \xi} \quad (3.80)$$

$$\frac{\partial^2 r}{\partial \xi \partial \eta} = \frac{\partial^2 r}{\partial \eta \partial \xi} \quad (3.81)$$

Defining transformed velocities as

$$\begin{bmatrix} U_\xi \\ U_\eta \end{bmatrix} = J^{-1} \begin{pmatrix} v_z \\ v_r \end{pmatrix}$$

the transformed model equation can be written as

$$\frac{\partial}{\partial t} (T\|J\|) + \frac{\partial}{\partial \eta} (T\|J\|U_\eta) + \frac{\partial}{\partial \xi} (T\|J\|U_\xi) = \|J\|S + T \left(\frac{\partial}{\partial \eta} (\|J\|U_\eta) + \frac{\partial}{\partial \xi} (\|J\|U_\xi) \right) \quad (3.82)$$

Given this model equation, the actual kinematic conditions to be solved are:

$$\frac{\partial}{\partial t} (\phi'\|J\|) + \frac{\partial}{\partial \eta} (\phi'\|J\|U_\eta) + \frac{\partial}{\partial \xi} (\phi'\|J\|U_\xi) = \|J\| \left(\frac{\bar{v} \cdot \bar{v}}{2} - V_\infty v_z \right) + \phi' \psi \quad (3.83)$$

$$\frac{\partial}{\partial t} (B\|J\|) + \frac{\partial}{\partial \eta} (B\|J\|U_\eta) + \frac{\partial}{\partial \xi} (B\|J\|U_\xi) = -\|J\| \frac{v_\theta}{r} + B\psi \quad (3.84)$$

$$\frac{\partial}{\partial t} (rv_\theta\|J\|) + \frac{\partial}{\partial \eta} (rv_\theta\|J\|U_\eta) + \frac{\partial}{\partial \xi} (rv_\theta\|J\|U_\xi) = rv_\theta\psi \quad (3.85)$$

$$\frac{\partial}{\partial t} (v_z^s\|J\|) + \frac{\partial}{\partial \eta} (v_z^s\|J\|U_\eta) + \frac{\partial}{\partial \xi} (v_z^s\|J\|U_\xi) = v_z^s\psi \quad (3.86)$$

$$\frac{\partial}{\partial t} (Z\|J\|) + \frac{\partial}{\partial \eta} (Z\|J\|U_\eta) + \frac{\partial}{\partial \xi} (Z\|J\|U_\xi) = Z\psi \quad (3.87)$$

where:

$$\psi = \left(\frac{\partial}{\partial \eta} (\|J\|U_\eta) + \frac{\partial}{\partial \xi} (\|J\|U_\xi) \right) \quad (3.88)$$

This set of equations is solved using a midpoint rule time integration in conjunction with a uniformly second order accurate non-oscillatory interpolation scheme (UNO2).

3.6 Dimensional Analysis

The final modification made to the governing equations is to put them into dimensionless form. Dimensionless variables are defined as:

$$r^* = \frac{r}{R}, \quad z^* = \frac{z}{R}, \quad v_r^* = \frac{v_r}{V_{ref}}, \quad v_z^* = \frac{v_z}{V_{ref}}, \quad t^* = \frac{tV_{ref}}{R} \quad (3.89)$$

$$\phi^* = \frac{\phi}{RV_{ref}}, \quad \rho^* = \frac{\rho}{\rho_{ref}}, \quad F^* = \frac{F}{\rho_{ref}RV_{ref}}, \quad v_\theta^* = \frac{v_\theta}{V_{ref}} \quad (3.90)$$

$$B^* = B, \quad v_z^{s*} = \frac{v_z^s}{V_{ref}}, \quad Z^* = \frac{Z}{R} \quad (3.91)$$

The radial and axial velocity fields are given by:

$$v_r = \frac{\partial \phi}{\partial r} + rv_\theta \frac{\partial B}{\partial r} + \frac{1}{\rho} \frac{\partial F}{\partial r} + v_z^s \frac{\partial Z}{\partial r} \quad (3.92)$$

$$v_z = V_\infty + \frac{\partial \phi}{\partial z} + rv_\theta \frac{\partial B}{\partial z} + \frac{1}{\rho} \frac{\partial F}{\partial z} + v_z^s \frac{\partial Z}{\partial z} \quad (3.93)$$

Substituting the non-dimensional variables, we obtain:

$$v_r^* = \frac{\partial \phi^*}{\partial r^*} + r^* v_\theta^* \frac{\partial B^*}{\partial r^*} + \frac{1}{\rho^*} \frac{\partial F^*}{\partial r^*} + v_z^{s*} \frac{\partial Z^*}{\partial r^*} \quad (3.94)$$

$$v_z^* = \frac{V_\infty}{V_{ref}} + \frac{\partial \phi^*}{\partial z^*} + r^* v_\theta^* \frac{\partial B^*}{\partial z^*} + \frac{1}{\rho^*} \frac{\partial F^*}{\partial z^*} + v_z^{s*} \frac{\partial Z^*}{\partial z^*} \quad (3.95)$$

It is clear that the velocity decomposition is in non-dimensional form without the introduction of any non-dimensional parameters.

The continuity equation can be written as:

$$\frac{\partial}{\partial r}(rv_r) + \frac{\partial}{\partial z}(rv_z) = 0 \quad (3.96)$$

Substituting the dimensionless variables results in:

$$\frac{\partial}{\partial r^*}(r^*v_r^*) + \frac{\partial}{\partial z^*}(r^*v_z^*) = 0 \quad (3.97)$$

The continuity equation is in non-dimensional form without the introduction of any non-dimensional numbers.

Using the non-dimensional variables, the model convection equation, equation (3.63), can be written as:

$$\frac{\partial T^*}{\partial t^*} + v_r^* \frac{\partial T^*}{\partial r^*} + v_z^* \frac{\partial T^*}{\partial z^*} = S^* \quad (3.98)$$

The convection equations are also non-dimensional without the introduction of any non-dimensional parameters. The * will be dropped in all future equations, where it is assumed that the variables are non-dimensional.

CHAPTER 4

NUMERICAL TECHNIQUES

4.1 Solution Sequence

A benefit of employing a Clebsch decomposition to the Euler equations is that the resulting system of equations can be solved by coupling the numerical methods to the physical characteristics of the equations. The hyperbolic wave equations are solved using a Leapfrog Method, and the elliptic continuity equation is solved using an approximately factored LU scheme whose growth factor is tailored to the use of multigrid.

The sequence in which these hyperbolic and elliptic equations is solved is important, and shall be outlined here:

1. Initial conditions on all of the complex lamellar potentials except for the F potential are specified. The F potential is calculated by solving the continuity equation (4.1). This equation is solved using an approximately factored LU scheme and accelerated to a steady state by the multigrid method.
2. The complex lamellar variable equations (3.83) to (3.87) are character-

istically convected to the next time level using a leapfrog method and a uniformly second order accurate interpolation scheme (UNO2). The boundary conditions are then updated at this new time level.

3. An F potential that satisfies the continuity equation is obtained at the new time level.

4.2 Elliptic Equations

Elliptic equations have imaginary characteristics. Information in these acoustic equations is not transmitted in any preferred directions, instead it is propagated in all directions simultaneously. Thus, it is beneficial to solve elliptic equations with a numerical scheme that gathers information from all directions. The continuity equation is solved at each timestep by using an approximately factored LU scheme which is accelerated to convergence by a geometric multigrid solver [Yokota 1987].

4.2.1 Approximate LU Factorization

Substituting the velocity decomposition (3.27) into equation (3.96), the following expression is obtained:

$$\begin{aligned} & \frac{\partial}{\partial r} \left[(r) \left(\frac{\partial \phi'}{\partial r} + r v_\theta \frac{\partial B}{\partial r} + \frac{1}{\rho} \frac{\partial F}{\partial r} + v_z^s \frac{\partial Z}{\partial r} \right) \right] \\ & + \frac{\partial}{\partial z} \left[(r) \left(V_\infty + \frac{\partial \phi'}{\partial z} + r v_\theta \frac{\partial B}{\partial z} + \frac{1}{\rho} \frac{\partial F}{\partial z} + v_z^s \frac{\partial Z}{\partial z} \right) \right] = 0 \end{aligned} \quad (4.1)$$

The F potential is constructed to satisfy the continuity equation. This is achieved numerically by first making equation (4.1) time dependent and then

iterating the resulting equation to a steady state. Rearranging (4.1) gives:

$$\begin{aligned} \frac{\partial F}{\partial t^*} = & \frac{\partial}{\partial r} \left(\frac{r}{\rho} \frac{\partial F}{\partial r} \right) + \frac{\partial}{\partial z} \left(\frac{r}{\rho} \frac{\partial F}{\partial z} \right) + \\ & \frac{\partial}{\partial r} \left[(r) \left(\frac{\partial \phi'}{\partial r} + r v_\theta \frac{\partial B}{\partial r} + v_z^s \frac{\partial Z}{\partial r} \right) \right] + \frac{\partial}{\partial z} \left[(r) \left(V_\infty + \frac{\partial \phi'}{\partial z} + r v_\theta \frac{\partial B}{\partial z} + v_z^s \frac{\partial Z}{\partial z} \right) \right] \end{aligned} \quad (4.2)$$

where t^* is a pseudo time different from the real time t .

Equation (4.2) is solved using an approximately factored LU scheme. This scheme is derived by considering a Taylor series expansion of the F potential:

$$F^{k+1} = F^k + \frac{\partial F^k}{\partial t^*} \Delta t^* + O(\Delta t^{*2}) \quad (4.3)$$

This can also be written as:

$$F^{k+1} = F^k + \Delta t^* \left[(1 - \mu) \frac{\partial F^k}{\partial t^*} + \mu \frac{\partial F^k}{\partial t^*} \right] + O(\Delta t^{*2}) \quad (4.4)$$

Using equation (4.3) we obtain:

$$F^{k+1} = F^k + \Delta t^* \left[(1 - \mu) \frac{\partial F^k}{\partial t^*} + \mu \frac{\partial F^{k+1}}{\partial t^*} \right] + O(\Delta t^{*2}) \quad (4.5)$$

By defining $\Delta F = F^{k+1} - F^k$, and rearranging we are left with:

$$\Delta F - \mu \Delta t^* \left[\frac{\partial F^{k+1}}{\partial t^*} - \frac{\partial F^k}{\partial t^*} \right] = \Delta t^* \frac{\partial F^k}{\partial t^*} \quad (4.6)$$

The time derivative on the right hand side of equation (4.6) can be replaced using equation (4.2). For brevity the right hand side of equation (4.2) shall be labelled as the residual, Res:

$$\Delta F - \mu \Delta t^* \left[\frac{\partial F^{k+1}}{\partial t^*} - \frac{\partial F^k}{\partial t^*} \right] = \Delta t^* \text{Res}^k \quad (4.7)$$

Linearizing equation (4.7) about the last time step gives:

$$\left\{ I - \mu \Delta t^* \left[\frac{\partial}{\partial r} \left(\frac{r}{\rho} \frac{\partial}{\partial r} \right) + \frac{\partial}{\partial z} \left(\frac{r}{\rho} \frac{\partial}{\partial z} \right) \right] \right\} \Delta F^k = \Delta t^* \text{Res}^k \quad (4.8)$$

This is written in delta form as:

$$\left\{ I - \mu \Delta t^* \left[\delta_r \frac{r}{\rho} \delta_r + \delta_z \frac{r}{\rho} \delta_z \right] \right\} \Delta F^k = \Delta t^* \text{Res}^k \quad (4.9)$$

Equation (4.9) can be written as an approximate factorization:

$$\begin{aligned} & \left[I - \mu \Delta t^* \left(\left(\frac{r}{\rho} \right)_{i+1/2} \frac{\delta_z^+}{\Delta z^2} + \left(\frac{r}{\rho} \right)_{j+1/2} \frac{\delta_r^+}{\Delta r^2} \right) \right] \\ & \left[I + \mu \Delta t^* \left(\left(\frac{r}{\rho} \right)_{i-1/2} \frac{\delta_z^-}{\Delta z^2} + \left(\frac{r}{\rho} \right)_{j-1/2} \frac{\delta_r^-}{\Delta r^2} \right) \right] \Delta F^k = \omega \Delta t^* \text{Res}^k \end{aligned} \quad (4.10)$$

where ω is a relaxation factor. This is solved in two steps:

$$\begin{aligned} (1) \quad & \left[I + \mu \Delta t^* \left(\left(\frac{r}{\rho} \right)_{i-1/2} \frac{\delta_z^-}{\Delta z^2} + \left(\frac{r}{\rho} \right)_{j-1/2} \frac{\delta_r^-}{\Delta r^2} \right) \right] \Delta F' = \omega \Delta t^* \text{Res} \\ (2) \quad & \left[I - \mu \Delta t^* \left(\left(\frac{r}{\rho} \right)_{i+1/2} \frac{\delta_z^+}{\Delta z^2} + \left(\frac{r}{\rho} \right)_{j+1/2} \frac{\delta_r^+}{\Delta r^2} \right) \right] \Delta F = \Delta F' \end{aligned} \quad (4.11)$$

Steps (1) and (2) in equation (4.11) are solved explicitly in a step by step manner.

As with the hyperbolic equations, the continuity equation is solved in generalized co-ordinates to allow for flexibility in the types of grids which may be used. The transformation is carried out using the techniques described in Section 3.5, and results in:

$$\begin{aligned} (1) \quad & \left[I + \mu \Delta t^* \left(\left(\frac{K_2 r}{\rho} \right)_{i-1/2} \delta_\xi^- + \left(\frac{K_1 r}{\rho} \right)_{j-1/2} \delta_\eta^- \right) \right] \Delta F' = \omega \Delta t^* \text{Res} \\ (2) \quad & \left[I - \mu \Delta t^* \left(\left(\frac{K_2 r}{\rho} \right)_{i+1/2} \delta_\xi^+ + \left(\frac{K_1 r}{\rho} \right)_{j+1/2} \delta_\eta^+ \right) \right] \Delta F = \Delta F' \end{aligned} \quad (4.12)$$

where:

$$\text{Res} = \frac{\partial}{\partial \eta} (r \|J\| U_\eta) + \frac{\partial}{\partial \xi} (r \|J\| U_\xi) \quad (4.13)$$

$$K_1 = \frac{z_\xi^2 + r_\xi^2}{\|J\|} \quad (4.14)$$

$$K_2 = \frac{z_\eta^2 + r_\eta^2}{\|J\|} \quad (4.15)$$

4.2.2 Calculation of the Residual

The residual as written in equation (4.13) can be recast in a more general form as:

$$\text{Res} = \frac{\partial}{\partial \eta} (A_f) + \frac{\partial}{\partial \xi} (B_f) \quad (4.16)$$

where A_f and B_f are representative fluxes.

In this work all spatial derivatives are solved for using a finite volume approximation. In this approximation, the differential in the η direction represents the change of the A_f flux in the η direction. The ξ differential represents the change in the B_f flux in the ξ direction. The η differential is approximated by differencing the values of A_f on the top and bottom faces of a computational cell and dividing by $\Delta\eta = 1$. Similarly the ξ differential is obtained by differencing the values of B_f on the right and left hand faces of a computational cell and dividing by $\Delta\xi = 1$. The residual can be written as the sum of these differences:

$$\text{Res}_{i,j} = (A_{f_{i,j+1/2}} - A_{f_{i,j-1/2}}) + (B_{f_{i+1/2,j}} - B_{f_{i-1/2,j}}) \quad (4.17)$$

The values of the fluxes at the cell faces is obtained from the cell centered data through a linear interpolation.

4.2.3 Stability Analysis Of LU Scheme

A numerical scheme is said to be stable if the numerical error remains bounded as:

1. $t \rightarrow \infty$ for a fixed Δt
2. $\Delta t \rightarrow 0$ for a fixed t

This analysis of stability is carried out using a von Neumann Stability Analysis. This technique is applied to a simplified model equation. The model equation is simpler to analyze than the full equation, but offers insight into the stability characteristics of the full equation. This analysis is only a guideline as it provides a necessary but not sufficient condition for stability. For this analysis, equation (4.1) is approximated by:

$$\frac{\partial^2 F}{\partial z^2} = 0 \quad (4.18)$$

The approximate LU factorization of equation (4.18) is:

$$\left[I + \mu\alpha\delta_z^- \right] \cdot \left[I - \mu\alpha\delta_z^+ \right] \Delta F_j = \alpha\omega\delta_{zz}F_j \quad (4.19)$$

where $\alpha = \frac{\Delta t^*}{\Delta z^2}$ is the Fourier Number and ω is a relaxation parameter.

A Fourier decomposition of the solution potential F is:

$$F_j = G^k e^{i\beta_w z} \quad (4.20)$$

where G^k represents the growth factor or, the ratio of the numerical solution between two consecutive time steps.

$$G^k = \frac{F_j^{k+1}}{F_j^k} \quad (4.21)$$

In operator form, the LU scheme can be written as:

$$LU\Delta F^k = \text{Res}F^k \quad (4.22)$$

Using equation (4.20) L, U and Res can be written:

$$L = [I + \mu\alpha (1 - e^{-i\beta_w})] \quad (4.23)$$

$$U = [I - \mu\alpha (e^{i\beta_w} - 1)] \quad (4.24)$$

$$\text{Res} = \alpha\omega [e^{i\beta_w} + e^{-i\beta_w}] \quad (4.25)$$

Equation (4.22) can be rearranged into the form:

$$F^{k+1} = (LU)^{-1} (\text{Res} + LU) F^k \quad (4.26)$$

By comparing equation (4.26) and equation (4.21), it is clear that:

$$G^k = (LU)^{-1} (\text{Res} + LU) \quad (4.27)$$

Substituting equations (4.23) to (4.25) into equation (4.27) and using the general mathematical results:

$$\cos(z) = \frac{1}{2} (e^{iz} + e^{-iz}) \quad (4.28)$$

$$\sin^2\left(\frac{z}{2}\right) = \frac{1}{2} (1 - \cos(z)) \quad (4.29)$$

The growth factor of the approximately factored LU scheme can be written as:

$$G = \frac{1 - 4\alpha [\omega - \mu(1 + \mu\alpha)] \sin^2(\beta_w \Delta z/2)}{1 + 4\mu\alpha(1 + \mu\alpha) \sin^2(\beta_w \Delta z/2)} \quad (4.30)$$

The growth factor is shown in Figure 4.1, for the parameter values $\mu = 0.5$, $\alpha = 5.3$, and $\omega = 1.9$. These values were chosen to optimize the schemes ability to damp high frequency errors.

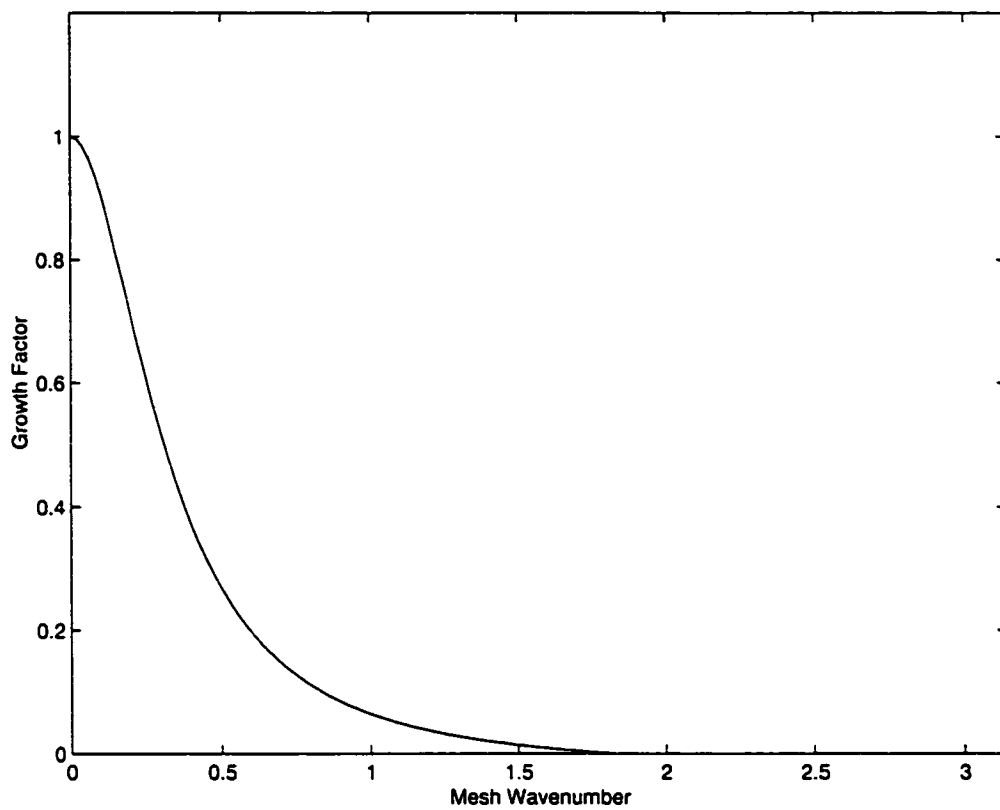


Figure 4.1: Growth Factor of LU Scheme

4.2.4 Multigrid Convergence Acceleration

Figure 4.1 demonstrates the fact that the approximately factored LU scheme has favorable high wavenumber damping. As with most numerical schemes, both explicit and implicit, it is the low frequency errors that cause slow asymptotic convergence to steady state [Yokota 1987].

The Multigrid method is founded on the principle that low frequency errors on a fine grid are high frequency errors on a courser mesh. By solving the flow equations on course meshes and updating the fine grid solution including a course grid influence, convergence rates can be dramatically improved. The accuracy of the solution is governed by the fine grid calculation, the course grids help to accelerate the solution to a steady state.

The solution of steady state problems is governed by the boundary conditions. It can be said that Multigrid accelerates the solution by accelerating the influence of these boundary conditions.

In operator form, the LU scheme can be written as:

$$LU\Delta F = -\Delta t \text{Res} \quad (4.31)$$

Initially the scheme is applied to the fine grid, allowing an updated fine grid solution to be calculated:

$$LU_h\Delta F_h = -\Delta t \text{Res}_h \quad (4.32)$$

$$F_h^{k+1} = F_h^k + \Delta F_h^k \quad (4.33)$$

The fine grid residual contains low frequency errors which are more efficiently removed on the course grids. The fine grid residual is transferred to the courser grids using a direct summation denoted by \tilde{N}_{h-1}^h :

$$\text{Res}_{h-1}^c = \tilde{N}_{h-1}^h \text{Res}_h \quad (4.34)$$

The fine grid solution is transferred to the courser meshes using an area weighted averaging process denoted by N_{h-1}^h :

$$F_{h-1}^t = N_{h-1}^h F_h \quad (4.35)$$

Using the transferred course grid solution, a course grid residual is now calculated:

$$\begin{aligned} \text{Res}_{h-1}^t &= \text{Res} [F_{h-1}^t]_{h-1} \\ &= \text{Res} [N_{h-1}^h F_h]_{h-1} \end{aligned} \quad (4.36)$$

A forcing function FF , is calculated from the residuals in equations (4.36) and (4.34). The forcing function is a measure of the difference in truncation error between the two grids.

$$\begin{aligned} FF &= \text{Res}_{h-1}^c - \text{Res}_{h-1}^t \\ &= \tilde{N}_{h-1}^h F_h - \text{Res} [N_{h-1}^h F_h]_{h-1} \end{aligned} \quad (4.37)$$

The course grid residual is the sum of the forcing function and the residual calculated on the course grid:

$$\begin{aligned} LU_{h-1} \Delta F_{h-1} &= -\Delta t (\text{Res}_{h-1} + FF_{h-1}) \\ &= -\Delta t \left(\text{Res}_{h-1} + N_{h-1}^h \text{Res}_h - \text{Res} (N_{h-1}^h F_h)_{h-1} \right) \end{aligned} \quad (4.38)$$

This procedure of passing grid information down to progressively courser grids continues until the coarsest grid has been reached. At this point, course grid corrections are passed up to progressively finer grids until the fine grid is reached.

The corrections are interpolated in the following manner:

$$\begin{aligned} F_h' &= F_h + I_h^{h-1} (F_{h-1}' - F_{h-1}^t) \\ &= F_h + I_h^{h-1} (F_{h-1}' - N_{h-1}^h F_h) \end{aligned} \quad (4.39)$$

where:

$$F'_{h-1} = F_{h-1} + I_{h-1}^{h-2} (F'_{h-2} - N_{h-2}^{h-1} F_{h-1}) \quad (4.40)$$

The Multigrid procedure is continued until the desired level of accuracy has been reached.

The I and N operators denote interpolation and transfer operations used to pass information up and down between different grid levels. They are not the inverse of one another.

There are many different forms that a Multigrid cycle can take [Yokota 1987]. In this work, a five level W cycle is used.

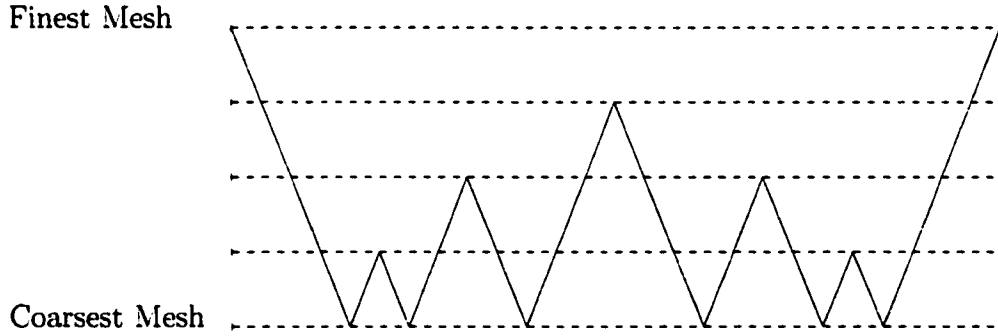


Figure 4.2: Five Level Multigrid Scheme

4.3 Hyperbolic Equations

Hyperbolic equations have two real characteristics, or lines along which information is propagated. This means that these equations have both a domain of dependence and a region of influence and that the equation propagates

information in the direction of the flow. This physical behavior has an important impact on the numerical scheme used to solve hyperbolic equations. Central differencing is not a valid choice of discretization since this method assumes that the independent variable at a point is affected by every point around it. This obviously violates the concept of a domain of dependence. Instead an upwinding scheme must be used to solve hyperbolic equations. Often, upwinding is associated with one sided differencing. For a one dimensional problem this is true, but for a multi-dimensional problem there is an infinite number of directions and waves which may be chosen to upwind. For such multi-dimensional problems, a more sophisticated technique must be applied to achieve upwinding. In this work a leapfrog method in conjunction with a nonoscillatory quadratic interpolation scheme (UNO2) is applied to upwind all the hyperbolic equations.

For the model convection equation (3.82) with no source term, the finite volume formulation of the leapfrog method may be written as:

$$T_{i,j}^{n+1} = T_{i,j}^n - \frac{\Delta t}{\|J\|} \left[\frac{M_{i+1/2,j}^{n+1/2} - M_{i-1/2,j}^{n+1/2}}{\Delta \xi} + \frac{K_{i,j+1/2}^{n+1/2} - K_{i,j-1/2}^{n+1/2}}{\Delta \eta} \right] \quad (4.41)$$

where $M = U_\xi \|J\| T$, $K = U_\eta \|J\| T$ and $\Delta \xi = 1$, $\Delta \eta = 1$.

The half cell information used to calculate the convective derivatives is obtained using UNO2 a uniformly non-oscillatory second order accurate interpolation technique derived by Harten and Osher [1987]. The following description is from Yokota [1998].

4.3.1 UNO2 Convection Scheme

A one dimensional interpolation can be written as:

$$T = T_i + S_i^z (z - z_i) \quad (4.42)$$

where the repeated indices do not imply summation. S_i^z represents the slope of T in the 'z' direction, and for Harten and Oshers UNO2 scheme [1987] is given by:

$$S_i^z = \frac{\text{Median} \left(0, T_{i+1/2}^c - T_i, T_i - T_{i-1/2}^c \right)}{\Delta z / 2} \quad (4.43)$$

A quadratic interpolation is used to construct the $T_{i+1/2}^c$ terms:

$$T_{i+1/2}^c = \frac{1}{2} (T_i + T_{i+1}) - \frac{1}{4} D_{i+1/2} \quad (4.44)$$

where:

$$D_{i+1/2} = \text{minmod} (T_{i+1} - 2T_i + T_{i-1}, T_{i+2} - 2T_{i+1} + T_i) \quad (4.45)$$

and:

$$\text{minmod} (a, b) = \text{sign} (a) \max (0, \text{sign} (ab) \min (|a|, |b|)) \quad (4.46)$$

Following characteristics back to their spatial locations at time level n allows for the calculation of cell face data at time level $n + 1/2$. Surface data at the half cells can be calculated in four different ways depending upon the axial and radial convection speeds. For positive convection speeds, the half cell surface data is given by:

$$T_{i+1/2,j}^{n+1/2} = T_{i,j}^n + S_{i,j}^z \frac{\Delta z}{2} \left(1 - \frac{v_{z(i+1/2,j)} \Delta t}{\Delta z} \right) - S_{i,j}^r \frac{v_{r(i+1/2,j)} \Delta t}{2} \quad (4.47)$$

After the cell face data has been updated, the cell centered values are updated using the Leapfrog method, equation (4.41)

4.3.2 Source Terms

The discretized convection equation (4.41) does not include the source term found in equation (3.82). The numerical inclusion of the source term is quite straightforward. Numerically, the convective derivatives found in equation (3.82) are treated as residuals, which, when added to time level n , update the solution to time level $n + 1$:

$$T_{i,j}^{n+1} = T_{i,j}^n + \text{Res} \quad (4.48)$$

The source term is calculated at time level n in accordance with equation (4.17), and added to the residual prior to updating the solution.

4.4 Boundary and Initial Conditions

When using a complex lamellar velocity decomposition, the specification of boundary and initial conditions is not a trivial matter. The specified conditions on all of the Monge variables must be chosen to satisfy certain physical boundary conditions while introducing no numerical instabilities into the various governing equations.

4.4.1 Solid Wall and Symmetry Boundary Conditions

Equation (3.54) is the kinematic velocity decomposition of the velocity field:

$$\bar{v} = \nabla (V_\infty z + \phi') + rv_\theta \nabla \theta + rv_\theta \nabla B + \frac{1}{\rho} \nabla F + v_z^s \nabla Z$$

Along the top solid wall boundary and along the symmetry boundary, the physical condition that must be met in an inviscid flow is a no flux condition.

In transformed co-ordinates the radial velocity can be written as:

$$v_r = \frac{1}{D} [z_\xi A_2 - z_\eta A_1] \quad (4.49)$$

where:

$$\begin{aligned} A_1 &= \frac{\partial \phi'}{\partial \xi} + r v_\theta \frac{\partial B}{\partial \xi} + \frac{1}{\rho} \frac{\partial F}{\partial \xi} + v_z^s \frac{\partial Z}{\partial \xi} \\ A_2 &= \frac{\partial \phi'}{\partial \eta} + r v_\theta \frac{\partial B}{\partial \eta} + \frac{1}{\rho} \frac{\partial F}{\partial \eta} + v_z^s \frac{\partial Z}{\partial \eta} \end{aligned} \quad (4.50)$$

Since all of the grids used in this study use only vertical grid lines in the radial direction, the term $z_\eta = 0$. This reduces equation (4.49) to:

$$v_r = \frac{1}{D} [z_\xi A_2] \quad (4.51)$$

This will be identically zero at the wall and symmetry boundaries when the following conditions are set:

$$\left. \frac{\partial \phi'}{\partial \eta} \right|_{wall} = 0, \quad \left. \frac{\partial B}{\partial \eta} \right|_{wall} = 0, \quad \left. \frac{\partial F}{\partial \eta} \right|_{wall} = 0, \quad \left. \frac{\partial Z}{\partial \eta} \right|_{wall} = 0 \quad (4.52)$$

$$\left. \frac{\partial \phi'}{\partial \eta} \right|_{sym} = 0, \quad \left. \frac{\partial B}{\partial \eta} \right|_{sym} = 0, \quad \left. \frac{\partial F}{\partial \eta} \right|_{sym} = 0, \quad \left. \frac{\partial Z}{\partial \eta} \right|_{sym} = 0 \quad (4.53)$$

4.4.2 Inflow Boundary Conditions

In an incompressible flow, downstream disturbances can influence the upstream flow through pressure waves. For these incompressible calculations, the inflow boundary condition is specified such that it can adjust to downstream disturbances. This is achieved by specifying the axial velocity to be C^1 continuous over the inflow boundary:

$$\frac{\partial v_z}{\partial z} = 0 \quad (4.54)$$

This condition allows the inflow to adjust to both radial and axial disturbances. An F potential is constructed along the inflow boundary such that equation (4.54) is satisfied.

The remaining Monge variables are chosen such that an inflow axial velocity distribution can be prescribed. In transformed co-ordinates, the axial velocity can be written as:

$$v_z = \frac{1}{D} [r_\eta A_1 - r_\xi A_2] \quad (4.55)$$

where A_1 and A_2 are given in equation (4.50). Since $r_\xi = 0$ along the inflow boundary for all of the grids used in this study, the axial velocity expression reduces to:

$$v_z = \frac{1}{D} r_\eta \left[V_\infty + \frac{\partial \phi'}{\partial \xi} + r v_\theta \frac{\partial B}{\partial \xi} + \frac{1}{\rho} \frac{\partial F}{\partial \xi} + v_z^s \frac{\partial Z}{\partial \xi} \right] \quad (4.56)$$

By setting:

$$\left. \frac{\partial \phi'}{\partial \xi} \right|_{inflow} = 0, \quad \left. \frac{\partial B}{\partial \xi} \right|_{inflow} = 0, \quad \left. \frac{\partial Z}{\partial \xi} \right|_{inflow} = 1 \quad (4.57)$$

we are left with

$$v_z = \frac{1}{D} r_\eta \left[V_\infty + v_z^s + \frac{1}{\rho} \frac{\partial F}{\partial \xi} \right] \quad (4.58)$$

for the axial velocity.

To obtain a value for the F potential from equation (4.54) would require:

$$\frac{\partial^2 F}{\partial \xi^2} = 0 \quad (4.59)$$

be specified along the inlet boundary. This boundary condition cannot be used with equation (4.12). A second order partial differential equation cannot have a second order boundary condition. Using the continuity equation (3.96), an equivalent boundary condition for equation (4.54) is:

$$\frac{\partial (r v_r)}{\partial r} = 0 \quad (4.60)$$

When expanded utilizing the equation for v_r with $z_\eta = 0$, this becomes:

$$\frac{\partial}{\partial \eta} \left(\frac{r}{\rho} \frac{\partial F}{\partial \eta} \right) = - \left[r \frac{\partial^2 \phi}{\partial \eta^2} + \frac{\partial}{\partial \eta} \left(r^2 v_\theta \frac{\partial B}{\partial \eta} \right) + \frac{\partial}{\partial \eta} \left(r v_z^s \frac{\partial Z}{\partial \eta} \right) \right] \quad (4.61)$$

Discretizing this equation gives:

$$F_{j+1} \left(\frac{r}{\rho} \right)_{j+1/2} - F_j \left[\left(\frac{r}{\rho} \right)_{j+1/2} + \left(\frac{r}{\rho} \right)_{j-1/2} \right] + F_{j-1} \left(\frac{r}{\rho} \right)_{j-1/2} = -\text{Res}_j \quad (4.62)$$

where the residual is the right hand side of equation (4.61). This tridiagonal system is solved for the inflow F potential using the Thomas algorithm.

The boundary condition on the inflow shear is supplied explicitly to the code, as is the density and reduced circulation (rv_θ). In the simulations conducted in this research the following conditions were applied:

$$v_z^s = 0 \quad (4.63)$$

$$V_\infty = 1 \quad (4.64)$$

$$rv_\theta = V_{\theta 1} (1 - \exp(-\alpha r^2)) \quad (4.65)$$

$$\rho = 1.0 \quad (4.66)$$

Equation (4.65) is known as a Burgers vortex [Rusak et. al. 1998]. $V_{\theta 1}$ is the swirl level and is used to control the magnitude of the swirl velocity. α is used to control the size of the vortical core:

$$\frac{r_c}{r_t} = \frac{1.12}{\alpha^{\frac{1}{2}}} \quad (4.67)$$

Figure 4.3(a) illustrates the inflow distribution of the reduced circulation (rv_θ) with a swirl level of $V_{\theta 1} = 0.5$ and a vortical core of $r_c = 0.6$. Figure 4.3(b) is the corresponding inflow distribution of azimuthal velocity.

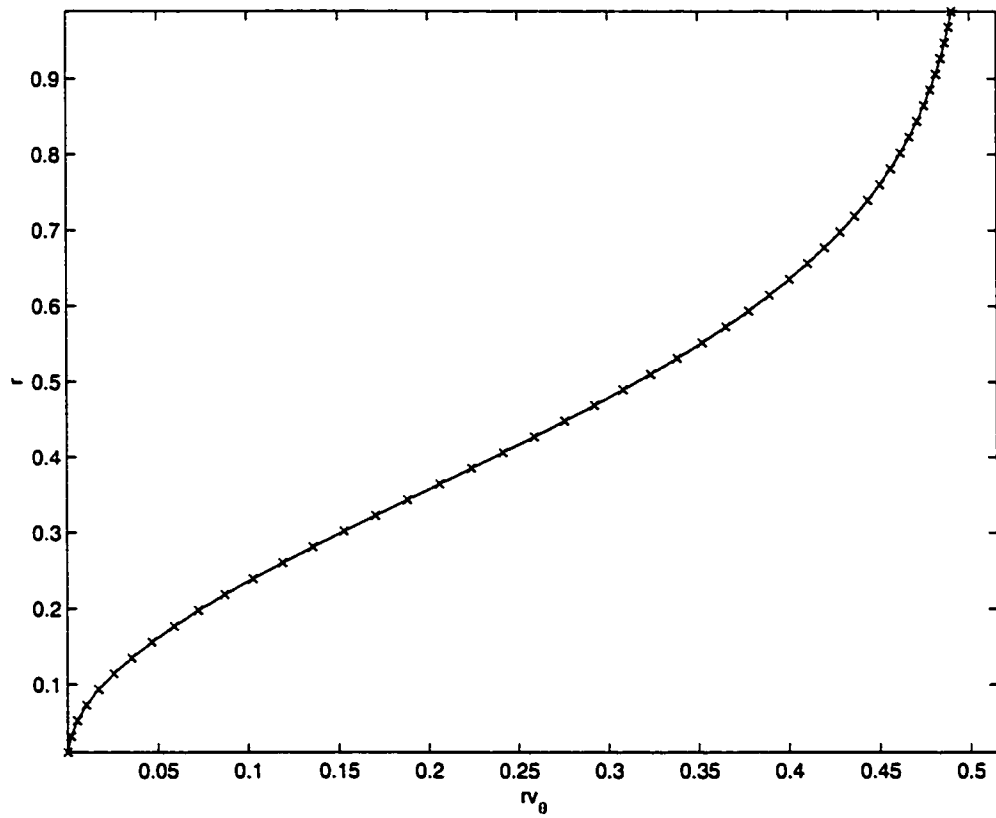


Figure 4.3(a): Inflow Distribution of Reduced Circulation ($V_{\theta 1} = 0.5$)

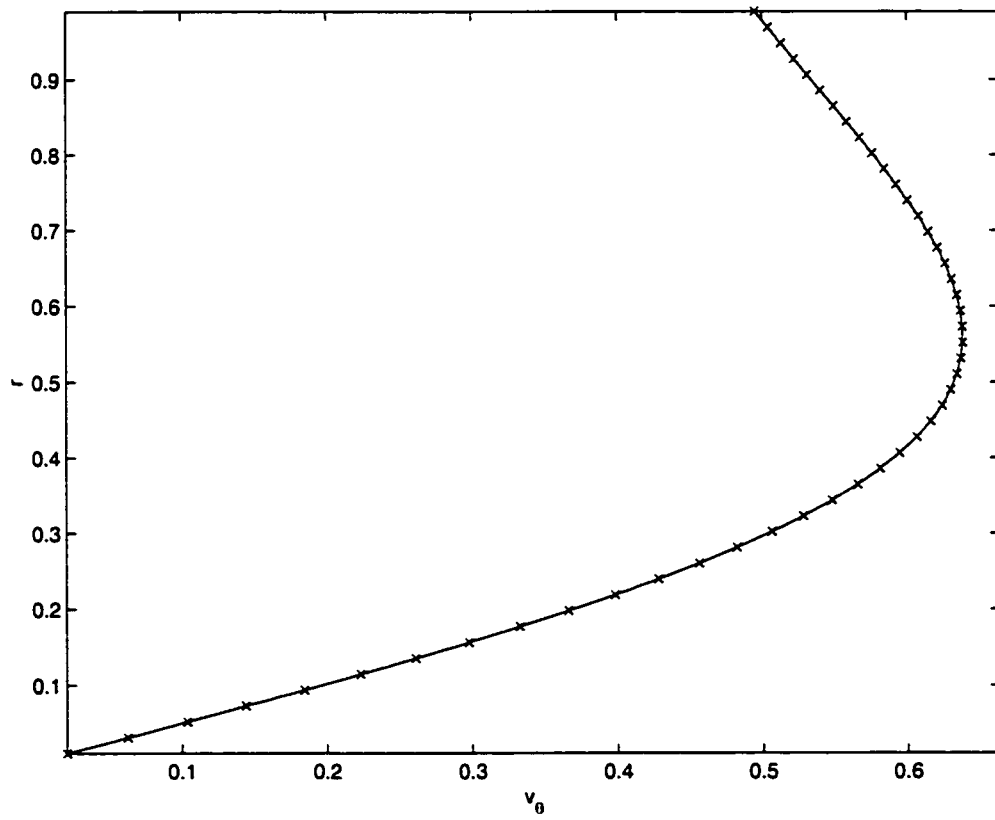


Figure 4.3(b): Inflow Distribution of Azimuthal Velocity ($V_{\theta 1} = 0.5$)

4.4.3 Outflow Boundary Condition

The outflow boundary condition must be chosen so that the flow can move smoothly through the outlet. This is achieved on the convected variables by setting:

$$\left. \frac{\partial^2 \phi'}{\partial \xi^2} \right|_{outflow} = 0, \quad \left. \frac{\partial^2 B}{\partial \xi^2} \right|_{outflow} = 0, \quad \left. \frac{\partial^2 Z}{\partial \xi^2} \right|_{outflow} = 0 \quad (4.68)$$

$$\left. \frac{\partial^2 \rho}{\partial \xi^2} \right|_{outflow} = 0, \quad \left. \frac{\partial^2 v_z}{\partial \xi^2} \right|_{outflow} = 0, \quad \left. \frac{\partial^2 (rv_\theta)}{\partial \xi^2} \right|_{outflow} = 0 \quad (4.69)$$

Since the equation for F , equation (4.11), is a second order partial differential equation, it is impossible to use the boundary condition:

$$\frac{\partial^2 F}{\partial \xi^2} = 0 \quad (4.70)$$

as this would not constitute a well posed mathematical problem. It is possible, however, to enforce this condition indirectly. The outflow boundary condition on F is similar to that utilized for the inflow boundary. Equation (4.54) is satisfied along the outflow boundary by solving equation (4.60) for the F potential. Equation (4.60) is discretized to equation (4.62) and solved using the Thomas algorithm.

4.4.4 Initial Conditions

The initial conditions on the convected variables are input to the code, and the initial condition on the F variable is constructed from these values by solving the continuity equation.

The initial conditions on the convected quantities are:

$$v_z^s = 0 \quad (4.71)$$

$$V_\infty = 1 \quad (4.72)$$

$$rv_\theta = V_{\theta 1} (1 - \exp(-\alpha r^2)) \quad (4.73)$$

$$\beta = \text{atan}\left(\frac{v_\theta}{v_z^s + V_\infty}\right) \quad (4.74)$$

$$\phi = 0 \quad (4.75)$$

$$\rho = 1 \quad (4.76)$$

$$Z = z \quad (4.77)$$

B is initialized to the local inflow helix angle β . Figure 4.4 shows the inflow helix angle β for a Burgers vortex with $V_{\theta 1} = 0.5$ and $r_c = 0.6$. The initial condition for the reduced circulation is identical to its inflow boundary condition shown in Figure 4.3(a).

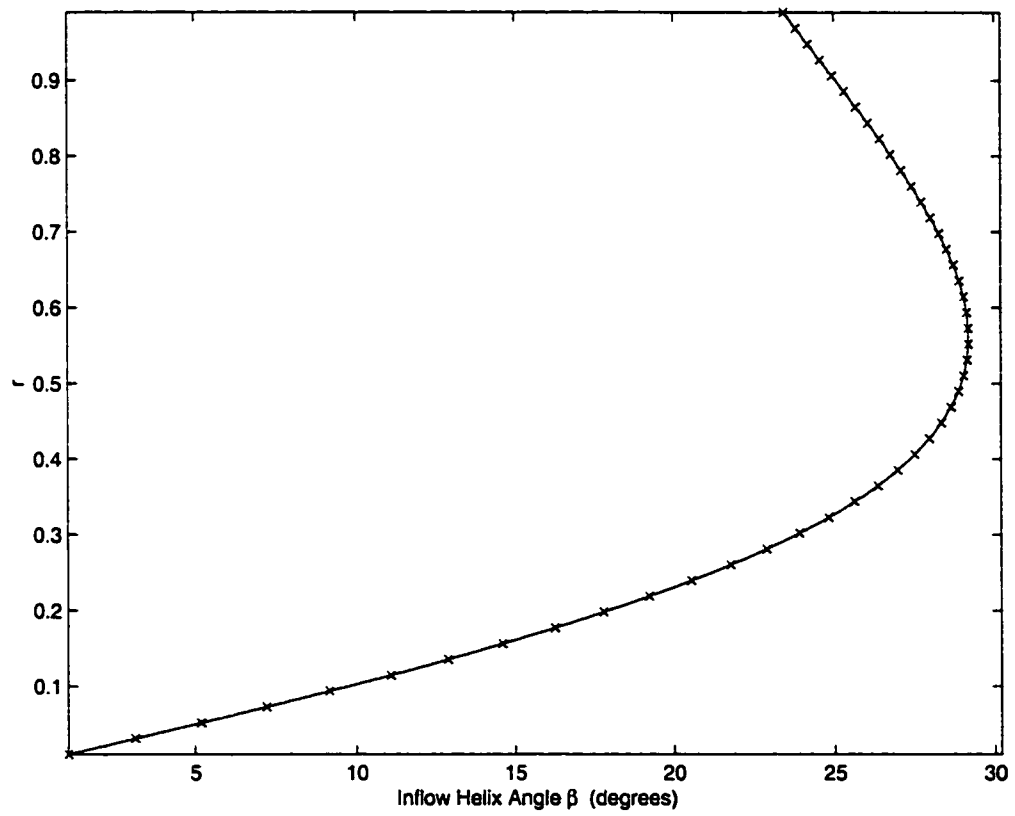


Figure 4.4: Initial Condition on Beta Potential ($V_{\theta 1} = 0.5$)

CHAPTER 5

RESULTS

5.1 Flow Through a Straight Pipe

Simulations of flow in a straight pipe were conducted to test the code's fidelity. In the absence of spatial and temporal disturbances, swirling and non-swirling inviscid flows should convect through straight pipes with no change.

Figure 5.1 shows the grid used for straight pipe flow calculations. The grid corresponds to the flow plane shown in Figure 3.1. In the axial direction the grid is 8 units long and discretized by 128 uniformly sized computational cells ($\Delta z = 0.0625$). In the radial direction the grid is 1 unit high and is discretized by 48 uniformly spaced computational cells ($\Delta r = 0.0208$). Simulations were conducted using finer grids with no change in the flow solution, indicating that the solutions are not grid dependent.

A timestep of 0.01 was used in these calculations. Since this timestep corresponds to a maximum local Courant number of 0.16, we are confident that these simulations are numerically stable. Each timestep, the maximum

residual in the continuity equation is reduced to $O(10^{-14})$ within 6 iterations using a 5 level multigrid cycle, Figure 4.2



Figure 5.1: Straight Pipe Numerical Domain

5.1.1 Non-Swirling Flow

Material lines in the z direction are Lagrangian co-ordinates. Although the initial conditions are assumed to exist for $-\infty < z < +\infty$, they are only observed within the finite domain shown in Figure 5.2(a). In Figure 5.2(a) the material co-ordinates coincide with the Eulerian co-ordinates. Equation (3.61) governs the evolution of the Z material lines and indicates that these lines are purely convected with the flow. Figure 5.2(b) shows the Lagrangian co-ordinates after 3200 timesteps. At this instant in time the initial flow has convected 32 pipe radii or 4 times through the numerical domain. Since the material lines are still straight and parallel after 3200 timesteps, it is clear that the flow is still uniform.

5.1.2 Swirling Flow

Figure 5.2(a) also represents the initial condition for the Z material lines in a swirling flow. The inflow helix angle β is described by equations (4.74),(4.72) and (4.65) with $V_{\theta 1} = 0.6$, and is shown in Figure 5.3(a). The inflow helix angle is used as the initial condition of the B potential. Equation (3.41) governs the evolution of B indicating that this is not a purely convected quantity. A B distribution exists for $-\infty < z < +\infty$, but is only observed within the finite flow domain.

By examining a simplified swirling flow, the significance of the B term becomes clear. This simplified flow is axisymmetric and the velocity field is given by:

$$v_z = 1 \tag{5.1}$$

$$v_r = 0 \quad (5.2)$$

$$v_\theta = \zeta r \quad (5.3)$$

Substituting this velocity field into equation (3.41) gives:

$$\frac{\partial B}{\partial t} = -\zeta \quad (5.4)$$

Integrating gives:

$$B_2 = B_1 - \zeta t \quad (5.5)$$

This simplified analysis shows that for a uniform flow in solid body rotation, B is a linear function of time. The Burgers vortex employed in this work contains a core region of solid body swirling flow and this region should behave similarly to equation (5.5). B will only develop a nonuniform distribution in regions where the local helix angle β is a function of 'z', the radial velocity is non-zero or the azimuthal velocity is not solid body rotation. B offers a unique three dimensional insight into axisymmetric swirling flows. All of the other convected quantities in this work are convected by the axial and radial velocity field, they feel no influence of the swirling component. B is also convected by the axial and radial velocities, but it is also influenced by the azimuthal velocity through the source term in equation (3.41). This quantity, which is unique to the potential\complex lamellar decomposition, is axisymmetric yet influenced by the three dimensional velocity field.

Figures 5.3(b) and 5.3(c) show the Z material lines and B potential after 3200 timesteps or after passing 4 times through the computational domain. The convected Z material lines have remained vertical indicating that no

shear disturbances have developed in the flow. The B distribution has remained independent of ' z ', indicating that no azimuthal or axial velocity shears have developed.

The inlet boundary condition applied to the F potential, equation (4.61), does not fix the inflow axial velocity for all time. Instead, this boundary condition satisfies the continuity equation and allows the axial velocity to adjust to any downstream disturbance. The literature categorizes breakdown flows by the localized velocity ratio along the inlet, or inflow helix angle (β). Therefore, it is important to quantify the variation with time of the the local helix angle in these flow simulations. Figure 5.3(d) shows that β is constant for all time in a straight pipe flow.

Text resumes on page 79

Increment = 1
 Maximum Value = 7
 Minimum Value = 1

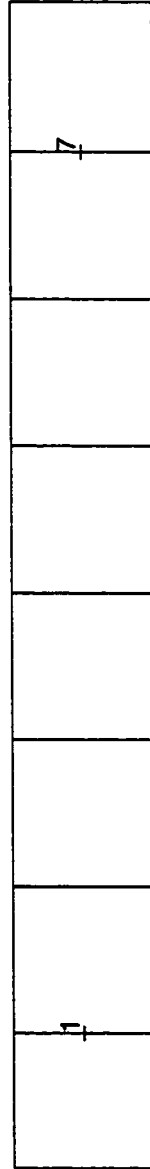


Figure 5.2(a): Initial Condition of Z Material Lines ($V_{01} = 0.0$)

Increment = 1
 Maximum Value = -25
 Minimum Value = -31



Figure 5.2(b): Z Material Lines After 3200 timesteps ($V_{\theta 1} = 0.0$)

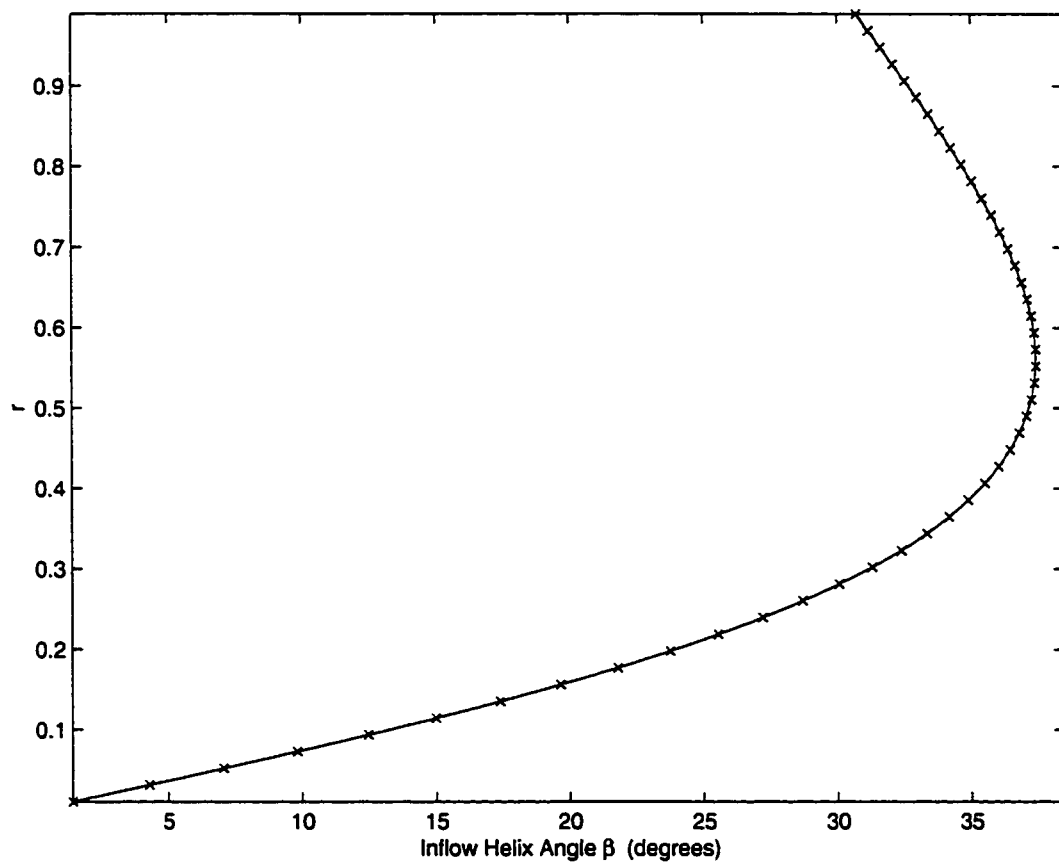


Figure 5.3(a): Inflow Helix Angle β ($V_{\theta 1} = 0.6$)

Increment = 1
 Maximum Value = -25
 Minimum Value = -31



Figure 5.3(b): Z Material Lines After 3200 timesteps ($V_{\theta 1} = 0.6$)

Increment = 6
 Maximum Value = -20
 Minimum Value = -80

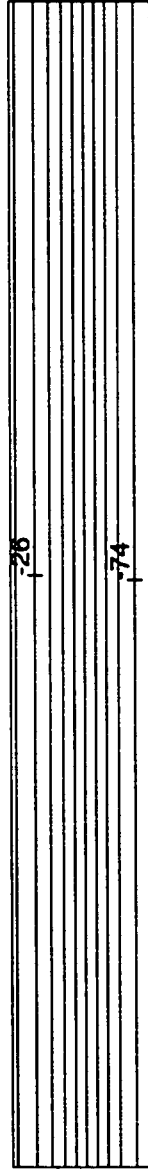


Figure 5.3(c): *B* Potential After 3200 timesteps ($V_{01} = 0.6$)

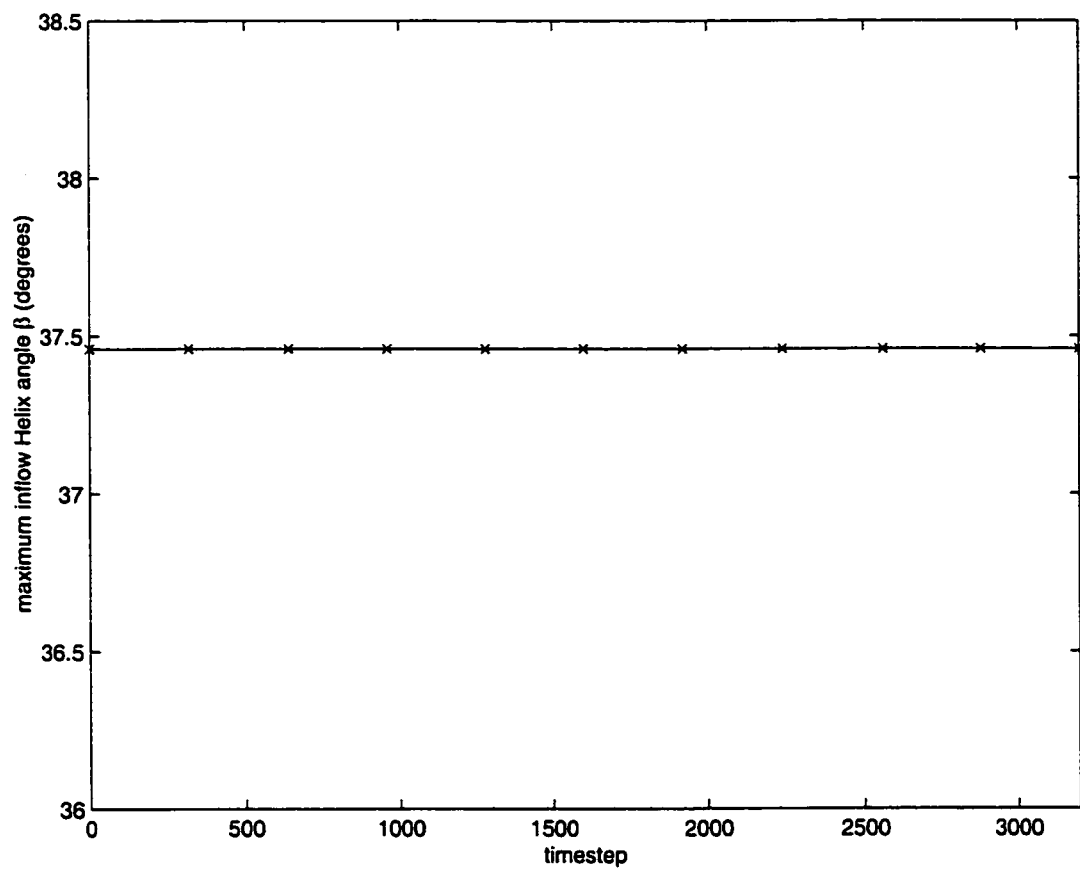


Figure 5.3(d): Temporal Variation of Inflow Helix Angle (β) ($V_{\theta 1} = 0.6$)

5.2 Flow Through a Divergent Pipe

Figure 5.4 shows the grid used to study vortex breakdown flows. The grid corresponds to the flow plane shown in Figure 3.1. In the axial direction the grid is 8 units long and is discretized by 128 uniformly sized computational cells ($\Delta z = 0.0625$). The section of the grid from $z = 0$ to $z = 2$ is 1 unit high and is discretized by 32 cells in the axial direction and 48 cells in the radial direction ($\Delta r = 0.0208$). The divergent portion of the grid extends from $z = 2$ to $z = 8$ and has a 2° angle of divergence. This portion of the grid is discretized by 96 cells in the axial direction and 48 cells in the radial direction. The radial grid spacing in the divergent section of the grid varies in the axial direction from $\Delta r = 0.0208$ at $z = 2$ to $\Delta r = 0.0252$ at $z = 8$. The distribution of the computational cells was chosen so that the coarsest mesh used in multigrid consisted of a straight pipe discretization of 2 cells x 3 cells and a divergent section discretization of 6 cells x 3 cells. This ensured that the grid maintained its shape in the multigrid calculations. The solutions obtained are not grid dependent as simulations conducted on finer grids produced the same results.

Diverging pipes have been used in experimental studies of vortex breakdown [Sarpkaya 1971a 1971b 1974, Faler & Leibovich 1977a 1977b, Bruecker and Althaus 1995]. It was found that the radial velocities generated in diverging pipes promoted the occurrence of a breakdown by initiating the tilting of the axial vorticity into azimuthal vorticity which is characteristic of breakdown flows [Darmofal 1993]. Computational work has also been carried out in diverging tubes [Darmofal 1996, Beran and Culick 1992]. In numerical work, the wave propagation characteristics found in a diverging tube isolate the

breakdown location from the inlet of the numerical domain. The importance of isolating a vortex breakdown from the inflow boundary is emphasized by Spall et. al. [1987], and in the discussion of Section 2.3. Since the inflow boundary condition of this work, equation (4.57), is influenced by the flow-field it is of paramount importance that the breakdown occurs at least one pipe radius downstream of the inflow boundary. If the breakdown structure were able to influence the inlet boundary, an unsteady boundary condition would exist. This would make it impossible to attribute the flow development to fluid dynamic effects as opposed to numerically induced effects.

A timestep of 0.01 was used in all divergent pipe calculations. Since this timestep corresponds to a local maximum Courant number of 0.18, we are again confident that these simulations are numerically stable. At each timestep, the maximum residual in the continuity equation is reduced to $O(10^{-9})$ within 8 iterations using a 5 level multigrid cycle, Figure 4.2.

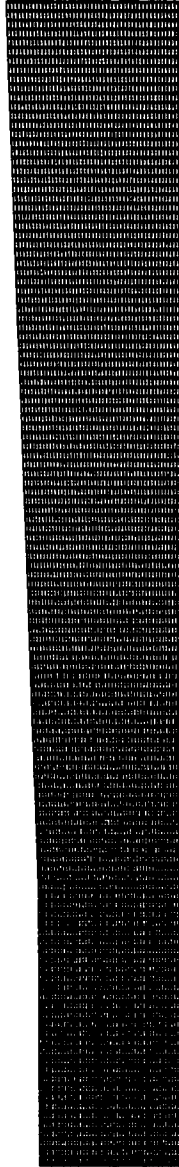


Figure 5.4: Diverging Pipe Numerical Domain

5.2.1 Non-Swirling Flow

Panton [1996] presents an analytical solution for inviscid, irrotational plane flow through a diverging duct. The geometry considered by this solution consists of a straight pipe followed by a diffuser and another section of straight pipe. The straight pipe sections are considered to be of infinite extent, and a solution is obtained through a Schwarz-Christoffel transformation. It is not possible to make quantitative comparisons between the present simulations and Panton's work due to the infinite flow domain he considers, and due to two singular points that occur in his solution. However, it is possible to make qualitative comparisons of the overall flow behavior.

Panton predicts an infinite velocity occurring at the point on the wall where the first straight pipe connects to the diffuser. Through the Bernoulli equation, this infinite velocity results in a low pressure occurring at this point. In an inviscid flow, a pressure gradient is required to turn streamlines, the large velocity is created so that the streamlines can curve into the diffuser section. Panton predicts that the velocity along the wall at the connecting point of the diffuser and second straight pipe should be zero. The low velocity creates a high pressure at this point and the corresponding pressure gradient bends the streamlines into the outflow pipe.

Figure 5.5(a) is the initial axial velocity field for a non-swirling flow through a diverging pipe. Figure 5.5(b) is the axial velocity after 3200 timesteps. It is clear from Figure 5.5(b), that the axial velocity reaches a maximum along the wall at the entrance of the divergent section. This local maximum agrees qualitatively with the infinite velocity found in Panton's analytical solution, and exists to bend the streamlines into the diffuser. The

F potential is shown in Figure 5.5(c). F is calculated to satisfy continuity, however the kinematic condition governing F , equation (3.43), shows it to be closely related to the pressure field. The gradients in the F potential in the straight pipe section are causing the flow to accelerate towards the bent. In the divergent section, the F gradients are causing flow deceleration. These observations are in agreement with Panton's analytical solution.

Figure 5.5(d) and Figure 5.5(e) represent material lines in the 'z' direction initially and after 3200 timesteps. The fact that these timelines are still vertical after the flow has convected through the computational domain 4 times, indicates that there are no shear disturbances being generated by the pipe divergence.

Text resumes on page 89

Increment = 0.025
 Maximum Value = 1.1
 Minimum Value = 0.85



Figure 5.5(a): Initial Condition of Axial Velocity ($V_{\theta 1} = 0.0$)

Increment = 0.03
 Maximum Value = 1.1
 Minimum Value = 0.8

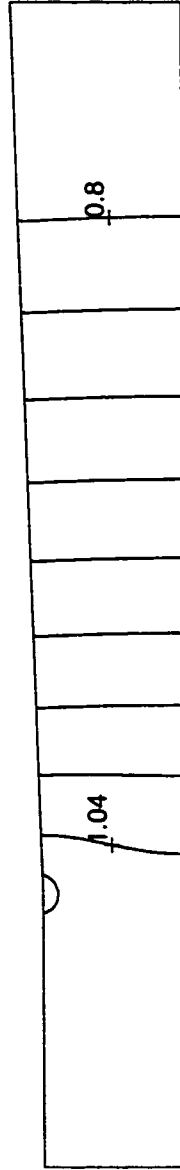


Figure 5.5(b): Axial Velocity After 3200 timesteps ($V_{\theta 1} = 0.0$)

Increment = 0.02
 Maximum Value = 1.2
 Minimum Value = 1

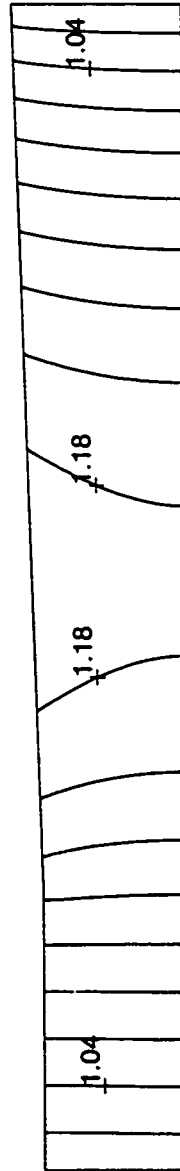


Figure 5.5(c): F Potential 3200 timesteps ($V_{\theta 1} = 0.0$)

Increment = 1
 Maximum Value = 7
 Minimum Value = 1

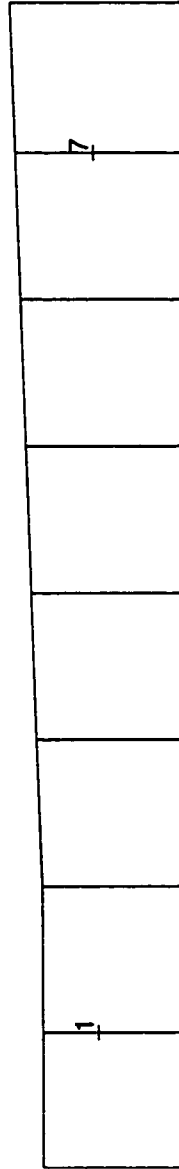


Figure 5.5(d): Initial Condition on Z Material Lines ($V_{\theta 1} = 0.0$)

Increment = 1
 Maximum Value = -26
 Minimum Value = -33

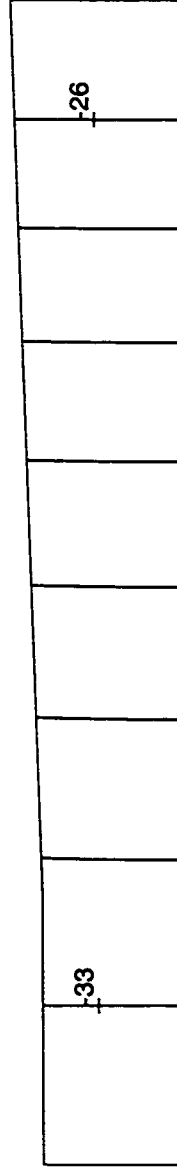


Figure 5.5(e): Z Material Lines after 3200 timesteps ($V_{01} = 0.0$)

5.2.2 Pre-Breakdown Swirling Flow

Batchelor [1967] presents analytical solutions of inviscid axisymmetric swirling flows. The analysis of these flows was completed using the Bragg-Hawthorne equation with the additional assumption of quasi-cylindrical stream surfaces. The Bragg-Hawthorne equation requires the specification of a circulation function and a total head function at a location upstream of the inflow condition. The form of these functions will not be valid in regions of reversed flow since the fluid originating downstream of the outlet does not necessarily have the same form as the flow at the inlet. For this reason, Batchelor's analysis is only valid up to the formation of a stagnation point.

Batchelor analyzed a Rankine vortex in a uniform flow. He assumed that at a location downstream of the initial conditions the velocity at the edge of the vortical core had decelerated to half of its upstream value. This boundary condition mimics the effect a divergent pipe section would have on the flow. Batchelor found that with this velocity deceleration along the outside of the vortical core, the axial velocity along the pipe centerline would stagnate when the quantity $\frac{2\Omega r_c}{V_{z1}}$ was of order unity. When Batchelor's swirl ratio was less than unity, flow deceleration but not stagnation was predicted along the vortex centerline.

Figure 5.6(a) shows the initial axial velocity distribution for a swirling flow in the divergent pipe. The inflow helix angle β is shown in Figure 5.6(b) for $V_{\theta1} = 0.4$. The velocity field after 3200 timesteps is given in Figure 5.6(c). This plot shows that the axial velocity along the pipe centerline has decreased to about 60% of the inlet axial velocity, but has not stagnated. The deceleration of the flow along the pipe axis is clearly illustrated by

the shearing of the Z material lines in the diffuser section of Figure 5.6(d). Figure 5.6(e), the B potential after 3200 timesteps, shows that the flow in the straight pipe has remained uniform. The flow in the bottom 25% of the diffuser is not uniform, indicating that a shear has developed. Figure 5.6(f) shows the F potential for this field, Figure 5.6(g) is a more detailed contour plot of the region inside the vortical core. The strongest axial gradients in the F potential are found in the region of highest material line shearing. This indicates that the strongest axial pressure gradients exist in this region. All breakdown flows undergo their most drastic flow changes along the pipe centerline, and the behavior along the axis of symmetry can be used to characterize the flow behavior as a whole [Beran and Culick 1992]. Figure 5.6(h) shows the variation of the minimum axial velocity along the pipe centerline with time. It is clear that the axial velocity is asymptoting to a steady state axial velocity 1800 timesteps.

Figure 5.6(i) shows the variation of the inflow helix angle β with time. The initial conditions applied in this work are not exact solutions for the flow through a diverging duct. The initial conditions are washed out of the flow domain after 800 timesteps, and this period is represented by the first 3 data points in Figure 5.6(i). After the initial transients have been washed out of the flow domain, the helix angle is asymptoting a steady state.

A quantitative comparison of this simulation and Batchelor's [1967] work is only approximate, due to differences in swirl velocity distribution and pipe geometry. The axial velocity along the edge of the vortical core in Figure 5.6(c) is reduced to 80% of the inflow value and Batchelor only considered the case where this velocity reduction was 50%. In a general sense, Batchelor

showed that by reducing the axial velocity along the edge of the vortex core, the velocity along the pipe centerline reduces by a greater amount. This behavior is evident in Figure 5.6(c). The velocity along the vortex core is reduced to 80% of the upstream value and the velocity along the axis of symmetry is reduced to 60% of the inflow value. The quantity $\frac{2\Omega r_c}{V_{z1}}$ is approximately unity for the flow shown in Figure 5.6(c). The present results and the results of Batchelor exhibit similar behavior and are of the same order of magnitude and significance.

Text resumes on page 101

Increment = 0.025
 Maximum Value = 1.1
 Minimum Value = 0.85

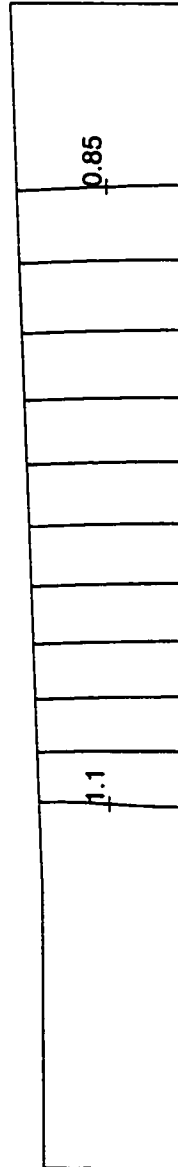


Figure 5.6(a): Initial Condition of Axial Velocity ($V_{\theta 1} = 0.4$)

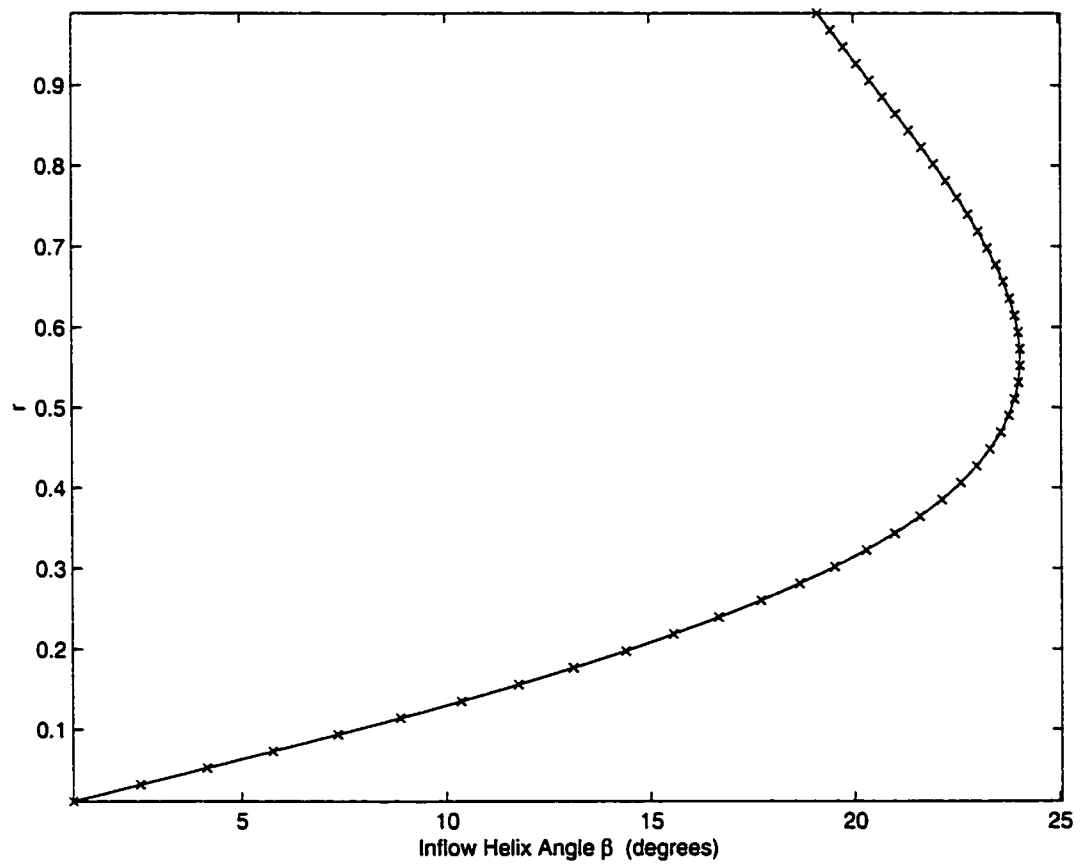


Figure 5.6(b): Inflow Helix Angle β ($V_{\theta 1} = 0.4$)

Increment = 0.05
 Maximum Value = 1.1
 Minimum Value = 0.6



Figure 5.6(c): Axial Velocity After 3200 timesteps ($V_{\theta 1} = 0.4$)

Increment = 1
 Maximum Value = -25
 Minimum Value = -34



Figure 5.6(d): Z Material Lines after 3200 timesteps ($V_{01} = 0.4$)

Increment = 4
 Maximum Value = -12
 Minimum Value = -48

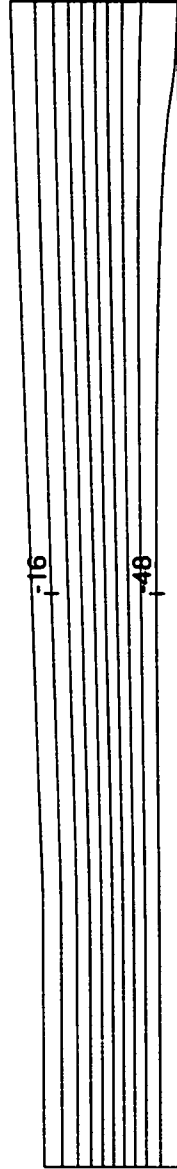


Figure 5.6(e): *B* Potential After 3200 timesteps ($V_{\theta 1} = 0.4$)

Increment = 1
 Maximum Value = 13
 Minimum Value = 1

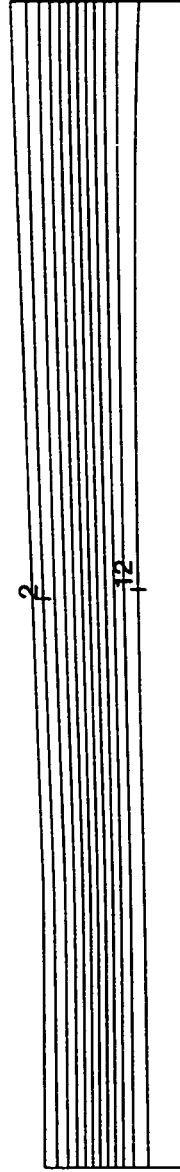


Figure 5.6(f): F Potential After 3200 timesteps ($V_{\theta 1} = 0.4$)

Increment = 0.2
 Maximum Value = 13
 Minimum Value = 11

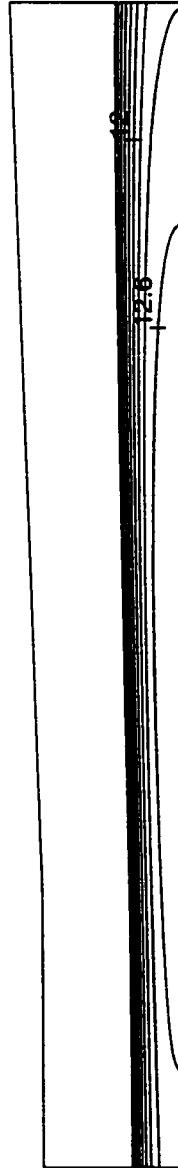


Figure 5.6(g): Detailed F Potential After 3200 timesteps ($V_{\theta_1} = 0.4$)

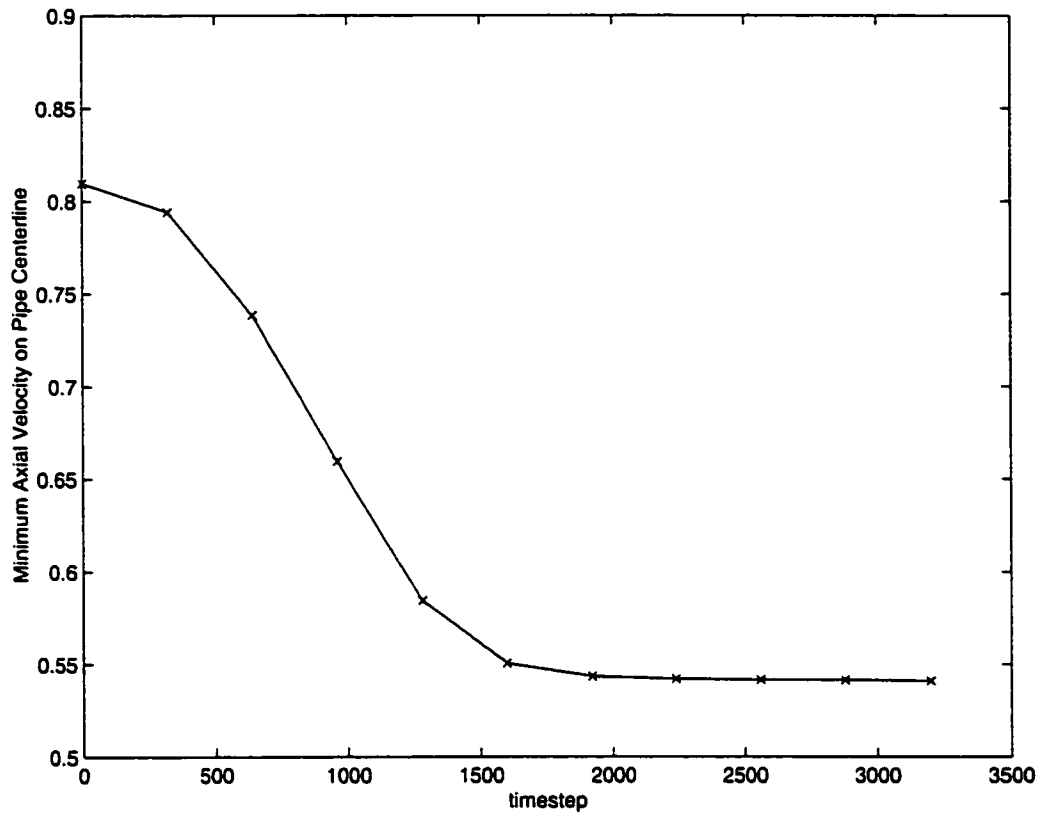


Figure 5.6(h): Convergence of Minimum Axial Velocity ($V_{\theta 1} = 0.4$)

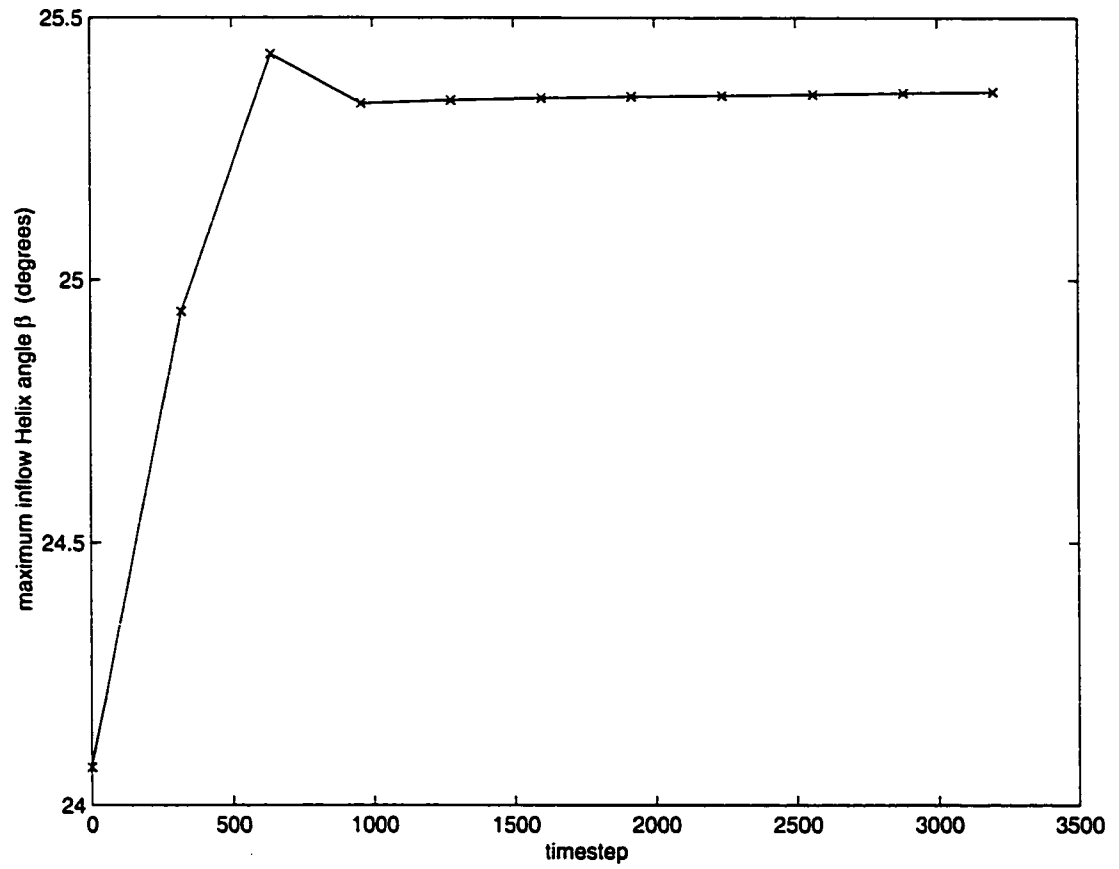


Figure 5.6(i): Temporal Variation of Inflow Helix Angle β ($V_{\theta 1} = 0.4$)

5.2.3 Incipient Breakdown Swirling Flow

Buntine and Saffman [1995] conducted numerical simulations of vortex breakdown in diverging pipes using the Bragg-Hawthorne equation. These simulations are only valid up to the occurrence of a stagnation point on the pipe axis due to the inherent limitations of the Bragg-Hawthorne equation discussed in the previous section. For pipes of a unit length and an inlet to outlet radius ratio of 1.5, Buntine and Saffman studied the response of a Burger vortex to changes in the swirl velocity magnitude. For a uniform inflow axial velocity, Buntine and Saffman observed that the level of flow deceleration along the axis decreases monotonically with an increase in swirl velocity until a stagnation point is reached.

Figure 5.7(a) shows the axial velocity field after convecting 4 times through the computational domain (3200 timesteps) with a swirl level of $V_{\theta 1} = 0.45$ and inflow helix angle β distribution shown in Figure 5.7(b). The only difference in the flow conditions leading to Figure 5.6(c) and Figure 5.7(a) is the applied β level. The minimum axial velocity in Figure 5.7(a) is 20% lower than that in Figure 5.6(c). The additional flow deceleration caused by increasing the swirl level is clearly illustrated by the Z material co-ordinates. The shearing of the Z material lines in Figure 5.7(c) is more pronounced than the shearing shown in Figure 5.6(d). This increased disturbance is also evident in a visual comparison of the B potentials between the two swirl levels, Figures 5.6(e) and 5.7(d). Figure 5.7(e) shows that this flow is asymptoting to a steady state. Like the $V_{\theta 1} = 0.4$ simulation, Figure 5.7(f) shows that the inflow helix angle β is asymptoting to a steady state after 800 timesteps. As with the $V_{\theta 1} = 0.4$ simulation, this flow approaches a steady state after the

initial conditions have washed out of the flow domain.

By increasing the initial swirl level to $V_{\theta 1} = 0.5$, with an inflow helix angle β distribution shown in Figure 5.8(a), the flowfield described by Figure 5.8(b) evolves after 5400 timesteps, or after convecting approximately 7 times through the computational domain. Unlike the $V_{\theta 1} = 0.40$ and $V_{\theta 1} = 0.45$ simulations, this flow does not reach a steady state. Instead it is clear that the flow has stagnated along the pipe centerline. The variation of the minimum axial velocity with time is shown in Figure 5.8(c) where it is evident a stagnation point formed on the axis after approximately 5000 timesteps. This flow stagnation is also evident in Figure 5.8(d) where the Z material co-ordinates at the bottom right hand corner of the outflow are piling up. The fact that these purely convected co-ordinates are stagnating means that the flow is also stagnating. The disturbance is also manifest in the B potential, Figure 5.8(e). Figure 5.8(f) shows the variation with time for the inflow helix angle β . Unlike the inflow helix angle for the $V_{\theta 1} = 0.4$ and $V_{\theta 1} = 0.45$ simulations, this inflow helix angle β does not reach a steady state. Instead, this B is increasing at a constant rate to adjust to the downstream stagnation point. However, the overall change after the initial conditions have been convected through the domain 7 times is only 1%, this small disturbance does not affect the flow.

The onset of the stagnation point is due to physical and not numerical effects. This is supported by the simulations conducted in the straight pipe which were not influenced by numerical disturbances. We are confident that the initial conditions are not triggering a breakdown as the effects of these initial conditions was shown to wash out of the flow domain after 800

timesteps in the $V_{\theta 1} = 0.4$ and $V_{\theta 1} = 0.45$ simulations, and this simulation was run for 5400 timesteps.

In these studies, the flow development occurring after the formation of a stagnation point was not explored. The flow velocities occurring after the formation of a stagnation point tended to grow dramatically because of the absence of viscosity in our simulations, neither physical nor artificially added. The structure of actual breakdown flows is governed by viscous three dimensional effects which are beyond the scope of the present work. As stated in Section 3.2.2, the mechanism causing vortex breakdown is inviscid although the breakdown structure is governed by viscous and three dimensional effects. Since the goal of this work was to predict the occurrence of vortex breakdown in stratified flows and not study the breakdown structure, viscosity was neglected.

Qualitatively, the simulations conducted at swirl levels of $V_{\theta 1} = 0.40$, $V_{\theta 1} = 0.45$ and $V_{\theta 1} = 0.50$ show the same trends as the results reported by Buntine and Saffman. An increase in swirl velocity leads to an increase in the flow deceleration along the pipe axis. Buntine and Saffman do not report quantitative data of their uniform axial flow simulations, so a more rigorous comparison is not possible.

Wang et. al. [1998] conducted inviscid simulations of vortex breakdown by solving the unsteady Euler equations in vorticity streamfunction form. These equations are not limited by the upstream dependence of the steady Bragg-Hawthorne equation. The calculations were conducted in a straight pipe and a vortex breakdown solution was initiated by perturbing a base columnar vortex. A uniform axial flow and a Burgers vortex described by

equation (4.65) were the prescribed inflow conditions. In their simulations there existed a critical level of swirl below which no breakdown could form, regardless of the perturbation magnitude used. This critical level was identified as $V_{\theta 1} = 0.7305$. In the present simulations the divergence angle of the diffuser is the perturbation which causes a breakdown to occur, and the critical swirl level has been identified as $V_{\theta 1} = 0.5$. The fact that less swirl is required to precipitate a breakdown in a diverging tube is in agreement with the experimental observations of Sarpkaya [1974]. Furthermore, Rusak et. al. [1997] studied the effect of pipe divergence on vortex breakdown analytically, and found that pipe divergence reduces the swirl level required to trigger a breakdown. Wang and Rusak and Sarpkaya both attributed the appearance of vortex breakdown at swirl numbers less than critical to the adverse pressure gradient found in diverging tubes.

Text resumes on page 117

Increment = 0.1
 Maximum Value = 1.1
 Minimum Value = 0.4



Figure 5.7(a): Axial Velocity After 3200 timesteps ($V_{\theta 1} = 0.45$)

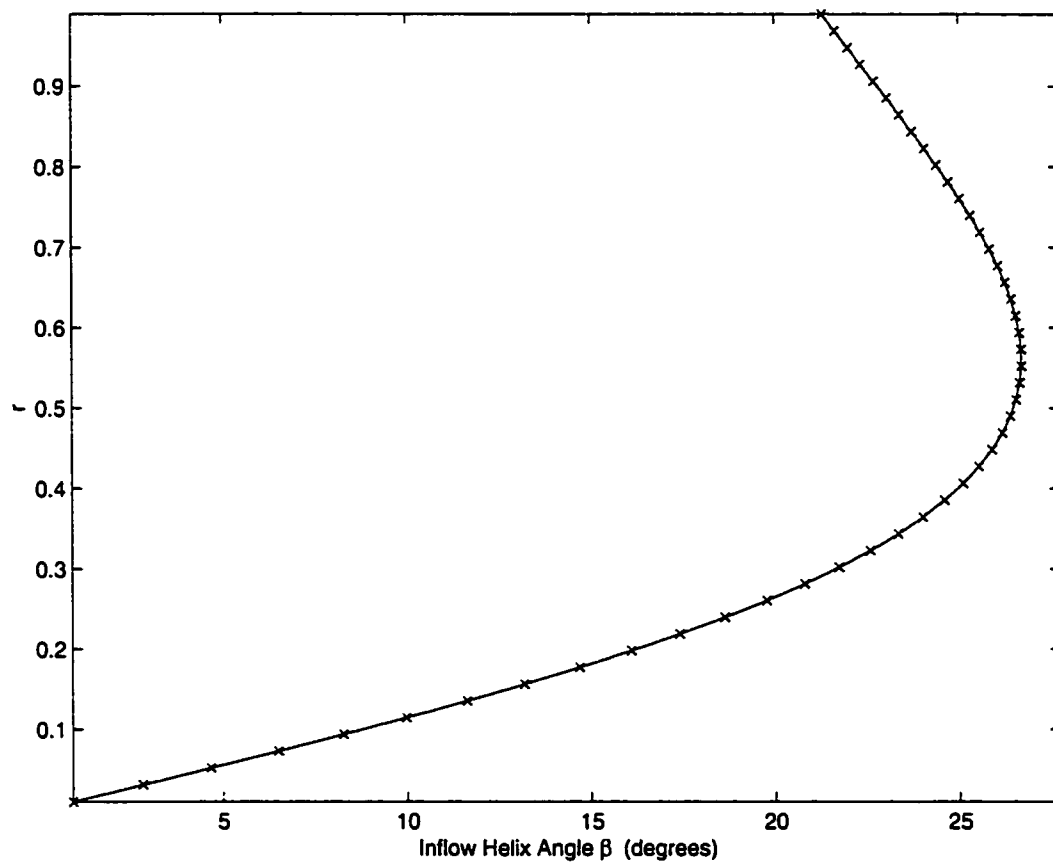


Figure 5.7(b): Inflow Helix Angle β ($V_{\theta 1} = 0.45$)

Increment = 1
 Maximum Value = -24
 Minimum Value = -34



Figure 5.7(c): Z Material Co-ordinate After 3200 timesteps ($V_{\theta 1} = 0.45$)

Increment = -5
 Maximum Value = -60
 Minimum Value = -10

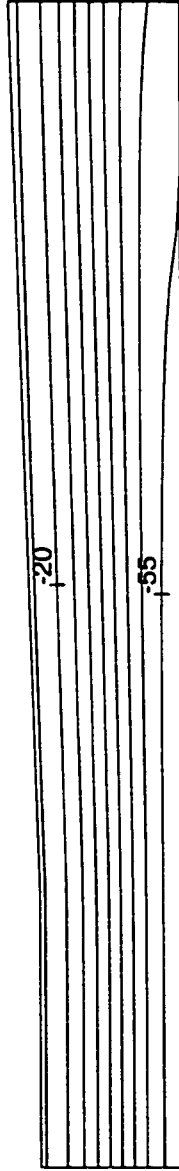


Figure 5.7(d): *B* Potential After 3200 timesteps ($V_{\theta 1} = 0.45$)

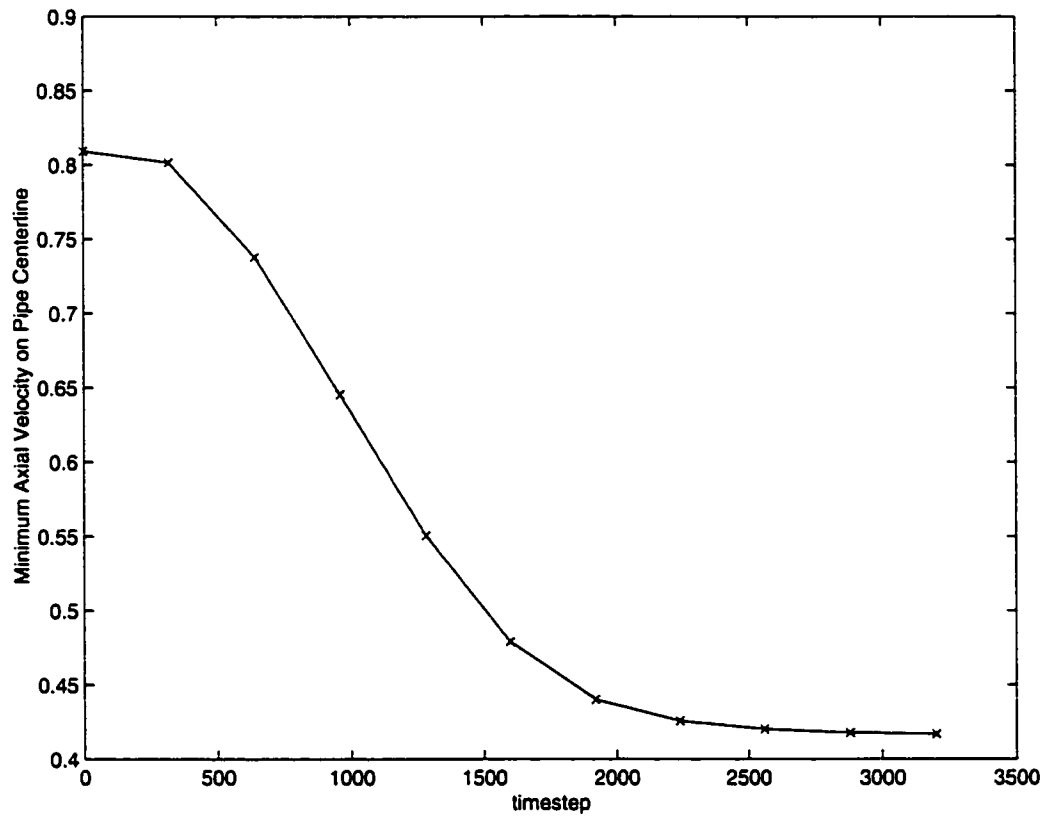


Figure 5.7(e): Convergence of Minimum Axial Velocity ($V_{\theta 1} = 0.45$)

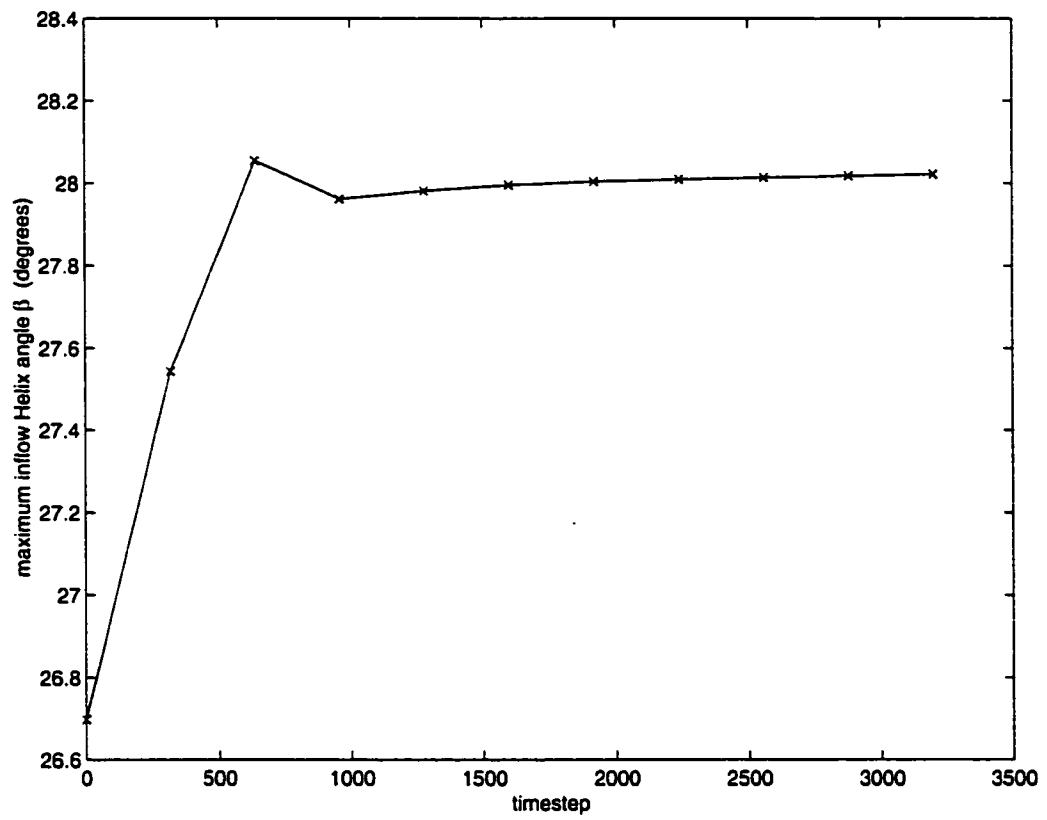


Figure 5.7(f): Temporal Variation of Inflow Helix Angle β ($V_{\theta 1} = 0.45$)

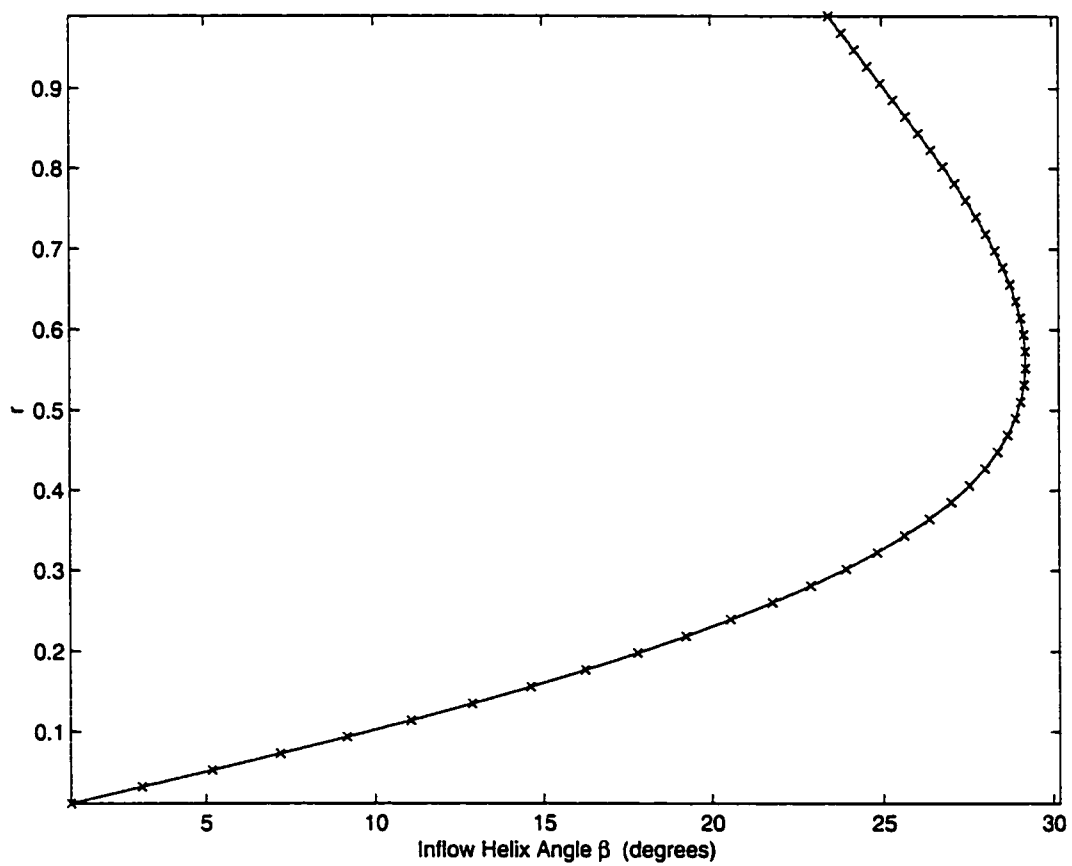


Figure 5.8(a): Inflow Helix Angle β ($V_{\theta 1} = 0.5$)

Increment = 0.1
 Maximum Value = 1.1
 Minimum Value = 0



Figure 5.8(b): Axial Velocity After 5400 timesteps ($V_{\theta 1} = 0.5$)

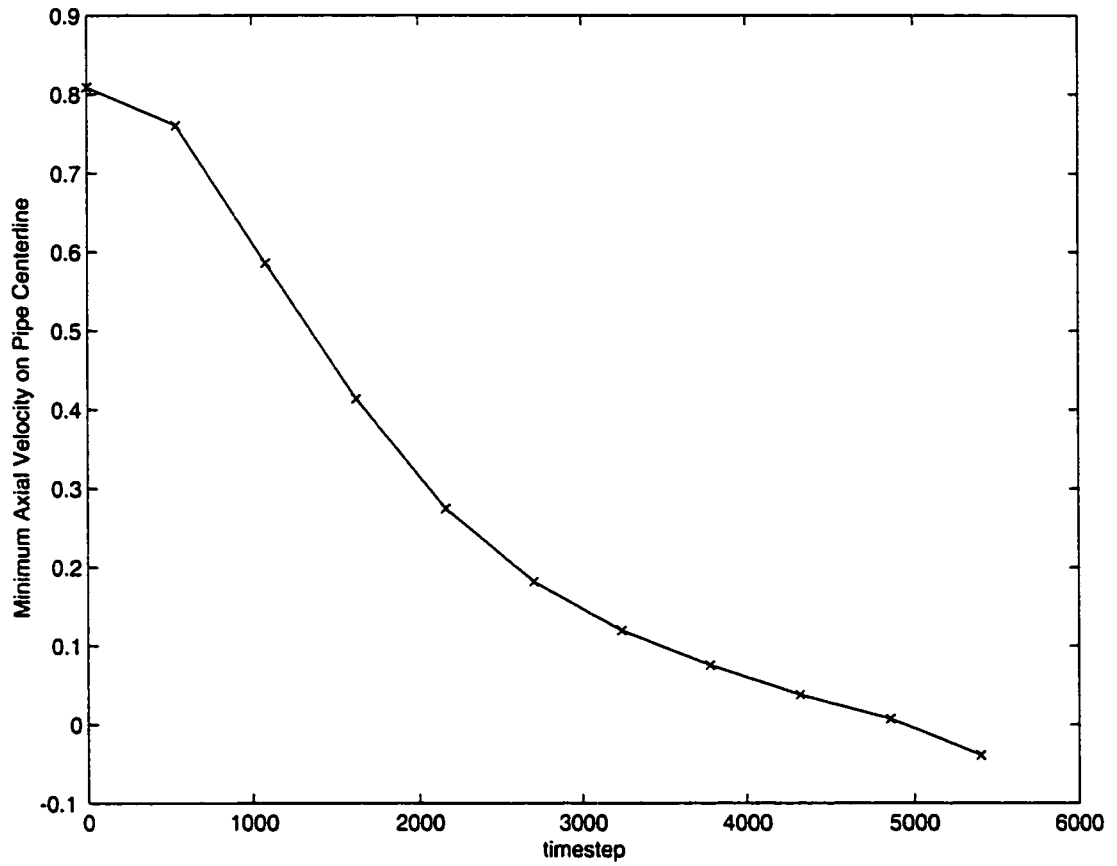


Figure 5.8(c): Variation of Axial Velocity With Time ($V_{\theta 1} = 0.5$)

Increment = 2
 Maximum Value = -28
 Minimum Value = -58



Figure 5.8(d): Z Material Co-ordinate After 5400 timesteps ($V_{\theta 1} = 0.5$)

Increment = 10
 Maximum Value = -20
 Minimum Value = -110

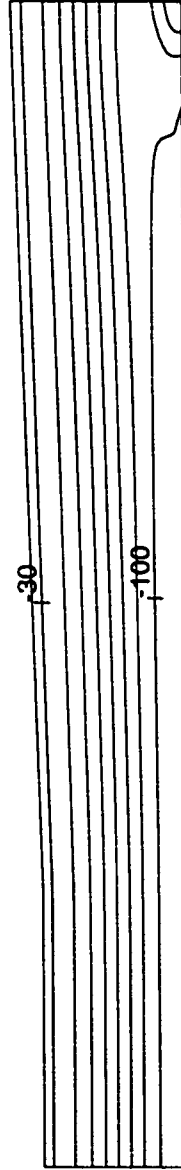


Figure 5.8(e): *B* Potential After 5400 timesteps ($V_{\theta 1} = 0.5$)

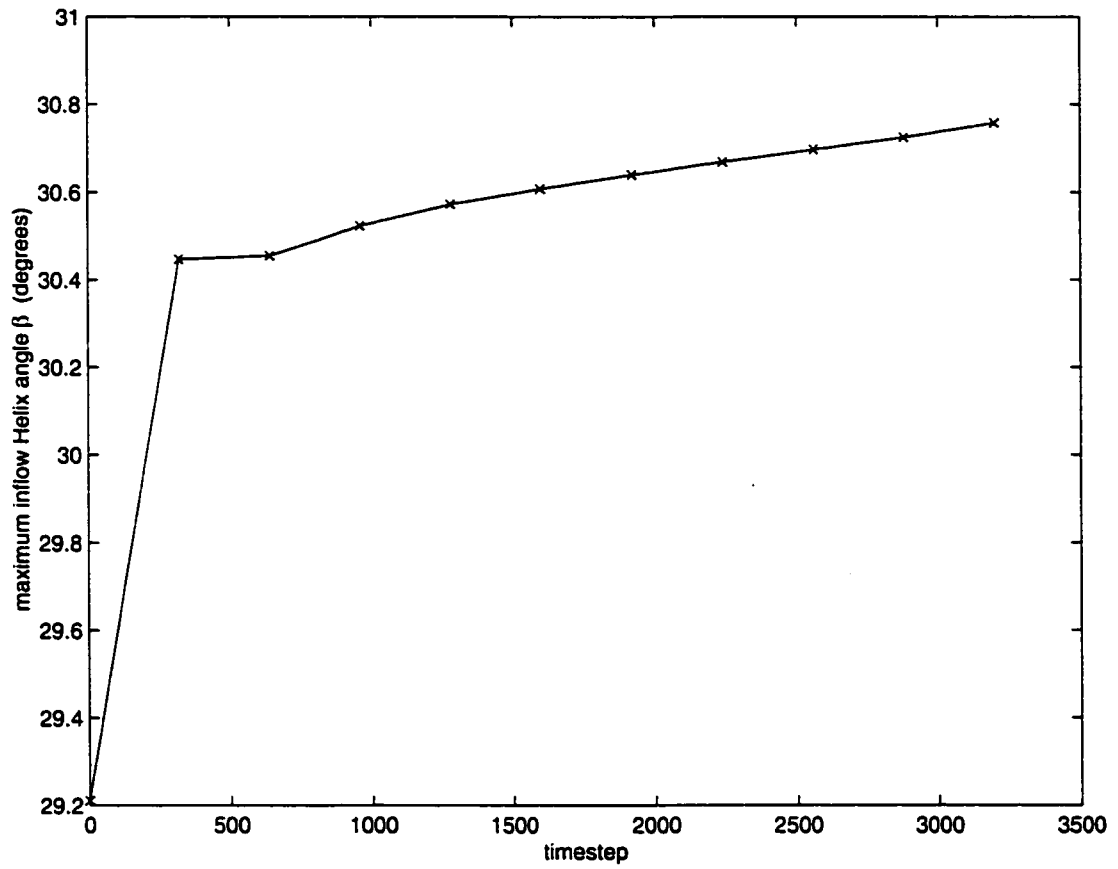


Figure 5.8(f): Temporal Variation of Inflow B ($V_{\theta 1} = 0.5$)

5.2.4 Response of Breakdown Zone to Increased Swirl

Figure 5.9(a) is the inflow helix angle β for a flow with a swirl level of $V_{\theta 1} = 0.55$. Figure 5.9(b) shows the axial velocity for this flow after convecting 4 times through the numerical domain (3200 timesteps). The stagnation point in Figure 5.9(b) occurs approximately 1 unit upstream of the stagnation point in Figure 5.8(b). The stagnation point can also be identified using the Z material co-ordinates, Figure 5.9(c). This movement of the stagnation point is in qualitative agreement with the experimental observations of Sarpkaya [1971a 1971b] and Faler and Leibovich [1977a] who observed the upstream migration of a breakdown zone in response to an increase in swirl level. The structure of the B potential after 3200 timesteps indicates that a large disturbance has developed in the flow, and the disturbance is approximately one half of a pipe radius in radial extent.

At the swirl levels of $V_{\theta 1} = 0.5$ and $V_{\theta 1} = 0.55$, the stagnation point on the flow axis occurred 0.5 units and 1.5 units upstream of the pipe outlet. The stagnation zone in these simulations extends from the initial stagnation point through the pipe outlet, forming an open stagnation zone. This stagnation zone is particularly clear in the Z material co-ordinates, Figure 5.9(c). The dense collection of material lines near the outlet boundary indicates that the fluid in this region is not being convected out of the flow domain. Wang et. al. [1998] conducted numerical simulations using an unsteady form of the Bragg-Hawthorne equation. Unlike the steady Bragg-Hawthorne equation, this equation is valid after the formation of a stagnation point. Wang et. al. predicted open stagnation zones for all swirl levels. They state that the open stagnation zone appears since their simulations are inviscid, and claim that

it is viscosity which causes the closing of a vortex breakdown bubble and the formation of a second stagnation point.

Figure 5.10(a) shows a breakdown flow with a swirl level of $V_{\theta 1} = 0.6$ after convecting 4 times through the domain (3200 timesteps). The inflow helix angle β for this flow is as shown in Figure 5.10(b). The maximum inflow helix angle β varies by 7% over the course of this simulation, Figure 5.10(c). This variation is due to the presence of a large breakdown region in the downstream flow. This large disturbance is evident in Figure 5.10(d). Since the $V_{\theta 1} = 0.5$ swirling flow underwent breakdown with only a 1% variation in the maximum helix angle β , it is clear that the $V_{\theta 1} = 0.6$ breakdown is not due to the inflow disturbance. Figure 5.10(e) shows the axial velocity along the pipe centerline when a vortex breakdown has formed. This plot shows that an identifiable stagnation zone forms between $z = 4.9$ units and $z = 5.5$ units to give a breakdown bubble 0.6 units long. The axial velocity after this breakdown zone recovers to 20% of the inflow value. The formation of this closed stagnation zone in an inviscid flow suggests that it is possible for a vortex breakdown bubble to form without viscosity. The B potential only changes in regions of axial and swirl velocity gradients. Figure 5.10(f) offers a particularly clear picture of the disrupted flow region which we call the bubble, and the surrounding regions of quiescent flow. Figure 5.10(g) and Figure 5.10(h) illustrate the F potential. The largest axial gradients in F are clearly found in the bubble region of the flow. These large gradients are indicative of the the large pressure gradients which are retarding the flow along the axis. Outside of the breakdown region, the gradients in the F potential are mostly radial. The breakdown bubble acts as a flow blockage

which the fluid must pass over. The radial gradients in F are required to deflect the flow around the breakdown region.

The presence of a closed stagnation zone is in disagreement with the results presented by Wang et. al. A definitive reason for this difference is not clear. Wang et. al.'s simulations were conducted in a straight pipe, and it is possible that the closing of the stagnation zone in this work is due to the use of a diverging pipe. It is also possible that the formation of the bubble is a second order effect not found in Wang et. al.'s first order accurate simulations.

Text resumes on page 132

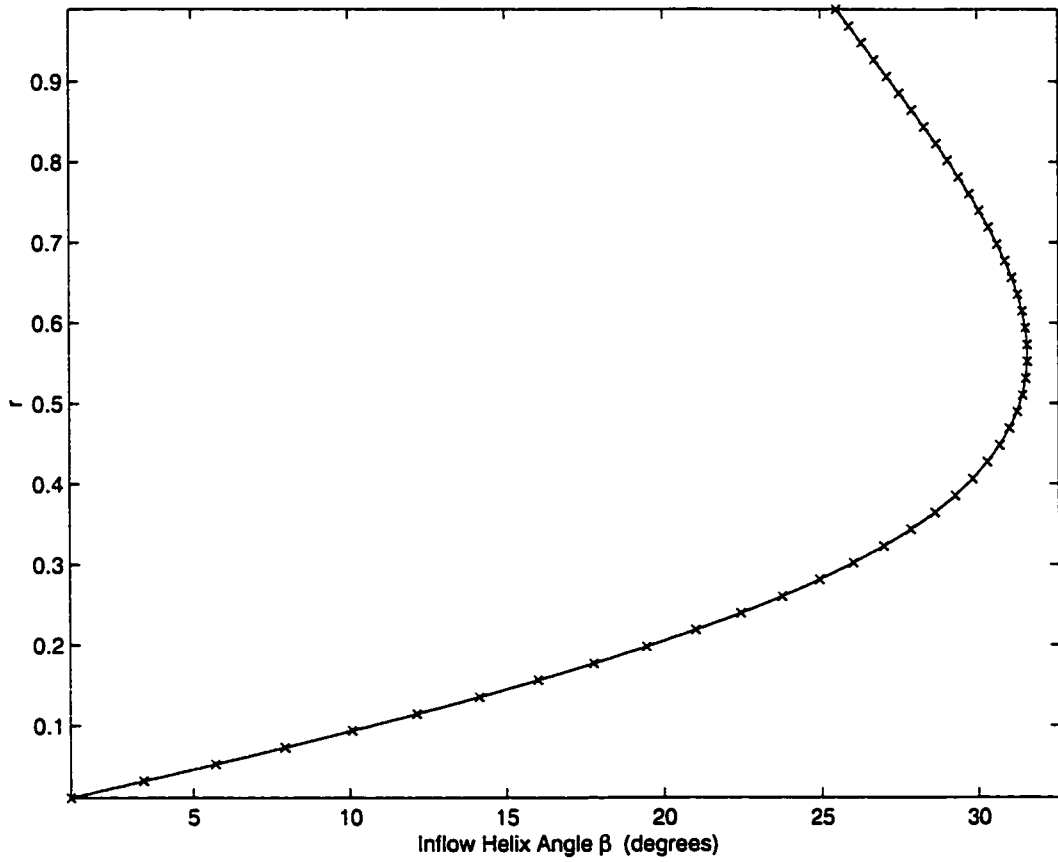


Figure 5.9(a): Inflow Helix Angle β Potential ($V_{\theta 1} = 0.55$)

Increment = 0.1
 Maximum Value = 1.1
 Minimum Value = 0



Figure 5.9(b): Axial Velocity After 3200 timesteps ($V_{\theta 1} = 0.55$)

Increment = 2
 Maximum Value = -10
 Minimum Value = -34



Figure 5.9(c): Z Material Co-ordinate After 3200 timesteps ($V_{\theta 1} = 0.55$)

Increment = 5
 Maximum Value = -15
 Minimum Value = -70

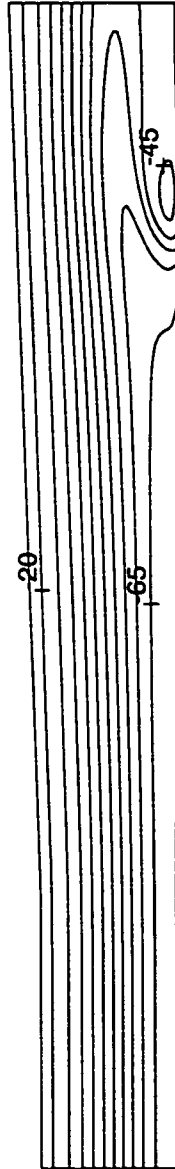


Figure 5.9(d): B Potential After 3200 timesteps ($V_{01} = 0.55$)

Increment = 0.1
 Maximum Value = 1.1
 Minimum Value = 0

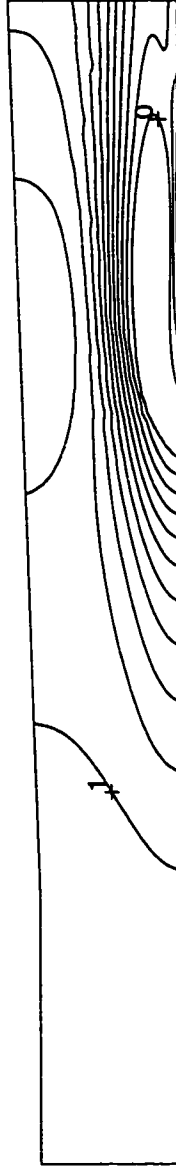


Figure 5.10(a): Axial Velocity After 3200 timesteps ($V_{\theta 1} = 0.60$)

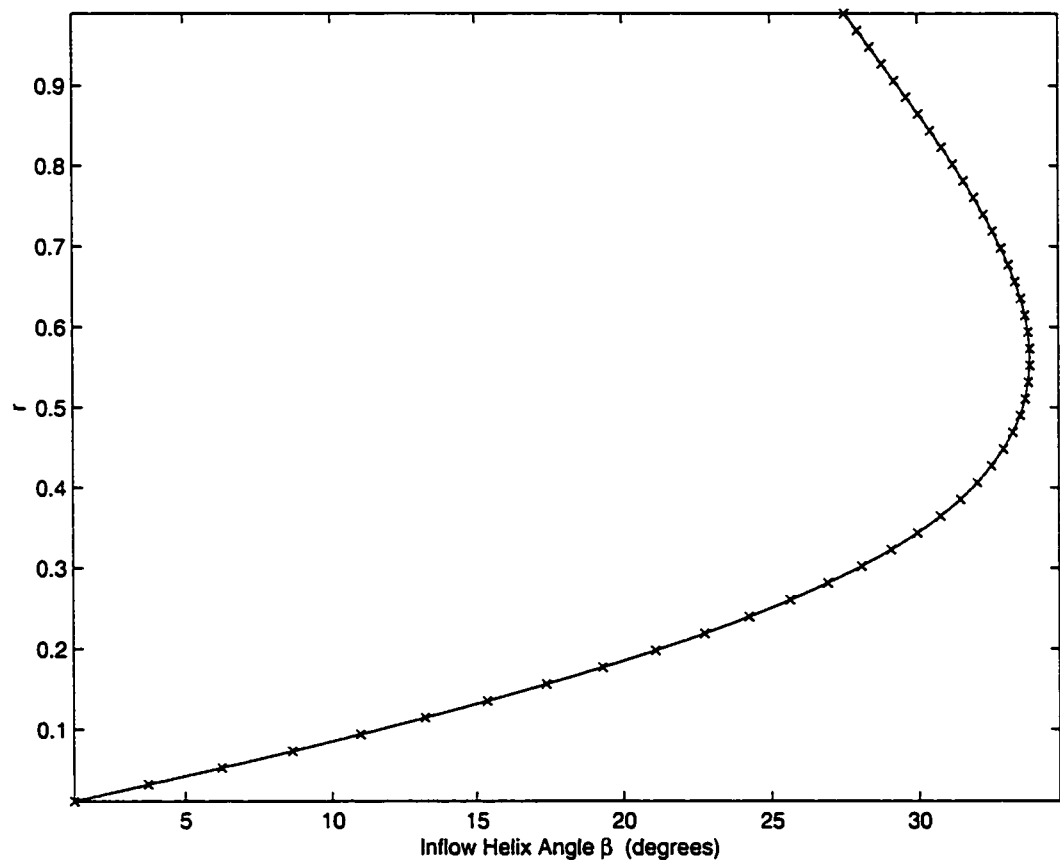


Figure 5.10(b): Inflow Helix Angle β ($V_{\theta 1} = 0.60$)

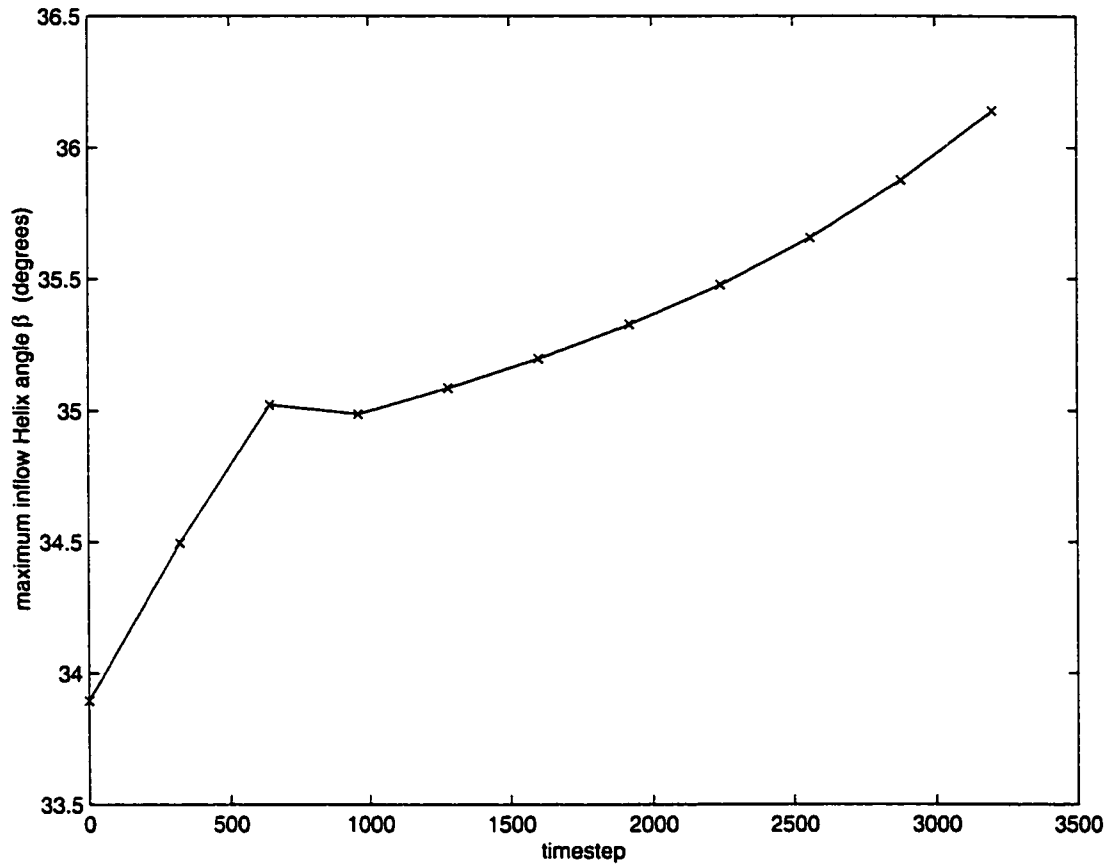


Figure 5.10(c): Temporal Variation of Inflow Helix Angle β ($V_{\theta 1} = 0.60$)

Increment = 2
 Maximum Value = -10
 Minimum Value = -34



Figure 5.10(d): Z Material Co-ordinate After 3200 timesteps ($V_{\theta 1} = 0.60$)

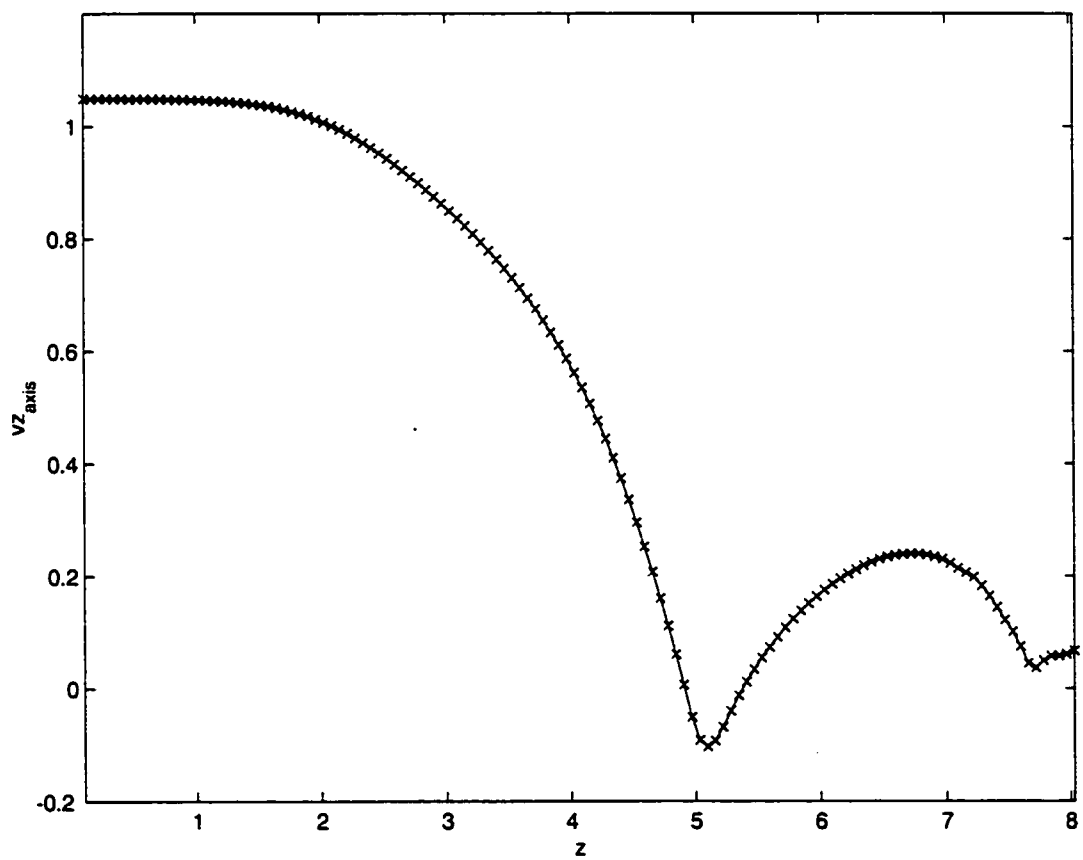


Figure 5.10(e): Axial Variation of Axial Velocity at Breakdown ($V_{\theta 1} = 0.60$)

Increment = 6
 Maximum Value = -20
 Minimum Value = -80

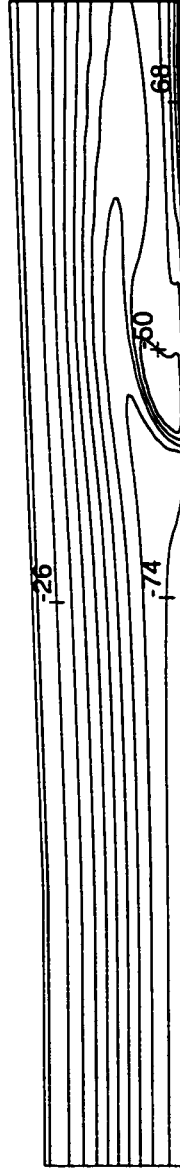


Figure 5.10(f): B Potential After 3200 timesteps ($V_{\theta_1} = 0.60$)

Increment = 2
 Maximum Value = 27
 Minimum Value = 1

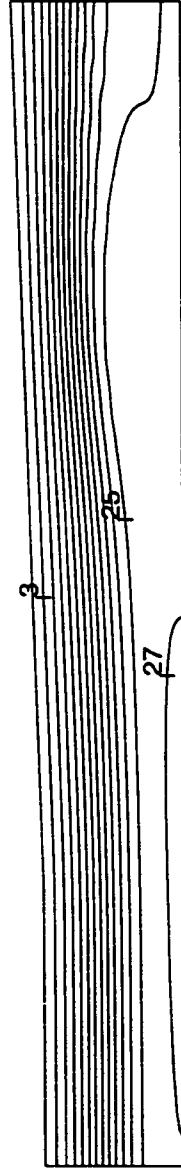


Figure 5.10(g): F Potential After 3200 timesteps ($V_{\theta 1} = 0.60$)

Increment = 0.3
 Maximum Value = 27
 Minimum Value = 24

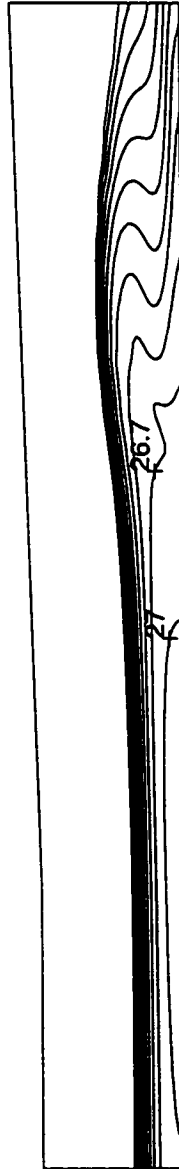


Figure 5.10(h): Detailed F Potential After 3200 timesteps ($V_{\theta 1} = 0.60$)

The preceding seven simulations have shown that the equations resulting from a kinematic decomposition of an axisymmetric swirling flowfield result in vortex breakdown solutions that follow expected behavior. Both swirling and non-swirling flows in a straight pipe convect through the domain unaltered. A non-swirling flow in a diverging pipe also convects through the computational domain unaltered. A low level swirling flow through a diverging pipe experiences a more pronounced flow deceleration along the pipe axis than it does along the pipe walls, in accordance with the solutions of Batchelor [1967]. As the swirl level is increased this flow deceleration becomes more pronounced, until the flow stagnates along the pipe axis in agreement with the results of Buntine and Saffman [1992]. With a further increase in swirl the location of the stagnation point is moved upstream in accordance with the experimental observations of Leibovich [1977a] and Sarpkaya [1971a].

5.3 Vortex Breakdown in Density Stratified Fluids

The results presented thus far have demonstrated the validity of using a potential/complex lamellar velocity decomposition to study vortex breakdown flows. A benefit of using such a velocity decomposition is that pressure is removed from the governing equations and density is treated as a material quantity. This allows for the calculation of density stratified fluids using an Eulerian grid without the use of a density interface boundary condition or grid regeneration at each timestep. The fluids considered in this work are immiscible stratified media.

5.3.1 Summary of the Vorticity Dynamics of Vortex Breakdown

The vorticity equation for an inviscid fluid can be written as:

$$\frac{D\bar{\omega}}{Dt} = (\bar{\omega} \cdot \nabla) \bar{v} + \frac{\nabla \rho \times \nabla P}{\rho^2} \quad (5.6)$$

where:

$$\omega_z = \frac{1}{r} \frac{\partial (rv_\theta)}{\partial r} \quad (5.7)$$

$$\omega_r = -\frac{\partial v_\theta}{\partial z} \quad (5.8)$$

$$\omega_\theta = \frac{\partial v_r}{\partial z} - \frac{\partial v_z}{\partial r} \quad (5.9)$$

The first term on the right hand side of equation (5.6) represents the tilting and stretching of the vorticity components. The cross product term is known as the Baroclinic torque and represents the creation of vorticity in the presence of density and pressure gradients. For an axisymmetric flow, gradients of density and pressure are only present in the (r, z) plane and as a result only azimuthal vorticity can be created in such a flow.

The vorticity dynamics occurring in vortex breakdown flows was discussed in Section 2.4. Brown and Lopez [1990] observed that the presence of negative azimuthal vorticity in a flow is a necessary condition for the formation of a vortex breakdown. Darmofal [1993] argued that the negative azimuthal vorticity is generated by a tilting of the axial vorticity into the azimuthal direction and is then intensified through vortex stretching. Darmofal's work dealt with homogeneous flows, the presence of a density stratification and the Baroclinic torque was not considered.

The sign of the azimuthal vorticity created in these flows is governed by the signs of local density and pressure gradients. Only radial density

gradients are considered in this work, therefore there are four possible combinations of density and pressure gradients creating azimuthal vorticity in these flows. The four scenarios are illustrated in Figure 5.11.

Taking the curl of the potential/complex lamellar velocity decomposition, equation (3.54), the azimuthal vorticity created by density and pressure gradients can also be written as:

$$\omega_\theta = -\frac{\nabla \rho \times \nabla F}{\rho^2} \quad (5.10)$$

The four possible vorticity fields produced by radial density gradients and axial gradients in the F potential are shown in Figure 5.12.

In Section 5.1.4 the flow with a swirl level of $V_{\theta 1} = 0.5$ was identified as the critical flow; a swirl level less than $V_{\theta 1} = 0.5$ will not cause a breakdown in the given geometry. Stratification was first added to this flow as the stabilizing/destabilizing effects of stratification should be most evident around this critical level.

The initial axial vorticity field of a constant density critical flow is shown in Figure 5.13(a). The azimuthal vorticity field is of the order $O(10^{-5})$ and is not contoured here. The axial and azimuthal vorticity fields after 5400 timesteps are shown in Figure 5.13(b) and Figure 5.13(c) respectively. The initial vorticity is all aligned in the axial direction, and when a breakdown solution is reached an azimuthal vorticity component has developed which is negative and of the same order as the axial vorticity. Equation (5.6) shows that a homogeneous flow has no sources of vorticity indicating that the azimuthal vorticity evolved from a tilting of the axial vorticity into the tangential direction.

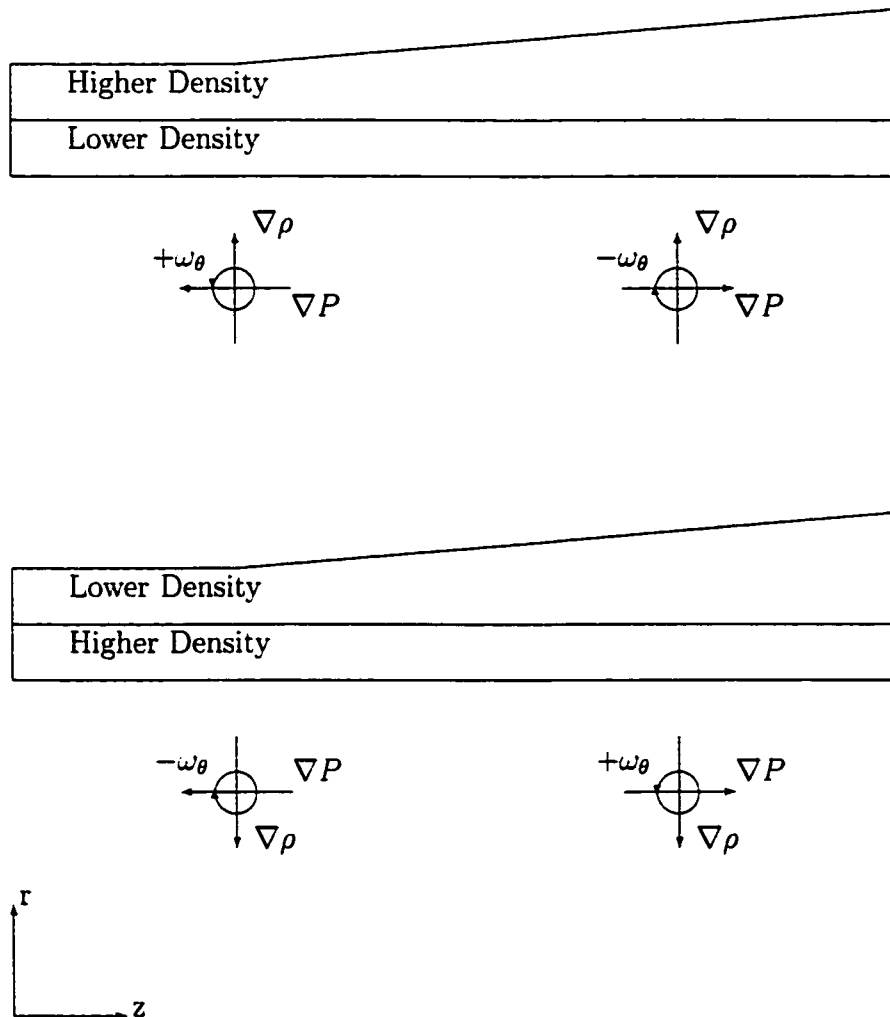


Figure 5.11: Azimuthal Vorticity Created by Different Density/Pressure Gradients

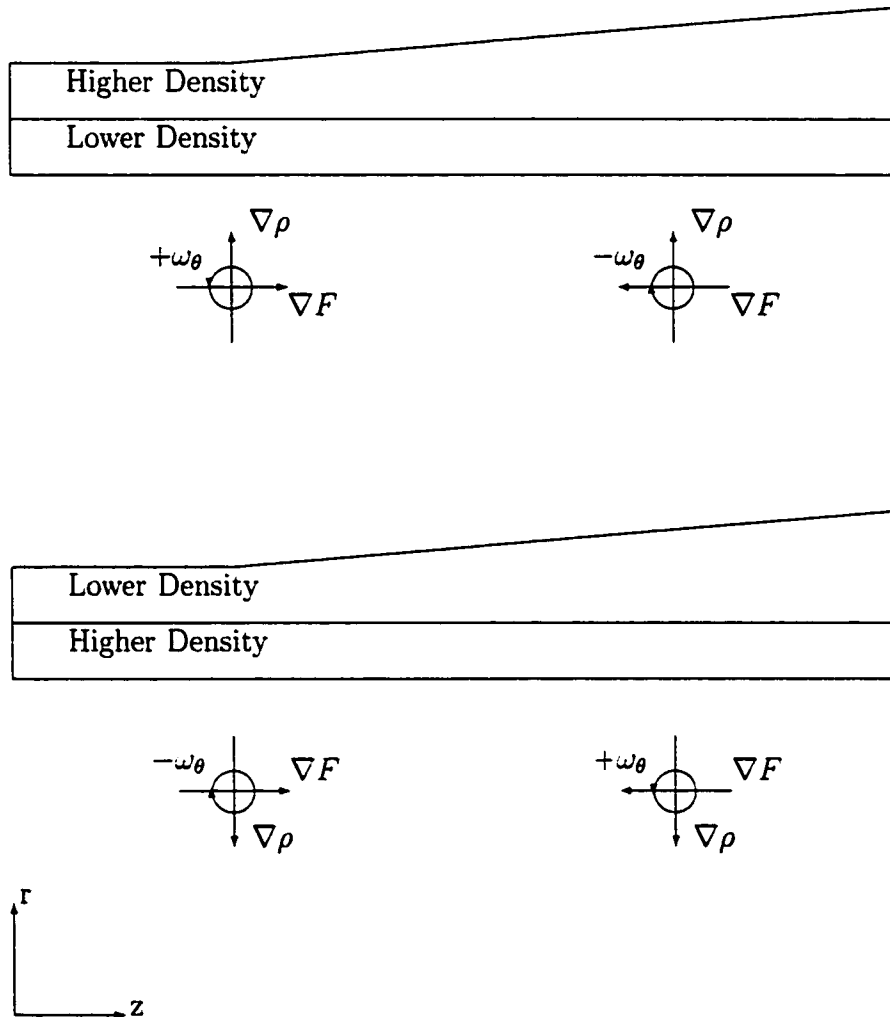


Figure 5.12: Azimuthal Vorticity Created by Different Density/ F Potential Gradients

Increment = 1
Maximum Value = 7
Minimum Value = 0

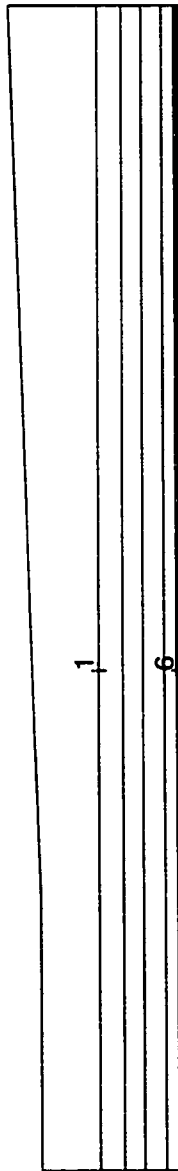


Figure 5.13(a): Initial Axial Vorticity (Homogeneous Flow $V_{\theta 1} = 0.50$)

Increment = 1
 Maximum Value = 7
 Minimum Value = 0

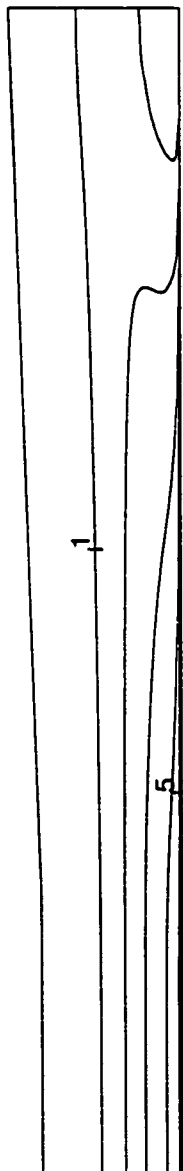


Figure 5.13(b): Axial Vorticity at Breakdown (5400 timesteps) (Homogeneous Flow $V_{\theta 1} = 0.50$)

Increment = 0.2
Maximum Value = 0
Minimum Value = -2

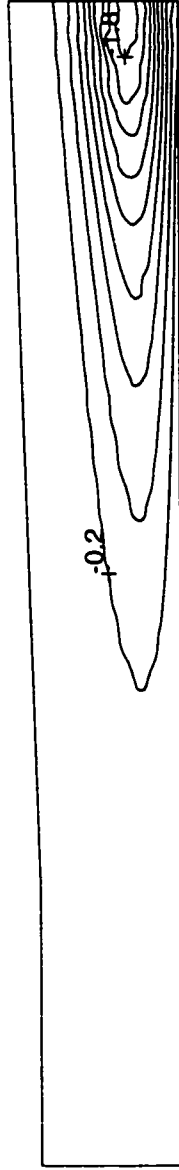


Figure 5.13(c): Azimuthal Vorticity at Breakdown (5400 timesteps) (Homogeneous Flow $V_{01} = 0.50$)

5.3.2 Effect of Negative Density Gradient on Vortex Breakdown

The initial and boundary conditions of the stratified flow cases are identical to those employed in the homogeneous test cases apart from the introduction of a density stratification. The stratification is imposed along the inflow boundary and allowed to convect through the domain governed by equation (3.59). This means that a fully stratified flowfield is not present until after 800 timesteps, or one sweep through the computational domain. The location of the density interface along the inflow boundary is identified as r_s , the density found in the region $0 < r < r_s$ is ρ_1 and the density located in the region $r_s < r < R$ is ρ_2 .

Critical Swirl With Density Interface Outside of Vortex Core

Figure 5.14(a) and Figure 5.14(b) show the axial velocity and the Z material lines for a flow with $r_s = 0.77$, $\rho_1 = 1.0$ and $\rho_2 = 0.9$, giving a negative density gradient in the radial direction. Unlike the homogeneous case the velocity has not stagnated along the pipe centerline. The initial axial vorticity field is represented by Figure 5.13(a) and the azimuthal vorticity is of the order $O(10^{-5})$ and not contoured. At breakdown, the axial vorticity and azimuthal vorticity are as shown in Figures 5.14(c) and 5.14(d) respectively. Figure 5.14(c) and Figure 5.13(b) show that the axial vorticity in homogeneous and stratified breakdown flows is of the same magnitude and varies from a maximum of 7 at the centerline to 0 at the pipe wall. Figure 5.14(e) shows the location of the density interface at breakdown. A visual comparison of Figures 5.13(c) and 5.14(d) shows that the Baroclinic torque has generated a region of concentrated azimuthal vorticity along the density

interface. A notable difference between the axial vorticity in the homogeneous and stratified flow cases is the wave like disturbances present in Figure 5.14(c). This disturbance is reminiscent of a Kelvin Helmholtz instability along the density stratification. Figure 5.14(f) shows that the disturbance is also present along the density interface in the F potential indicating that it is due to a pressure wave. Due to the wave disturbances it is difficult to interpret the azimuthal vorticity field, however, it appears as though the concentrated region of negative azimuthal vorticity at the downstream end of the pipe in the stratified case, differs from that in the homogeneous flow, Figure 5.13(b).

Text resumes on page 148

Increment = 0.1
Maximum Value = 1.1
Minimum Value = 0.1



Figure 5.14(a): Axial Velocity Field After 5400 timesteps (Negative Stratification $r_s = 0.77$ $V_{\theta 1} = 0.50$)

Increment = 1
 Maximum Value = -40
 Minimum Value = -57



Figure 5.14(b): Z Material Field After 5400 timesteps (Negative Stratification $\tau_s = 0.77$ $V_{\theta 1} = 0.50$)

Increment = 1
 Maximum Value = 7
 Minimum Value = 0

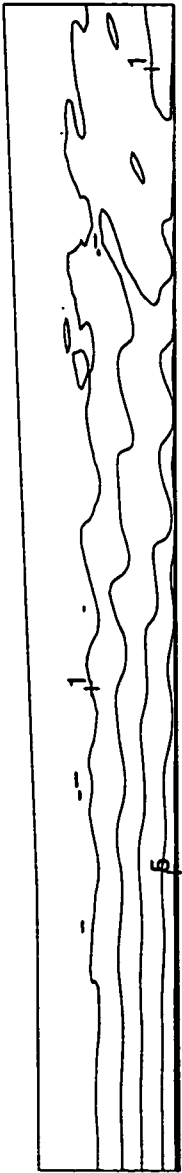


Figure 5.14(c): Axial Vorticity After 5400 timesteps (Negative Stratification $r_s = 0.77$ $V_{\theta 1} = 0.50$)

Increment = 0.5
 Maximum Value = 3
 Minimum Value = -2



Figure 5.14(d): Azimuthal Vorticity After 5400 timesteps (Negative Stratification $r_s = 0.77$ $V_{\theta 1} = 0.50$)

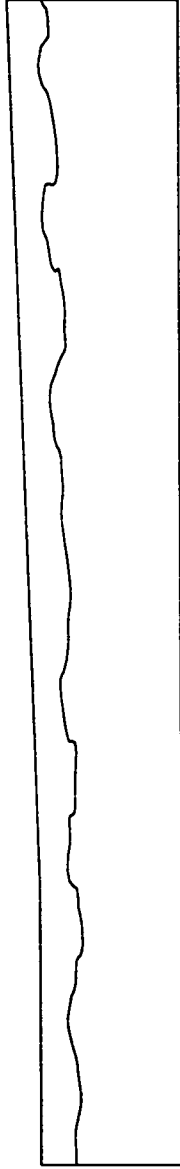


Figure 5.14(e): Density Interface After 5400 timesteps (Negative Stratification $r_s = 0.77$ $V_{\theta 1} = 0.50$)

Increment = 3
 Maximum Value = 31
 Minimum Value = 1

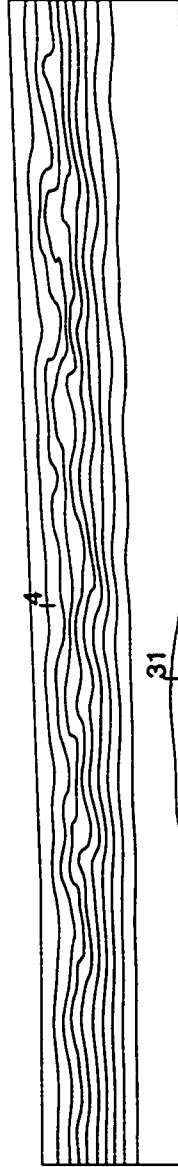


Figure 5.14(f): F Potential After 5400 timesteps (Negative Stratification $r_s = 0.77$ $V_{\theta 1} = 0.50$)

Critical Swirl With Density Interface Inside of Vortex Core

The axial velocity and Z material field for a flow with $r_s = 0.25$, $\rho_1 = 1.0$ and $\rho_2 = 0.9$ are shown in Figures 5.15(a) and 5.15(b) respectively. Again the presence of a negative density gradient in the radial direction has hindered the occurrence of a breakdown solution. The initial axial vorticity field is represented by Figure 5.13(a) and the azimuthal vorticity is of the order $O(10^{-5})$ and not contoured. At breakdown, the axial vorticity and azimuthal vorticity are as shown in Figures 5.15(c) and 5.15(d) respectively. Figure 5.15(c) and Figure 5.13(b) show that the axial vorticity in homogeneous and stratified breakdown flows is of the same magnitude and varies from a maximum of 7 at the centerline to 0 at the pipe wall. A visual comparison of Figures 5.13(c) and 5.15(d) shows that the Baroclinic torque has altered the azimuthal vorticity field. The density interface is shown in Figure 5.15(e). A region of negative azimuthal vorticity has been generated in the straight section of the pipe. Positive azimuthal vorticity has been generated along the density interface in the divergent section, lowering the magnitude of the minimum negative azimuthal vorticity in the homogeneous case by 80%. Figure 5.15(g) shows a negative gradient in the F potential along the density interface. Combined with a negative density gradient in the radial direction, Figure 5.12 shows that the Baroclinic torque creates positive azimuthal vorticity along the density stratification.

Text resumes on page 156

Increment = 0.1
 Maximum Value = 1.1
 Minimum Value = 0.2

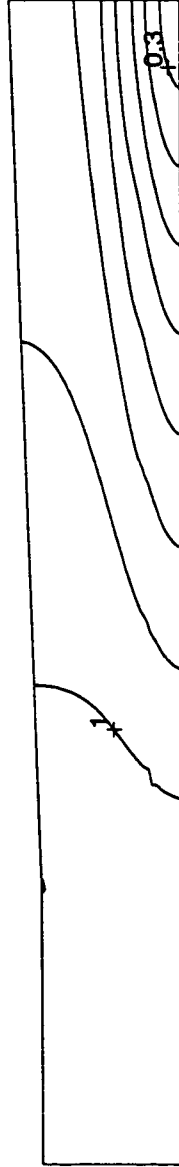


Figure 5.15(a): Axial Velocity After 5400 timesteps (Negative Stratification $r_s = 0.25$ $V_{\theta 1} = 0.50$)

Increment = 1
 Maximum Value = -45
 Minimum Value = -59

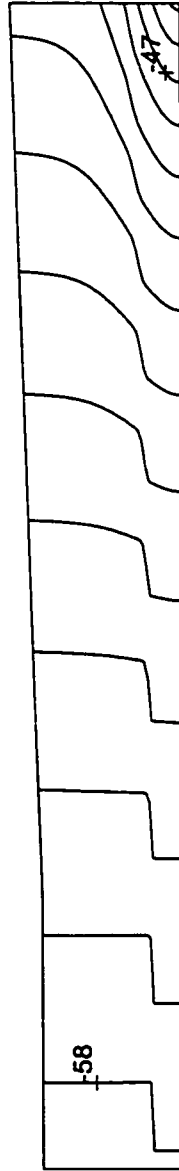


Figure 5.15(b): Z Material Field After 5400 timesteps (Negative Stratification $r_s = 0.25$ $V_{\theta 1} = 0.50$)

Increment = 1
Maximum Value = 7
Minimum Value = 0



Figure 5.15(c): Axial Vorticity After 5400 timesteps (Negative Stratification $r_s = 0.25$ $V_{\theta 1} = 0.50$)

Increment = 0.2
Maximum Value = 0.5
Minimum Value = -1.1



Figure 5.15(d): Azimuthal Vorticity After 5400 timesteps (Negative Stratification $r_s = 0.25$ $V_{\theta 1} = 0.50$)

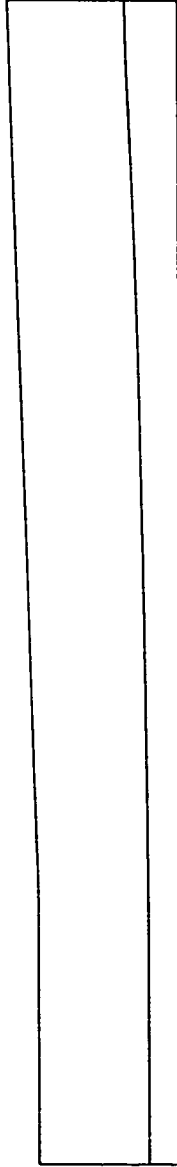


Figure 5.15(e): Density Interface After 5400 timesteps (Negative Stratification $r_s = 0.25$ $V_{\theta 1} = 0.50$)

Increment = 4
Maximum Value = 29
Minimum Value = 1

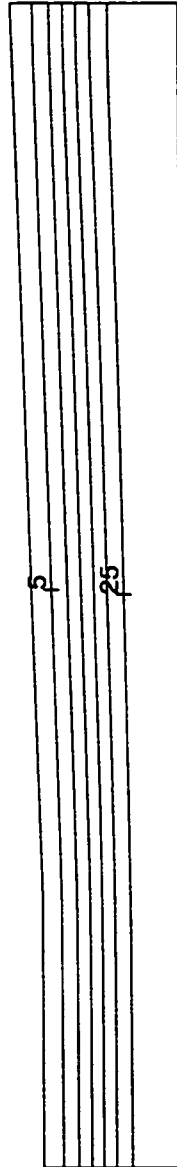


Figure 5.15(f): F Potential After 5400 timesteps (Negative Stratification $r_s = 0.25$ $V_{\theta 1} = 0.50$)

Increment = 0.3
Maximum Value = 29
Minimum Value = 26

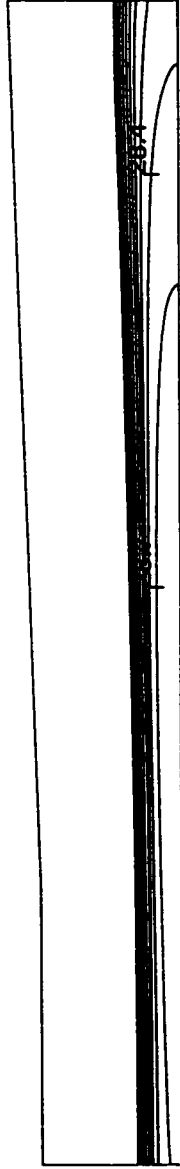


Figure 5.15(g): Detailed F Potential After 5400 timesteps (Negative Stratification $r_s = 0.25$ $V_{\theta 1} = 0.50$)

Stabilizing Effect of Negative Density Gradient

Figure 5.16 shows the variation of the minimum axial velocity along the pipe axis for a homogeneous flow, a flow with $r_s = 0.77, \rho_1 = 1.0, \rho_2 = 0.9$ and a flow with $r_s = 0.25, \rho_1 = 1.0, \rho_2 = 0.9$. This plot shows that a negative density gradient influences breakdown solutions. It also shows that the stratification has a stronger effect when located inside of the vortex core. The homogeneous flow stagnated along the pipe centerline after approximately 5000 timesteps. In the same time, the $r_s = 0.25$ flow is asymptoting to a steady state with a minimum axial velocity of 0.25, and the $r_s = 0.77$ flow has a minimum axial velocity of 0.1 but has not reached a steady state. Darmofal states that breakdown involves the tilting of the axial vorticity in the vortex core into negative azimuthal vorticity. Figure 5.13(c) shows that the negative azimuthal vorticity is concentrated at the downstream end of the pipe. The negative density gradient located inside of the vortex core lowers the magnitude of this vorticity by 80%, thus hindering breakdown. Due to the wave disturbances present when a negative density gradient is located outside of the core, it is difficult to interpret the effects of the stratification. Since the vorticity present in breakdown flows is concentrated in the vortex core, it is reasonable that a stratification located outside of the core will have less effect than one inside.

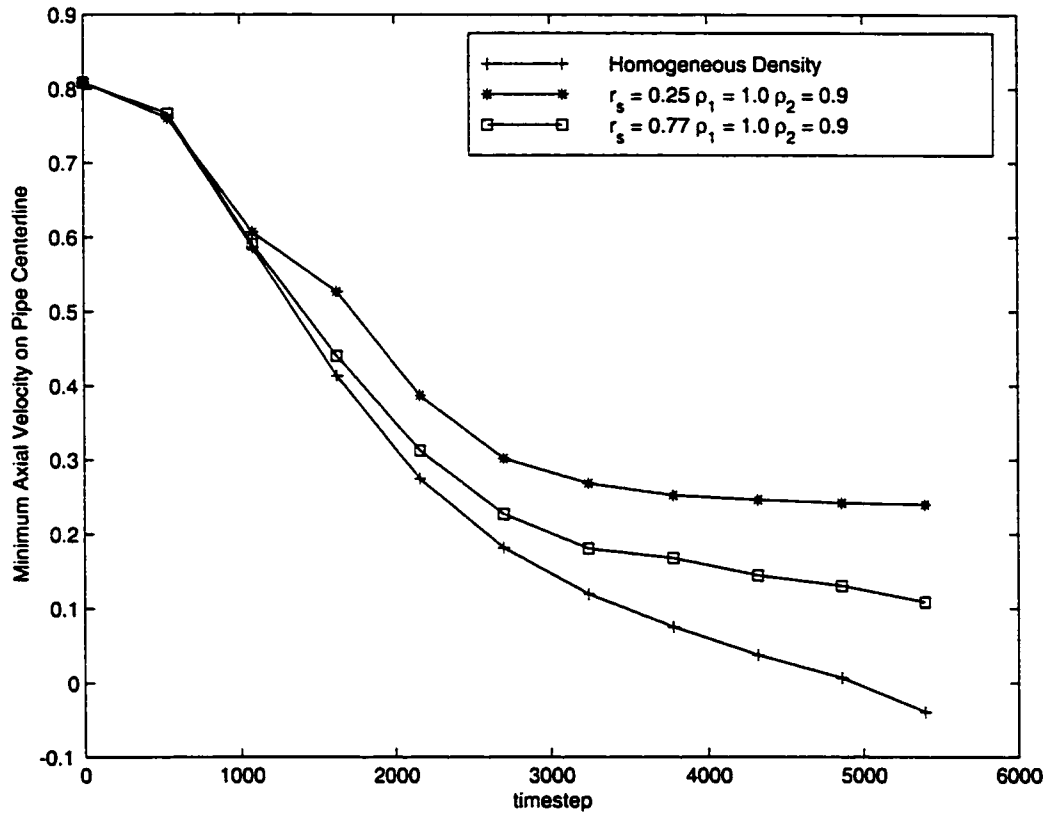


Figure 5.16: Variation of Minimum Axial Velocity Along Pipe Centerline For Various Stratification Locations (Negative Stratification $V_{\theta 1} = 0.50$)

5.3.3 Effect of Positive Density Gradient on Vortex Breakdown

Figure 5.17 shows the variation of the minimum axial velocity along the pipe axis for a homogeneous flow, a flow with $r_s = 0.77, \rho_1 = 0.9, \rho_2 = 1.0$ and a flow with $r_s = 0.25, \rho_1 = 0.9, \rho_2 = 1.0$. The presence of a positive density gradient in the radial direction has promoted the occurrence of vortex breakdown, and the location of the density interface has a stronger effect when located inside of the vortex core. The flow with the stratification located at $r_s = 0.25$ has reached a breakdown state before the flow with the density interface located at $r_s = 0.77$, which has broken down before the homogeneous flow. Figure 5.18(a) shows the azimuthal vorticity in a homogeneous flow after 3200 timesteps. Figures 5.18(b) and 5.18(c) show the azimuthal vorticity after 3200 timesteps for the $r_s = 0.77$ and $r_s = 0.25$ flows respectively. The $r_s = 0.77$ positive density gradient simulation has not generated the oscillations that it did with a negative density gradient, as can be seen on the density interface, Figure 5.18(d). It is clear that the presence of a positive density gradient inside the vortex core, as shown in Figure 5.18(e), has altered the azimuthal vorticity present in the homogeneous case. With the stratification inside the core the magnitude of the minimum azimuthal vorticity is increased by 50%. With the stratification outside of the core the magnitude of the minimum vorticity has not changed. However, the region of minimum azimuthal vorticity is larger in the stratified flow case.

Text resumes on page 165

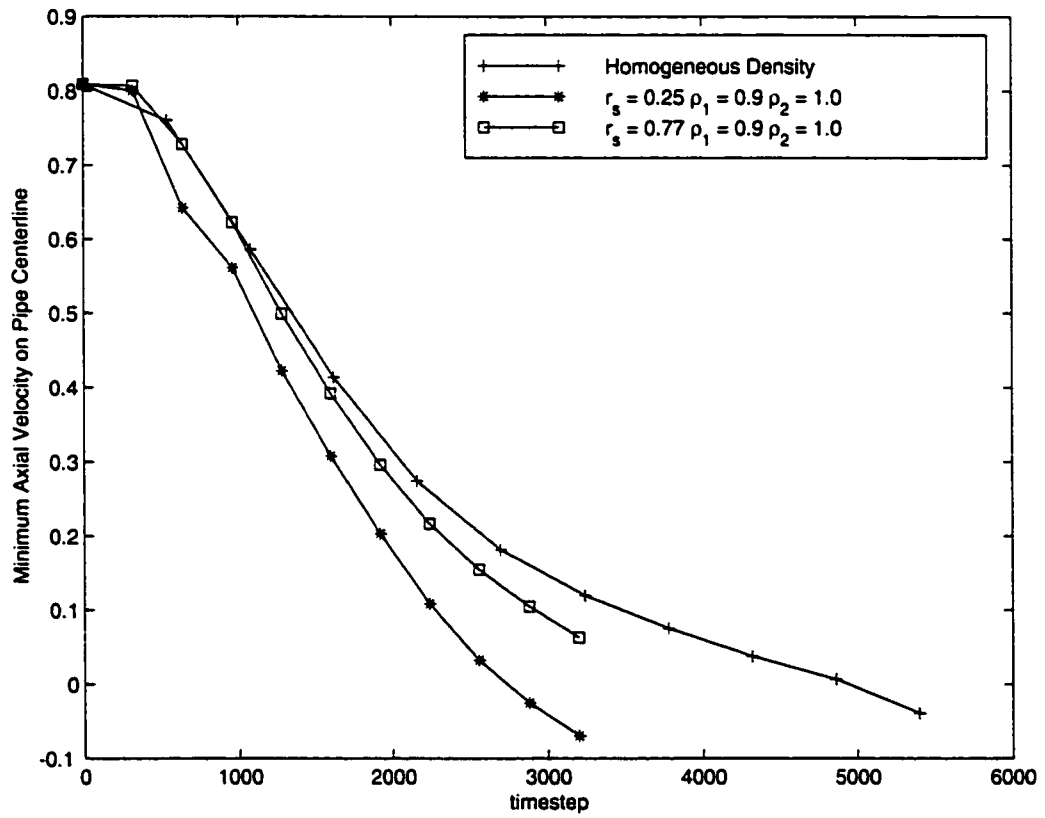


Figure 5.17: Variation of Minimum Axial Velocity Along Pipe Centerline For Various Stratification Locations (Positive Stratification $V_{\theta 1} = 0.50$)

Increment = 0.15
 Maximum Value = 0
 Minimum Value = -1.5

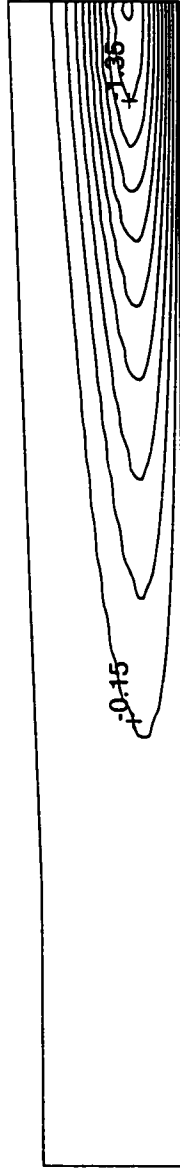


Figure 5.18(a): Azimuthal Vorticity After 3200 timesteps (Homogeneous $V_{\theta 1} = 0.50$)

Increment = 0.2
 Maximum Value = 0.5
 Minimum Value = -1.5

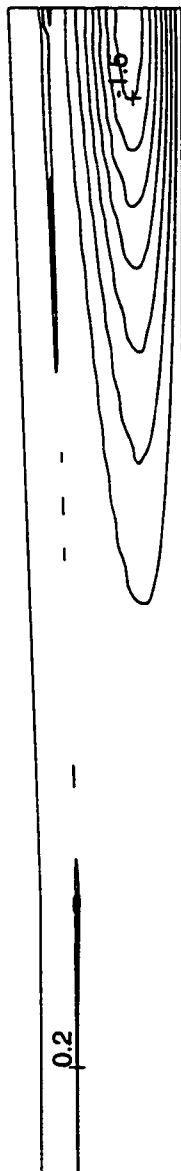


Figure 5.18(b): Azimuthal Vorticity After 3200 timesteps (Positive Stratification $r_s = 0.77$ $V_{\theta 1} = 0.50$)

Increment = 0.3
 Maximum Value = 0.5
 Minimum Value = -2.5

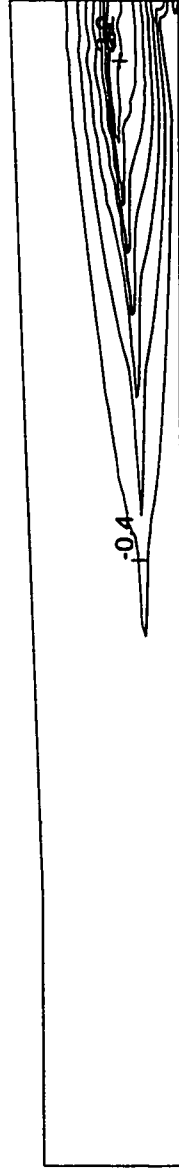


Figure 5.18(c): Azimuthal Vorticity After 3200 timesteps (Positive Stratification $\tau_s = 0.25$ $V_{\theta 1} = 0.50$)

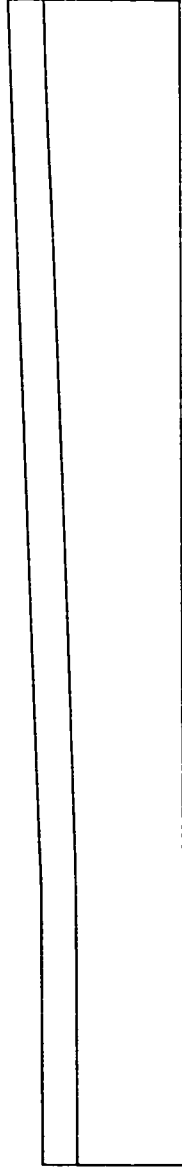


Figure 5.18(d): Density Interface After 3200 timesteps (Positive Stratification $\tau_s = 0.77$ $V_{\theta 1} = 0.50$)

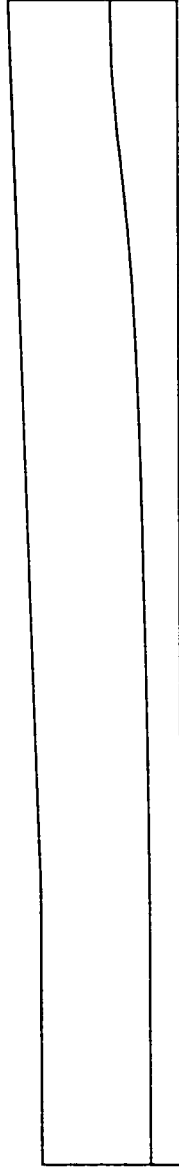


Figure 5.18(e): Density Interface After 3200 timesteps (Positive Stratification $r_s = 0.25$ $V_{\theta 1} = 0.50$)

5.3.4 Effect of Density Stratification on Above Critical Swirl Vortex Breakdown

The results of the previous section examined a vortex breakdown occurring at a swirl level of $V_{\theta 1} = 0.5$. The stagnation point in this flow occurs less than a pipe radius from the outflow boundary and a definable vortex breakdown bubble is not formed. To examine the effect of a density stratification on the location of a breakdown zone, simulations were conducted with a swirl level of $V_{\theta 1} = 0.6$. At this swirl level an identifiable bubble forms and the stagnation point occurs approximately three pipe radii from the outflow boundary.

Figure 5.10(a) shows the axial velocity field for a vortex breakdown occurring in a homogeneous flow. The stagnation region is approximately one half of a pipe radius in length and the initial stagnation point is located at $z = 5.0$. The bubble can also be visualized with the Z material lines and B potential, Figures 5.10(d) and 5.10(f). The initial vorticity field for this flow is shown in Figure 5.19(a) and the azimuthal vorticity is 5 orders of magnitude lower and not contoured. The axial and azimuthal vorticity at breakdown are shown in Figures 5.19(b) and 5.19(c) respectively. The axial vorticity has been tilted into the azimuthal direction as was evident in the $V_{\theta 1} = 0.5$ simulation.

Text resumes on page 169

Increment = 1
Maximum Value = 10
Minimum Value = 0

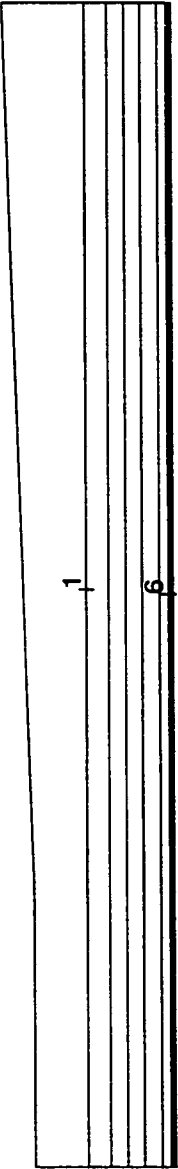


Figure 5.19(a): Initial Axial Vorticity (Homogeneous $V_{\theta 1} = 0.60$)

Increment = 2
 Maximum Value = 20
 Minimum Value = 0



Figure 5.19(b): Axial Vorticity After 3200 timesteps (Homogeneous $V_{\theta 1} = 0.60$)

Increment = 0.6
 Maximum Value = 2
 Minimum Value = -4

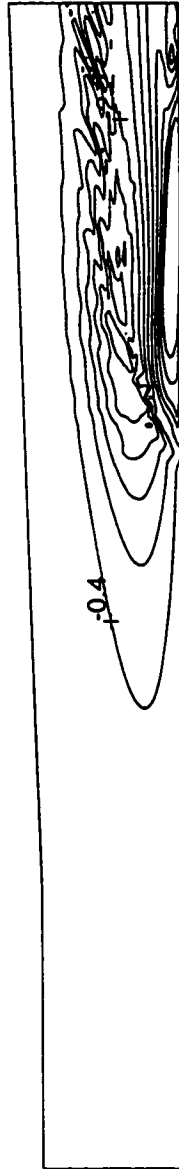


Figure 5.19(c): Azimuthal Vorticity After 3200 timesteps (Homogeneous $V_{\theta 1} = 0.60$)

Figure 5.20 shows the variation of the minimum axial velocity along the pipe axis for a homogeneous flow, a flow with $r_s = 0.77, \rho_1 = 1.0, \rho_2 = 0.9$ and a flow with $r_s = 0.25, \rho_1 = 1.0, \rho_2 = 0.9$. The results show the same trends as reported for the critical swirl flow of the previous section. A negative density gradient hinders the occurrence of a breakdown. The effect is strengthened by locating the density stratification inside the vortex core. Figure 5.21 shows the variation of the minimum axial velocity along the pipe axis for a homogeneous flow, a flow with $r_s = 0.77, \rho_1 = 0.9, \rho_2 = 1.0$ and a flow with $r_s = 0.25, \rho_1 = 0.9, \rho_2 = 1.0$. Again the results show the same trends as reported for the critical swirling flow, a positive density gradient promoting breakdown solutions, and the effect being more pronounced when the stratification is located inside the vortex core.

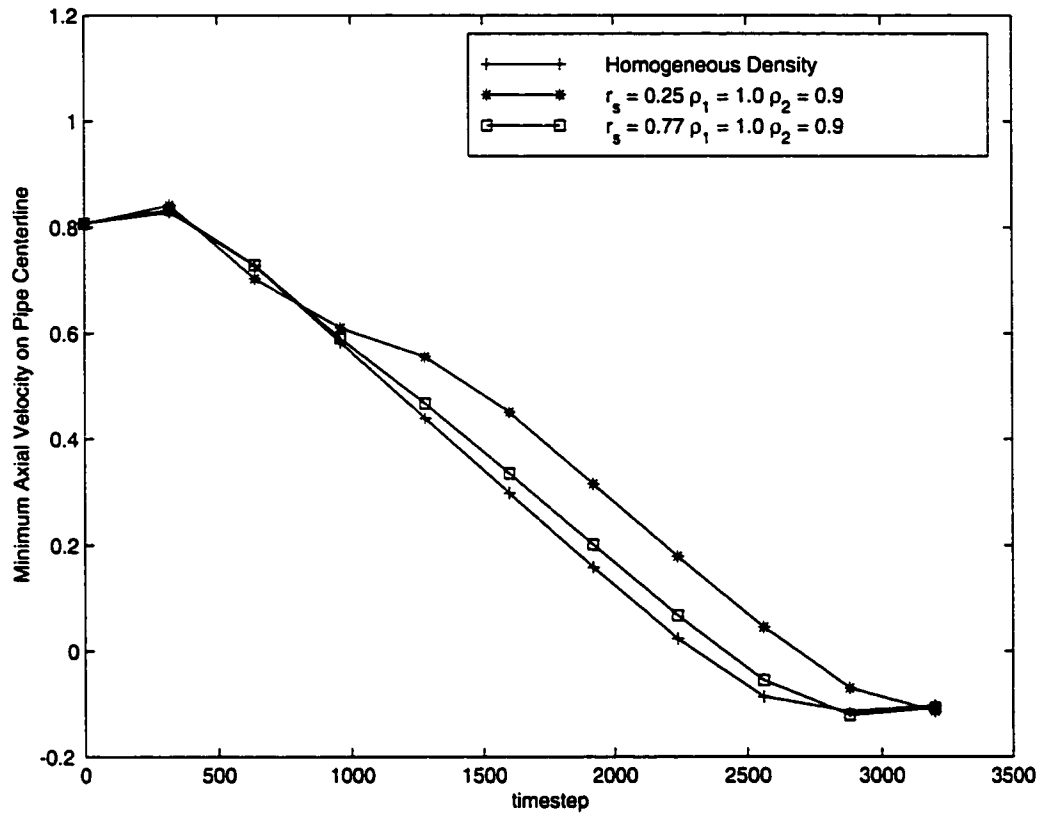


Figure 5.20: Variation of Minimum Axial Velocity Along Pipe Centerline For Various Stratification Locations (Negative Stratification $V_{\theta 1} = 0.60$)

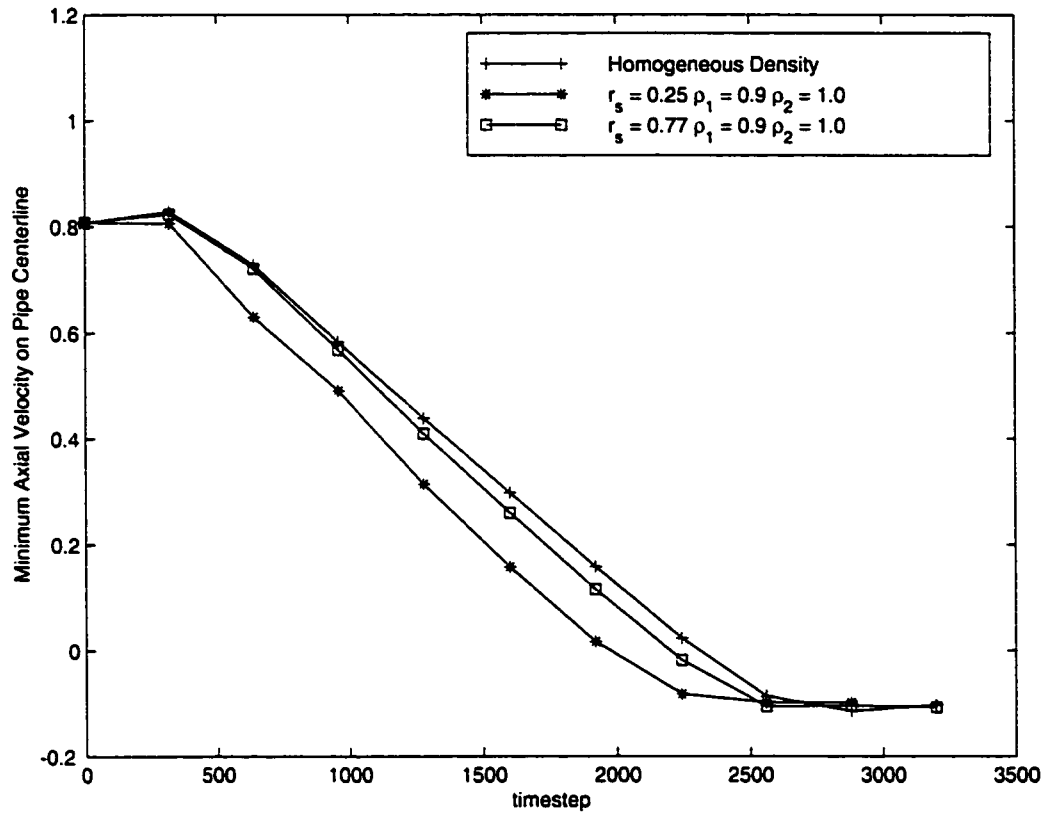


Figure 5.21: Variation of Minimum Axial Velocity Along Pipe Centerline For Various Stratification Locations (Positive Stratification $V_{\theta 1} = 0.60$)

Negative Density Gradient Inside of Vortex Core

A vortex breakdown solution occurring in a stratified flow with the density interface located at $r_s = 0.25$ with $\rho_1 = 1.0$ and $\rho_2 = 0.9$ is illustrated in Figure 5.22(a). The stagnation zone in this flow is 1.0 unit long and the initial stagnation point occurs at $z = 5.6$. Again, the bubble structure can be seen in the Z material lines and B potential, Figures 5.22(b) and 5.22(c). Figures 5.22(d) and 5.22(e) clearly show the F gradients in the bubble region indicating an adverse pressure gradient. The axial and azimuthal vorticity are shown in Figures 5.22(f) and 5.22(g). The density stratification is clearly evident in the density contour of Figure 5.22(h). Positive azimuthal vorticity is being generated along this density interface in the divergent section of the pipe reducing the amount of negative azimuthal vorticity in this region from the homogeneous case. This is why the negative density gradient has inhibited the occurrence of a breakdown solution in Figure 5.20.

Text resumes on page 181

Increment = 0.1
 Maximum Value = 1.1
 Minimum Value = 0



Figure 5.22(a): Axial Velocity Field After 3200 timesteps (Negative Stratification $r_s = 0.25$ $V_{\theta 1} = 0.60$)

Increment = 2
 Maximum Value = -15
 Minimum Value = -35



Figure 5.22(b): Z Material Field After 3200 timesteps (Negative Stratification $r_s = 0.25$ $V_{\theta 1} = 0.60$)

Increment = 5
Maximum Value = -20
Minimum Value = -70

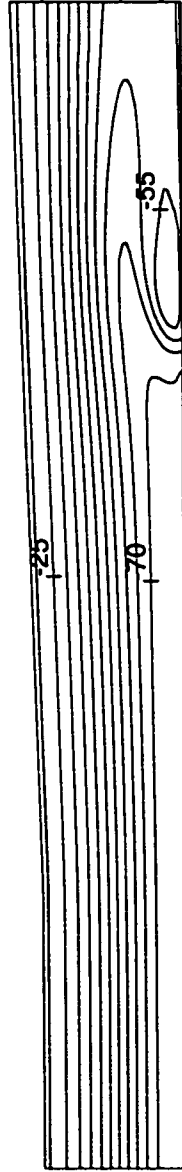


Figure 5.22(c): *B* Potential After 3200 timesteps (Negative Stratification $r_s = 0.25$ $V_{\theta 1} = 0.60$)

Increment = 2
Maximum Value = 25
Minimum Value = 1

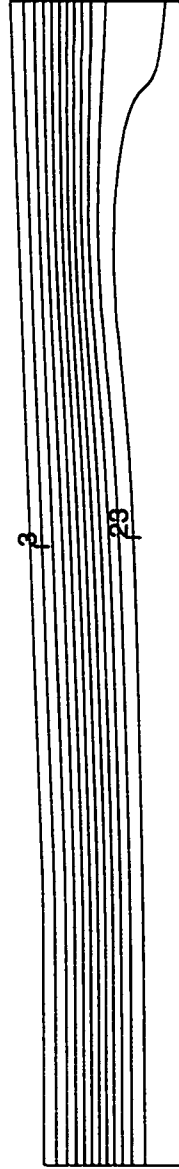


Figure 5.22(d): F Potential After 3200 timesteps (Negative Stratification $r_s = 0.25$ $V_{\theta 1} = 0.60$)

Increment = 0.3
Maximum Value = 25
Minimum Value = 22

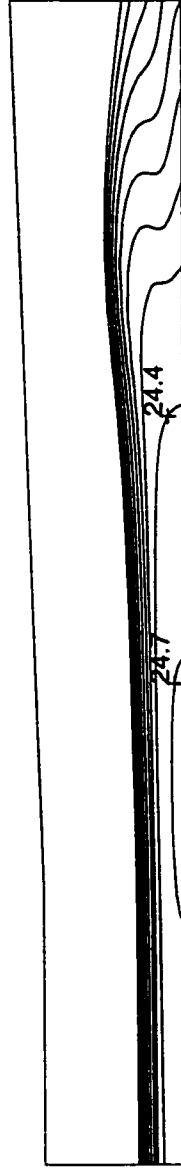


Figure 5.22(e): Detailed F Potential After 3200 timesteps (Negative Stratification $r_s = 0.25$ $V_{\theta 1} = 0.60$)

Increment = 2
Maximum Value = 14
Minimum Value = 0

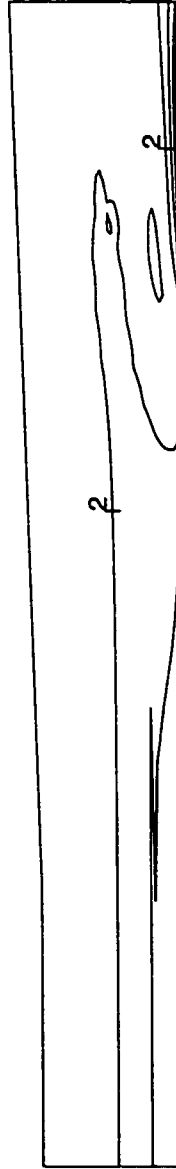


Figure 5.22(f): Axial Vorticity After 3200 timesteps (Negative Stratification $r_s = 0.25$ $V_{\theta 1} = 0.60$)

Increment = 0.4
 Maximum Value = 0.6
 Minimum Value = -3

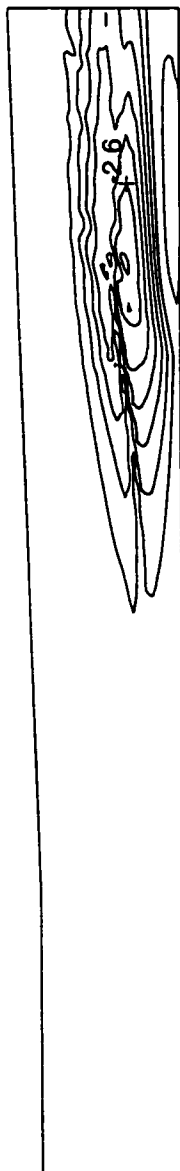


Figure 5.22(g): Azimuthal Vorticity After 3200 timesteps (Negative Stratification $\tau_s = 0.25$ $V_{\theta 1} = 0.60$)

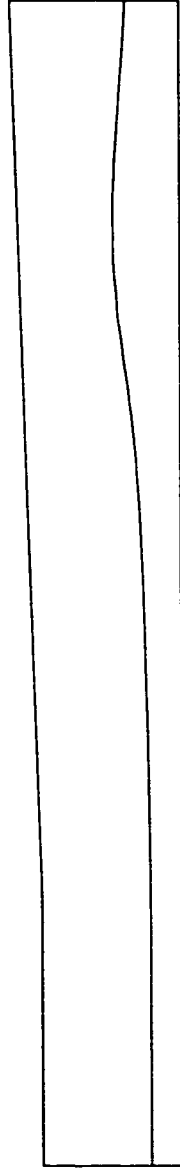


Figure 5.22(h): Density Interface After 3200 timesteps (Negative Stratification $r_s = 0.25$ $V_{\theta 1} = 0.60$)

Negative Density Gradient Outside of Vortex Core

A vortex breakdown solution occurring in a stratified flow with the density interface located at $r_s = 0.77$ with $\rho_1 = 1.0$ and $\rho_2 = 0.9$ is illustrated in Figure 5.23(a). The stagnation zone in this flow is 0.5 units long and the initial stagnation point occurs at approximately $z = 5.1$. Again, the bubble structure can be seen in the Z material lines and B potential, Figures 5.23(b) and 5.23(c). Figures 5.23(d) and 5.23(e) clearly show the F gradients in the bubble region indicating an adverse pressure gradient. Figure 5.23(f) is a single contour of the density interface. The density interface indicates that this flow is starting to develop a Kelvin Helmholtz type instability, due to a pressure wave as shown in Figure 5.23(d). The axial and azimuthal vorticity are shown in Figures 5.23(g) and 5.23(h). There is a region of concentrated azimuthal vorticity generated along the density interface. Due to the oscillations in this flow it is difficult to interpret the vorticity field. The presence of the stratification has, however, reduced the level of concentrated azimuthal vorticity shown in Figure 5.23(h), hindering the occurrence of a breakdown.

Text resumes on page 190

Increment = 0.1
 Maximum Value = 1.1
 Minimum Value = 0



Figure 5.23(a): Axial Velocity Field After 3200 timesteps (Negative Stratification $r_s = 0.77$ $V_{\theta 1} = 0.60$)

Increment = 2
Maximum Value = -15
Minimum Value = -35



Figure 5.23(b): Z Material Field After 3200 timesteps (Negative Stratification $r_s = 0.77$ $V_{\theta 1} = 0.60$)

Increment	= 5
Maximum Value	= -20
Minimum Value	= -70

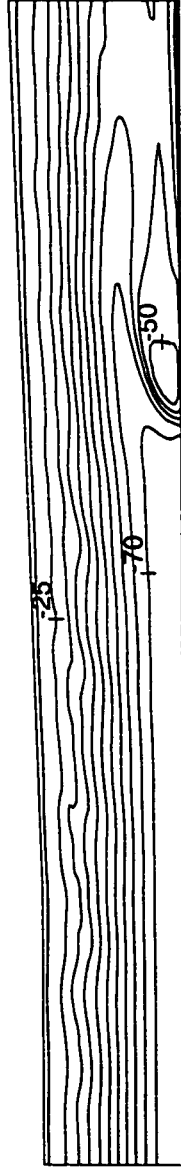


Figure 5.23(c): B Potential After 3200 timesteps (Negative Stratification $r_s = 0.77$ $V_{\theta 1} = 0.60$)

Increment = 2
Maximum Value = 27
Minimum Value = 1

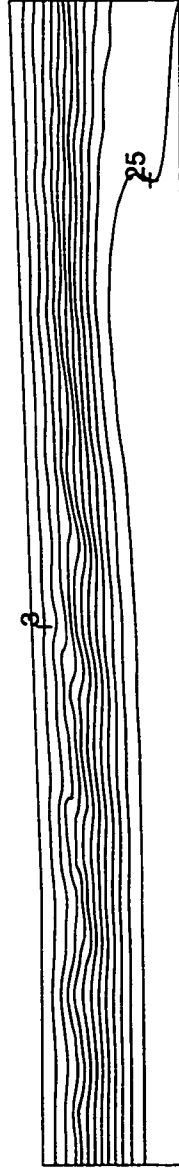


Figure 5.23(d): F Potential After 3200 timesteps (Negative Stratification $r_s = 0.77$ $V_{\theta 1} = 0.60$)

Increment = 0.3
 Maximum Value = 27
 Minimum Value = 24

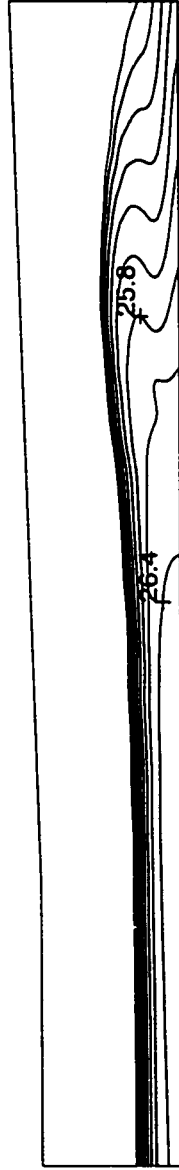


Figure 5.23(e): Detailed F Potential After 3200 timesteps (Negative Stratification $r_s = 0.77$ $V_{\theta 1} = 0.60$)

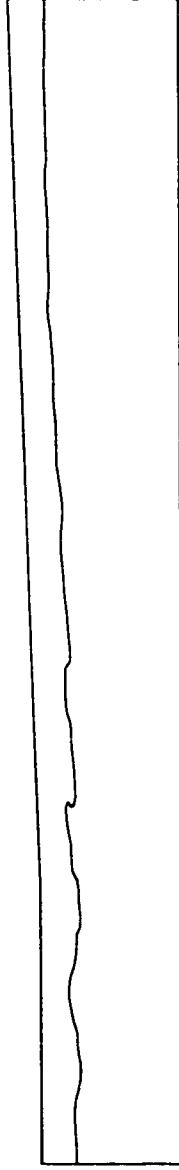


Figure 5.23(f): Density Interface After 3200 timesteps (Negative Stratification $r_s = 0.77$ $V_{\theta 1} = 0.60$)

Increment = 2
Maximum Value = 20
Minimum Value = 0



Figure 5.23(g): Axial Vorticity After 3200 timesteps (Negative Stratification $r_s = 0.77$ $V_{\theta 1} = 0.60$)

Increment = 0.5
 Maximum Value = 2
 Minimum Value = -3



Figure 5.23(h): Azimuthal Vorticity After 3200 timesteps (Negative Stratification $r_s = 0.77$ $V_{\theta 1} = 0.60$)

Positive Density Gradient Inside of Vortex Core

A vortex breakdown solution occurring in a stratified flow with the density interface located at $r_s = 0.25$ with $\rho_1 = 0.9$ and $\rho_2 = 1.0$ is illustrated in Figure 5.24(a). The stagnation zone in this flow is 0.5 units long and the initial stagnation point occurs at $z = 4.5$. The bubble structure can be seen in the Z material lines and B potential, Figures 5.24(b) and 5.24(c). Figures 5.24(d) and 5.24(e) clearly show the F gradients in the bubble region indicating an adverse pressure gradient. The axial and azimuthal vorticity are shown in Figures 5.24(f) and 5.24(g). The density stratification is clearly evident in the density contour of Figure 5.24(h). Negative azimuthal vorticity is being generated in the downstream region of the pipe along this interface, increasing the total negative azimuthal vorticity present. It is this addition of azimuthal vorticity into the flow which is promoting the occurrence of breakdown, as shown in Figure 5.21.

Text resumes on page 199

Increment = 0.1
 Maximum Value = 1.1
 Minimum Value = 0

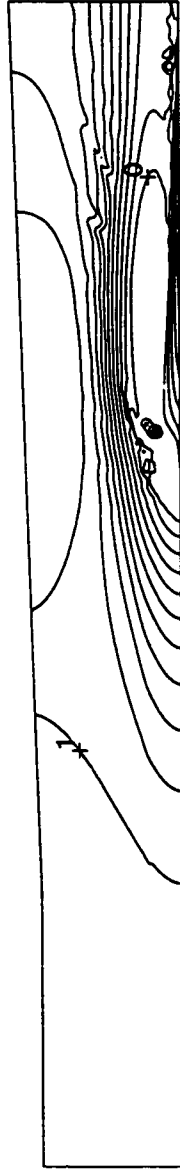


Figure 5.24(a): Axial Velocity Field After 3200 timesteps (Positive Stratification $r_s = 0.25$ $V_{\theta 1} = 0.60$)

Increment = 2
Maximum Value = -13
Minimum Value = -33



Figure 5.24(b): Z Material Field After 3200 timesteps (Positive Stratification $r_s = 0.25$ $V_{01} = 0.60$)

Increment = 8
 Maximum Value = -20
 Minimum Value = -100

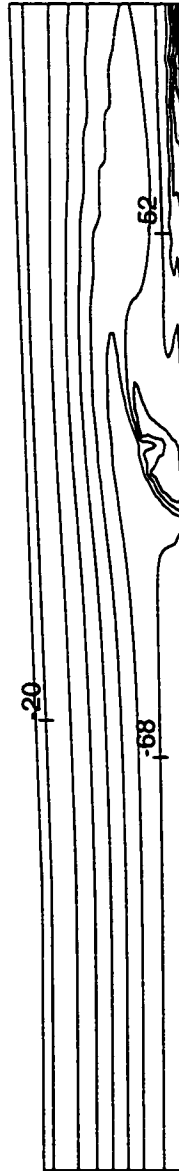


Figure 5.24(c): *B* Potential After 3200 timesteps (Positive Stratification $r_s = 0.25$ $V_{01} = 0.60$)

Increment = 2.5
Maximum Value = 26
Minimum Value = 1

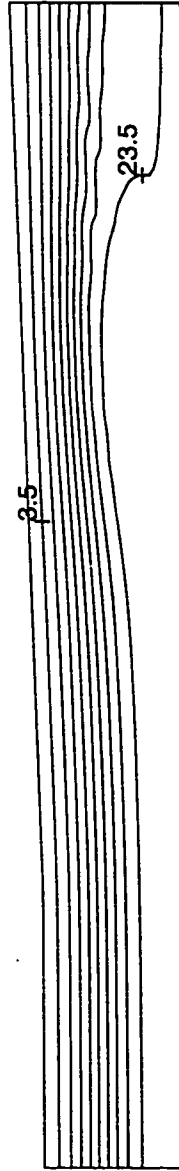


Figure 5.24(d): F Potential After 3200 timesteps (Positive Stratification $r_s = 0.25$ $V_{\theta 1} = 0.60$)

Increment = 0.3
Maximum Value = 26
Minimum Value = 23

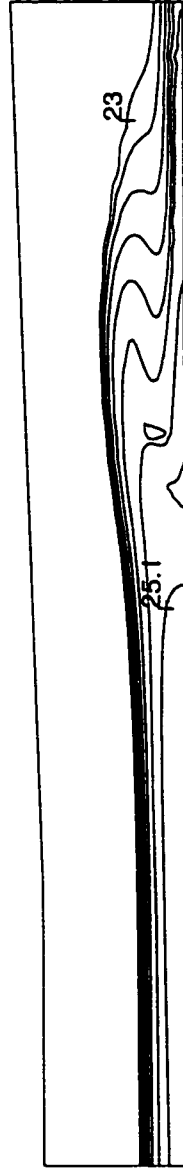


Figure 5.24(e): Detailed F Potential After 3200 timesteps (Positive Stratification $r_s = 0.25$ $V_{\theta 1} = 0.60$)

Increment = 3
Maximum Value = 28
Minimum Value = -2



Figure 5.24(f): Axial Vorticity After 3200 timesteps (Positive Stratification $r_s = 0.25$ $V_{\theta 1} = 0.60$)

Increment = 0.5
 Maximum Value = 1
 Minimum Value = -4

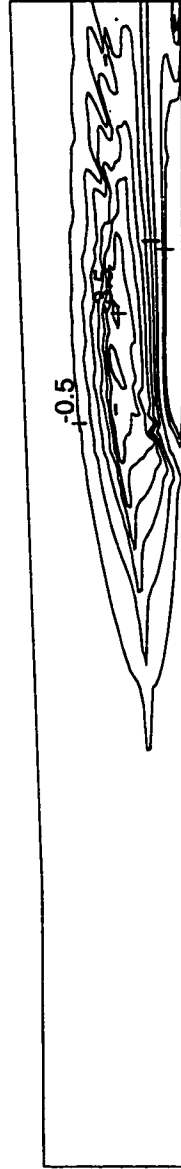


Figure 5.24(g): Azimuthal Vorticity After 3200 timesteps (Positive Stratification $r_s = 0.25$ $V_{\theta 1} = 0.60$)

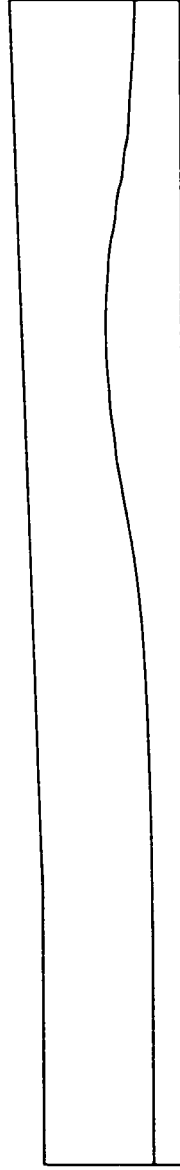


Figure 5.24(h): Density Interface After 3200 timesteps ($r_s = 0.25$ $V_{\theta 1} = 0.60$)

Positive Density Gradient Outside of Vortex Core

A vortex breakdown solution occurring in a stratified flow with the density interface located at $r_s = 0.77$ with $\rho_1 = 0.9$ and $\rho_2 = 1.0$ is illustrated in Figure 5.25(a). The stagnation zone in this flow is 0.5 units long and the initial stagnation point occurs at $z = 4.9$. Again, the bubble structure can be seen in the Z material lines and B potential, Figures 5.25(b) and 5.25(c). Figures 5.25(d) and 5.25(e) clearly show the F gradients in the bubble region indicating an adverse pressure gradient. Figure 5.25(f) is a single contour of the density interface. As opposed to the flow with a negative density gradient located outside of the vortex core, the density interface is not subject to a Kelvin Helmholtz like instability. The axial and azimuthal vorticity are shown in Figures 5.25(g) and 5.25(h). A thin region of azimuthal vorticity is generated along the interface. The presence of the stratification outside of the vortex core has not significantly influenced the concentrated region of negative azimuthal vorticity found in the homogeneous flow case.

Text resumes on page 208

Increment = 0.1
 Maximum Value = 1.1
 Minimum Value = 0

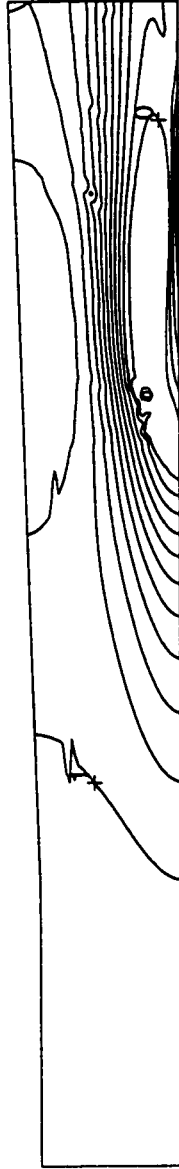


Figure 5.25(a): Axial Velocity Field After 3200 timesteps (Positive Stratification $r_s = 0.77$ $V_{\theta 1} = 0.60$)

Increment = 2
 Maximum Value = -13
 Minimum Value = -33



Figure 5.25(b): Z Material Field After 3200 timesteps (Positive Stratification $\tau_s = 0.77$ $V_{\theta 1} = 0.60$)

Increment = 7
 Maximum Value = -20
 Minimum Value = -90

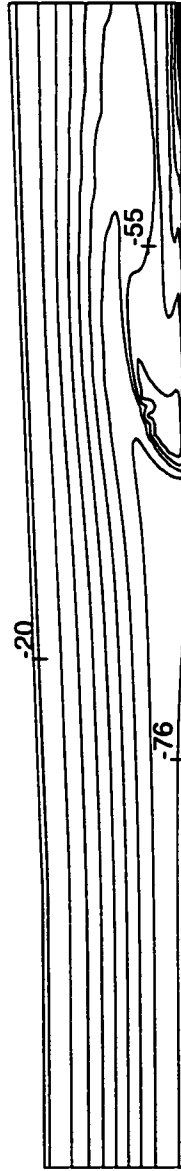


Figure 5.25(c): *B* Potential After 3200 timesteps (Positive Stratification $r_s = 0.77$ $V_{\theta 1} = 0.60$)

Increment = 2
Maximum Value = 25
Minimum Value = 1

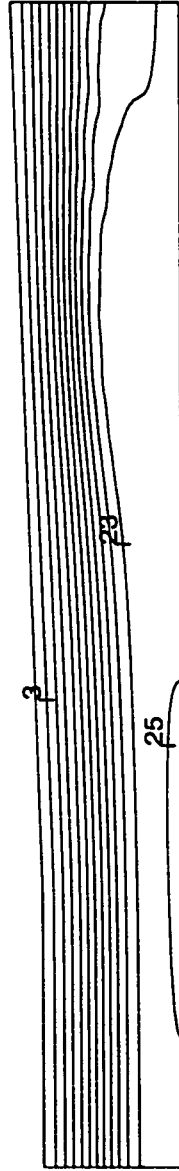


Figure 5.25(d): F Potential After 3200 timesteps (Positive Stratification $r_s = 0.77$ $V_{\theta 1} = 0.60$)

Increment = 0.3
Maximum Value = 25
Minimum Value = 22

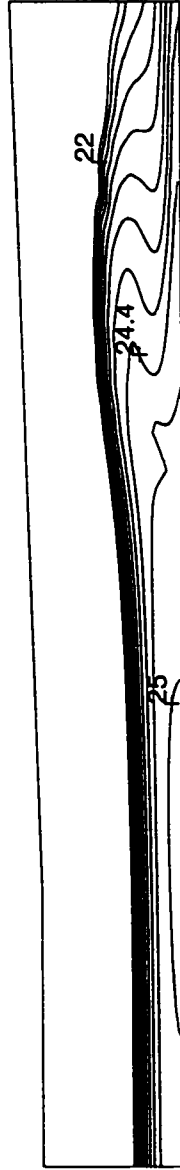


Figure 5.25(e): Detailed F Potential After 3200 timesteps (Positive Stratification $r_s = 0.77$ $V_{\theta 1} = 0.60$)

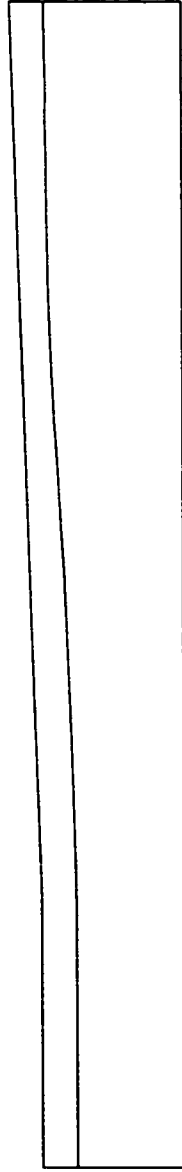


Figure 5.25(f): Density Interface After 3200 timesteps (Positive Stratification $r_s = 0.77$ $V_{\theta 1} = 0.60$)

Increment = 2
 Maximum Value = 24
 Minimum Value = 0



Figure 5.25(g): Axial Vorticity After 3200 timesteps (Positive Stratification $r_s = 0.77$ $V_{\theta 1} = 0.60$)

Increment = 0.6
Maximum Value = 2
Minimum Value = -4

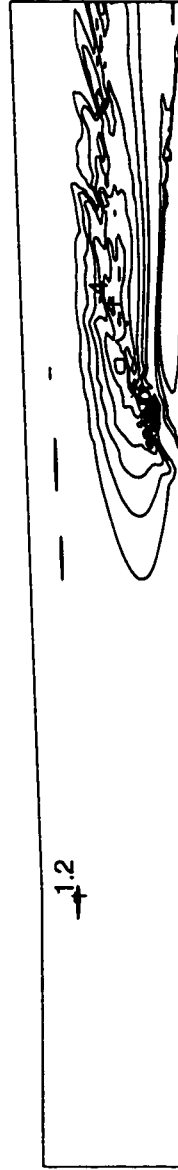


Figure 5.25(h): Azimuthal Vorticity After 3200 timesteps (Positive Stratification $r_s = 0.77$ $V_{\theta 1} = 0.60$)

The preceding set of four stratified flow simulations shows that the influence of vorticity on a breakdown zone depends on local flow conditions. Although the test section is a diverging tube and the global pressure gradient is adverse, the creation of azimuthal vorticity along a density stratification is governed by the local pressure gradients. It was found that the location of vortex breakdown was not influenced significantly by a density stratification located outside of the vortex core. With the stratification located inside the vortex core, a positive stratification moved the location of the initial stagnation point upstream by approximately half a tube radius. A negative stratification located inside of the vortex core moved the breakdown downstream by approximately half a tube radius.

CHAPTER 6

CONCLUSIONS

A modified Clebsch/Weber velocity decomposition was derived for an incompressible, inviscid, stratified, axisymmetric swirling flow. This decomposition separates the flowfield into two components, one rotational and the other irrotational. The rotational component is constructed from a set of hyperbolic complex lamellar potentials while the irrotational component is obtained from a scalar elliptic field. By applying appropriate upwind and central difference techniques to the hyperbolic and elliptic equations, the numerical scheme obeys the information propagation characteristics of the physical problem.

The numerical scheme was used to study vortex breakdown in the stratified flow of immiscible media. Due to the difficulties inherent in calculating a density interface, previous studies of vortex breakdown have been limited to homogeneous flows. The modified Clebsch/Weber decomposition treats density as a material quantity, allowing for the calculation of stratified flows on Eulerian grids.

Experimental vortex breakdown flows are sensitive to flow disturbances

and are not amenable to probe measurements. For this reason, it is impossible to obtain detailed pressure information in breakdown flows. The majority of the computational work on vortex breakdown utilizes the vorticity stream-function equations which do not calculate pressure. The modified Clebsch/Weber decomposition includes pressure information. Since the velocity decomposition is kinematic and the complex lamellar potentials include material quantities, the modified Clebsch/Weber decomposition also includes flow visualization as part of the solution.

The scalar hyperbolic equations were solved by characteristically convecting information to an intermediate time level and updating the solution using a midpoint rule time integration. To ensure a nonoscillatory solution, a uniformly second order accurate (UNO2) interpolation scheme was used. The elliptic equations were solved using an approximately factored LU scheme with multigrid convergence acceleration. Vortex breakdown is a flow instability which is sensitive to small flow disturbances. To avoid reflected pressure waves, the axial velocity is not fixed along the inflow or outflow boundaries.

A non-swirling flow simulation was conducted in a straight pipe. A uniform flow remained uniform after passing four times through the numerical domain. This proved the robustness of the numerical scheme.

Previous investigators have observed vortex breakdown solutions of an inviscid flow in a straight pipe with an applied disturbance. In this study, with no applied disturbance, a Burgers vortex in a uniform axial flow remained unchanged after passing four times through the numerical domain. This proves that any breakdown solutions obtained are due to physical effects and not numerical disturbances.

Vortex breakdown simulations were conducted in a straight/diverging pipe flow domain. The presence of the diffuser promotes the occurrence of a breakdown by creating an adverse pressure gradient. The wave propagation characteristics of a diverging tube prevent the breakdown from moving towards the inlet of the flow domain and influencing the inflow boundary condition.

Simulations were conducted using a Burgers vortex in an initially uniform axial flow. Homogeneous density flows were investigated at different levels of swirl to verify the model's fidelity.

With no swirl velocity, the initial uniform flow was convected through the domain unaltered. With an increase in the magnitude of the swirl, the flow was observed to decelerate along the pipe centerline. At a critical level of swirl, a maximum inflow helix angle of 29° , a stagnation point was formed along the axis of symmetry indicating that a vortex breakdown solution had occurred. Further increases in swirl caused the initial stagnation point to move upstream, and led to the formation of an identifiable breakdown zone characterized by two stagnation points along the flow axis. These results were in qualitative agreement with previous experimental and numerical studies.

The vorticity dynamics approach to vortex breakdown identifies the presence of negative azimuthal vorticity in the flow as a necessary condition for the onset of flow stagnation along the pipe centerline. Swirling flows found in combustion chambers consist of a core of fuel surrounded by an annulus of air. The radial gradients of density present in such flows can lead to the generation of azimuthal vorticity through a Baroclinic torque. To successfully control the onset and structure of vortex breakdown in these flows, it

is necessary to understand the effects of a density stratification on vortex breakdown.

The effect of an immiscible density stratification was first investigated on a critical swirling flow. Simulations were conducted with the density interface located both inside and outside of the vortex core with a density difference of ten percent.

It was observed that a positive density gradient in the radial direction promoted the onset of vortex breakdown while a negative density gradient hindered breakdown solutions. The effect of the density stratification was more pronounced when the density interface was located inside the vortex core. A breakdown zone is characterized by a region of negative azimuthal vorticity. In the presence of a local adverse pressure gradient, a positive density gradient creates negative azimuthal vorticity through a Baroclinic torque, thus promoting breakdown. A negative density gradient in a local adverse pressure gradient creates positive azimuthal vorticity which delays the onset of breakdown. When the stratification is located outside of the vortex core, away from the location of concentrated azimuthal vorticity, its influence on the breakdown zone is less significant.

The effects of a density stratification on a flow with a swirl level above the critical level were also investigated ($\beta = 34^\circ$). The same trends as occurred with the critical swirling flow were evident at this swirl level. In addition, it was observed that the positive density gradient caused the breakdown to occur upstream of its homogeneous breakdown location. A negative density gradient moved the breakdown downstream of its homogeneous location.

This work could be extended in several ways. At the inviscid level, it

would be interesting to conduct simulations using an inflow shear instead of a uniform axial flow. It would also be interesting to use a straight pipe flow domain and to investigate various inflow disturbances to see if they trigger a breakdown.

The influence of three dimensional effects on vortex breakdown could be studied by incorporating the correlation terms resulting from the axisymmetric averaging process. Viscous effects could also be incorporated by adding another term to the potential/complex lamellar decomposition.

Bibliography

1. Batchelor, G.K. 1967 "An Introduction to Fluid Dynamics." pp. 543-555. Cambridge University Press
2. Benjamin, T.B. 1962 "Theory of the Vortex Breakdown Phenomenon" J. Fluid Mech. **14**: 593
3. Benjamin, T.B. 1967 "Some Developments in the Theory of Vortex Breakdown Phenomenon" J. Fluid Mech. **28**: 65
4. Beran, P.S. 1994 "The Time Asymptotic Behavior of Vortex Breakdown in Tubes." Computers Fluids **23**: 913-937
5. Beran, P.S., Culick, F.E. 1992 "The Role of Non-Uniqueness in the Development of Vortex Breakdown in Tubes" J. Fluid Mech. **242**: 491
6. Buntine, J.D. & Saffman, P.G. 1995 "Inviscid Swirling Flows and Vortex Breakdown." Proc. R. Soc. Lond. A **449**: 139-153
7. Brown G.L., Lopez J.M. 1990 "Axisymmetric Vortex Breakdown Part 2: Physical Mechanisms" J. Fluid Mech. **221**: 553
8. Bruecker, Ch., Althaus, W. 1995 "Study of Vortex Breakdown by Particle Tracking Velocimetry (PTV), Part 3: Time Dependent Structure and Development of Breakdown Modes" Exps. Fluids **18**: 174
9. Darmofal, D.L. 1993 "The Role of Vorticity Dynamics in Vortex Breakdown" A.I.A.A. Paper 93-3036

10. Darmofal, D.L. 1996 "Comparisons of Experimental and Numerical Results for Axisymmetric Breakdown in Pipes" *Computers Fluids* **25**: 353
11. Grabowski W.J., Berger S.A. 1976 "Solutions of the Navier Stokes Equations for Vortex Breakdown" *J. Fluid Mech.* **75**: 525
12. Faler, J.H., Leibovich, S. 1977a "Disrupted States of Vortex Flow and Vortex Breakdown" *Phys. Fluids* **20**: 1385
13. Faler, J.H., Leibovich, S. 1977b "An Experimental Map of the Vortex Breakdown." *J. Fluid Mech.* **86**: 313-335
14. Hall, M.G. 1972 "Vortex Breakdown." *Ann. Rev. Fluid Mech.* **4**: 195-217
15. Harvey, J.K., "Some Observations of the Vortex Breakdown Phenomenon." *J. Fluid Mech.* **14**: 589-592
16. Jameson, A., Schmidt, W., Turkel, E. 1981 "Numerical Solution of the Euler Equations by Finite Volume Methods Using Runge Kutta Time Stepping Schemes" *A.I.A.A. Paper* 81-1259
17. Kopecky, R.M., Torrance, K.E. 1973 "Initiation and Structure of Axisymmetric Eddies in a Rotating Stream" *Comput. Fluids* **1**: 289
18. Leibovich, S. 1978 "The Structure of Vortex Breakdown." *Ann. Rev. Fluid Mech.* **10**: 221-246
19. Leibovich, S. 1984 "Vortex Stability and Breakdown: Survey and Extension" *A.I.A.A.J.* **22**: 1192-1206

20. Leibovich, S., Kribus, A. 1990 "Large Amplitude Wavetrains and Solitary Waves in Vortices" *J. Fluid Mech.* **216**: 459
21. Lessen, H., Singh, P.J., Paillet, F. 1974 "The Stability of a Trailing Line Vortex. Part 1. Inviscid Theory" *J. Fluid Mech.* **63**: 753
22. Ludweig, H. 1962 "Vortex Breakdown" *Z. Flugwiss* **10**: 242
23. Ludweig, H. 1965 "Vortex Breakdown Part 2" *Z. Flugweiss* **13**: 437
24. Panton, R. [1996] "Incompressible Flow." pp. 113-115, pp. 530-536. Wiley Interscience
25. Peckham, D.H., Atkinson, S.A. 1957 "Preliminary Results of Low Speed Wind Tunnel Tests on a Gothic Wing of Aspect Ratio 1.0" Aeronautical Research Council, CP508
26. Popper, K.R. 1969 "Conjectures and Refutations" London: Routledge and Kegan Paul
27. Randall, J.D., Leibovich, S. 1973 "The Critical State: A Trapped Wave Model of Vortex Breakdown" *J. Fluid Mech.* **53**: 481
28. Rusak, Z., Whiting, C.H., Wang, S. 1998 "Axisymmetric Breakdown of a Q Vortex in a Pipe" *A.I.A.A.J.* **36**: 1848
29. Rusak, Z., Judd, K.P., Wang, S. 1997 "The Effect of Small Pipe Divergence on Near Critical Swirling Flows." *Phys. Fluids* **9**: 2273

30. Salas, M. D. & Kuruvila, G. 1989 "Vortex Breakdown Simulation: A Circumspect Study of the Steady Laminar, Axisymmetric Model." *Computers and Fluids*. **17**: 247-262
31. Sarpkaya, T. 1971a "Vortex Breakdown in Swirling Conical Flows" *A.I.A.A.J* **9**: 1792
32. Sarpkaya, T. 1971b "On Stationary and Travelling Vortex Breakdowns" *J. Fluid Mech.* **45**: 545
33. Sarpkaya, T. 1974 "Effect of the Adverse Pressure Gradient on Vortex Breakdown" *A.I.A.A.J* **12**: 602
34. Spall, R.E, Gatski, T.B., Grosch, C.E. 1987 "A Criterion for Vortex Breakdown" *Phys. Fluids* **30**: 3434
35. Spall, R.E., Gatski, T.B., Ash, R.L. 1990 "The Structures and Dynamics of Bubble Type Vortex Breakdown" *Proc. R. Soc. Lond.* **429**: 613
36. Squire, H.B. 1960 "Analysis of the Vortex Breakdown Phenomenon." *Miszallaneen der Angewandton Mechanik*, pg 306-312. Berlin: Akademie
37. Trigub, V.N. 1985 "The Problem of Breakdown of a Line Vortex." *Prikl. Math Mech.* **49**: 166
38. Wang, S., Rusak, Z. 1996 "On the Stability of An Axisymmetric Rotating Flow" *Phys. Fluids* **8**: 1007

39. Wang, S., Rusak, Z. 1997 "The Dynamics of Swirling Flow in a Pipe and Transition to Axisymmetric Vortex Breakdown." J. Fluid Mech. **340**: 177-223
40. Yokota, J. 1987 "An LU Implicit Multigrid Algorithm to Solve the Euler Equations for Transonic Flow in Rotating Turbomachinery Passages." PhD. Thesis Cornell University
41. Yokota, J. 1993 "Vorticity Dynamics of Inviscid Shear Layers." AIAA **31**: 1430
42. Yokota, J. 1997 "Potential/Complex Lamellar Descriptions of Incompressible Viscous Flow." Phys. Fluids **9**: 2264
43. Yokota, J. 1998 "A Kinematic Velocity Decomposition of Stratified Flow." IJCFD **9**: 121